Superresolution fluorescence microscopy studies of the F-actin cytoskeleton in PC12 cells and DNA loci in *E. coli*

By

Renée M. Dalrymple

A dissertation submitted in partial fulfillment of

the requirements for the degree of

Doctor of Philosophy

(Chemistry)

at the

UNIVERSITY OF WISCONSIN-MADISON

2013

Date of final oral examination: 08/28/13

The dissertation is approved by the following members of the Final Oral Committee:

James C. Weisshaar, Professor, Chemistry

John C. Wright, Professor, Chemistry

Tomas F. J. Martin, Professor, Biochemistry

Richard L. Gourse, Professor, Bacteriology

Randall H. Goldsmith, Assistant Professor, Chemistry

Table of Contents

Acknowledgements

I would like to thank a number of people, without whom this work would not have been possible.

Thank you to my advisor Jim Weisshaar, who taught me to think critically and quantitatively about my results. Those are skills that I will carry with me long after leaving his lab. I'd like to thank him for the opportunity to be involved with the construction of our superresolution microscope. It was an amazing learning experience, and I am grateful to have been there from the beginning of such an exciting endeavor.

I would also like to thank the Weisshaar group members, past and present, for their mentorship and friendship. I would especially like to thank Colin Ingram, Izzy Smith, Kem Sochacki, and Ben Bratton for taking the time to teach a young graduate student the skills I needed to succeed in the Weisshaar Group. I would also like to thank Somenath Bakshi for his comradery. In was a pleasure to sit next to you for five years! Ken Barns, thanks for always being there and for offering a cookie when things weren't going well. Ranga, thank you for your friendship, and for your careful editing of this manuscript. Wenting Li, thank you for always smiling and for making sure I never went hungry. When I see a Ferrero Rocher, I will think of you. Trilly Gregg, thank you for your support and encouragement. To all the residents of 4225, whether about science, philosophy, or nothing at all, our conversations were always a welcome addition to a day in the lab.

I have had the pleasure of working on numerous projects across many departments on campus. Thank you to all of my collaborators over the years, both faculty and students for the opportunity to expand my knowledge base and become a more well-rounded scientist. Tom Martin and Elle Kielar-Grevstad, thank you for your insights about all things PC12 and for giving me the opportunity to work with you on F-actin imaging. Rick Gourse and Tamas Gaal, thank you for the use of your constructs. Tamas, thank you for your patient explanations and cloning help. Kevin Eliceiri, thank you for providing advice as I navigated my transition from graduate school.

Thank you to my committee members for your time, guidance, and review of my work. John Wright, your courses pushed me, but ultimately provided a sense of accomplishment and cohesion among our class. Your complementary comments at my RP gave me confidence moving forward.

To my friends in Madison, thank you for making my time here so fun and special. Thank you to my ballet buddies for encouraging me to get to the studio. That time was such a wonderful outlet for me and let me recharge. Thank you to Madison Ballet for allowing me to continue to pursue my passions outside of science, and for the opportunity to perform with you. There are not many companies that would allow a busy graduate student a place on their cast list. Being on stage at the Overture Center is something I will not forget.

Thank you to my Wisconsin family for looking out for me when I moved here, and for making sure I always had somewhere to go for the holidays. It has been wonderful spending time with you all and being able to be here for family events.

Finally, I need to thank my family for their endless love and support. Thank you to my brother Evan, for always reminding me to have fun. Thank you to my parents, Bob Dalrymple and Lonie Shortreed, for always encouraging me to pursue my education, from elementary school to my Ph. D.. Thank you for providing me with the tools and opportunities to get this far. Mom, I feel blessed that I was able to spend six years here where you grew up. Dad, I am proud to join you as a UW Madison Ph. D.!

To my boyfriend Jeff, words cannot express the amount of support you have given me over the years. Thank you for being with me through the ups and downs that only someone who has lived with a grad student can understand. Thank you for sharing this enormous adventure with me. Here's to the next!

Abstract

With the development of superresolution fluorescence microscopy techniques, it is now possible to study the precise structural organization and movement of biological systems to ~20 nm resolution. This thesis describes the construction of a superresolution microscope capable of epifluorescence, total internal reflection fluorescence (TIRF), photoactivated localization microscopy (PALM), direct stochastic optical reconstruction microscopy (dSTORM), and single particle tracking (SPT). These techniques were applied to the actin cytoskeleton and vesicles in PC12 cells, and DNA loci in *Escherichia coli* (*E. coli*).

The cytoskeletal component, filamentous actin (F-actin), has been implicated in the regulation of vesicle exocytosis in neuroendocrine cells. Superresolution images of F-actin before, 20 s after, and 120 s after stimulation of exocytosis were obtained in PC12 cells. F-actin bundles, which are present before stimulation, are absent from the structure 20 s after stimulation. They re-form less than 120 s post-stimulation. Vesicles were positioned in regions of lower F-actin density. Superresolution was used to determine that vesicles have an average diameter of 134 ± 40 nm.

We studied the movement and spatial organization of DNA loci labeled with a GFP-ParB/*parS* system in *E. coli*. SPT of various DNA loci was performed at 33 Hz. Mean squared displacement analysis was used to show that loci move similarly to each other at this time-scale. Long trajectories exhibited slower motion likely due to the physical bulk of multiple GFP-ParB copies. DNA loci tracking was used as a benchmark to determine the partitioning of RNA polymerase molecules into different biologically relevant states.

Individual loci were found to have specific spatial organization along the short cellular dimension. The majority of studied loci were located preferentially away from the center in cells grown in moderate growth conditions. The distributions were less peripherally located in cells grown in less rich conditions. These results suggest that on average the *E coli.* nucleoid exhibits some degree of hollowness. It is possible that loci are excluded from the bulk of the nucleoid due to the GFP-ParB/*parS* labeling system. The DNA loci work shown here should be verified using a different labeling scheme such as a fluorescent repressor operator system (FROS).

Chapter 1

Introduction

Methods of superresolution fluorescence microscopy

Overview

This thesis describes the use of superresolution fluorescence microscopy to study a variety of biological systems. Chapter 1 provides an introduction to fluorescence microscopy methods including Total Internal Reflection Fluorescence (TIRF), Photoactivated Localization Microscopy (PALM), direct Stochastic Optical Reconstruction Microscopy (dSTORM), and single particle tracking (SPT). It also describes the construction of our superresolution microscope setup. Chapter 2 discusses the application of dSTORM to the study of the cytoskeleton in neuroendocrine cells, as well as the spatial relationship of the cytoskeleton to secretory vesicles. Chapter 3 discusses the use of SPT to study the movement of DNA loci inside of *E. coli* cells. Chapter 4 explores the spatial arrangement of these DNA loci in the radial dimension of the cell and its implications for overall nucleoid structure and organization.

Fluorescence microscopy

The understanding of biological systems requires knowledge of the distribution and dynamics of cellular components. Fluorescence microscopy provides scientists with the tools to

image these cellular components inside of chemically fixed or living cells. Methods for fluorescent labeling such as immunocytochemistry and tagging with fluorescent proteins allow the observation of specific components of interest. Spectral separation of a diverse and expanding library of labels allows multiple structures to be imaged in the same cell.

Historically, the primary disadvantage of fluorescence microscopy was that the resolution was limited to approximately half the wavelength of light in x and y (~200-250 nm), and ~500 nm in z. This is due to the diffraction limit of light defined by Ernst Abbe and Lord Rayleigh.[1,2] Many biological structures of interest are smaller than this limit and were out of reach. Recently, there have been a number of landmark advances in the field which have allowed scientists to improve the possible resolution and even "break" the diffraction limit.

One method of improving resolution is to limit the contribution to blurring from out of focus light. This can be accomplished by using total internal reflection (TIRF) microscopy. In TIRF, the incoming excitation beam is shifted off of the central axis of the objective causing it to refract at an angle at the glass-medium interface (Figure 1.1). This angle increases as the beam is shifted until the critical angle, θ_c, is surpassed and the beam is total internally reflected. This critical angle is given by

$$\theta_c = \sin^{-1}(n_1/n_2) \qquad \textbf{(1.1)}$$

where n_1 is the index of refraction of the sample and n_2 is the index of refraction of the glass coverslip, with $(n_1/n_2) < 1$. This results in an evanescent wave of light that decays exponentially from the surface. This wave illuminates only the bottom ~200 nm of the sample and thus eliminates background fluorescence from deeper in the sample. This effectively improves the resolution in the z dimension by about a factor of two; however, it remains the

same in x and y. TIRF is extremely useful for studying structures at the cell surface, such as the cytoskeleton, but is limited to these structures.

Confocal laser scanning microscopy (CLSM) in contrast, has become a technique of choice for imaging beyond the surface and performing optical sectioning at improved resolution. In CLSM, a tightly focused laser beam is scanned across the sample and a pin hole, or small aperture, is used to allow only light from the focal plane to pass through, thus eliminating out of focus light.[3,4] This improves the resolution, but the increase is limited by the need to decrease the size of the pin hole, which discards the majority of the light.

Superresolution fluorescence microscopy

Structured illumination

The truly groundbreaking developments in resolution improvement came with the invention of superresolution microscopy techniques, which effectively "break" the diffraction limit. These methods rely on either patterned illumination or the localization of single molecules. In structured illumination microscopy (SIM) the sample is illuminated with a pattern of sinusoidal stripes. The fine details of the structure, which were previously unresolvable, interact with the patterned light and form moiré fringes (Figure 1.2). The orientation of the pattern is varied and the information from the moiré fringes is used to extract the higher spatial frequency information of the finer details of the structure.[5,6] It can also be extended into three dimensions.[7] SIM improves the image resolution by approximately a factor of two in all three dimensions. One particular advantage of this technique is that virtually any fluorescent label can be used and there are no specific sample preparation requirements. In addition, it is

commercially available, making it easy for users to obtain superresolution images in a minimal amount of time (Carl Zeiss Microscopy, Applied Precision, Nikon Instruments).

Single molecule methods

The largest improvements in resolution have come from the single molecule based techniques. Three of these techniques were developed almost simultaneously and share the same basic theory: photoactivated localization microscopy (PALM), stochastic optical reconstruction microscopy (STORM), and fluorescence photoactivation localization microscopy (FPALM).[8-10] These techniques use a pointillism approach in which the locations of individual molecules are combined to reconstruct a high resolution image.

The emission point-spread function (PSF) from one molecule can be well fit to a Gaussian function in order to precisely determine its location to ~5 nm in theory, ~20 nm in practice (Figure 1.3). The precision depends on the number of photons collected. When the PSFs from two neighboring molecules get so close that their PSFs overlap, their distinct locations can no longer be resolved (Figure 1.4). Superresolution techniques break this resolution limit by separating the emission of the molecules in time and then finding their precise individual locations. This has been made possible by the discovery of photoactivatable and photoswitchable fluorophores.

Fluorophores for superresolution imaging

There are a number of different fluorophore options for this type of imaging. PALM is generally performed with fluorescent proteins which are endogenously expressed. There are photoswitchable fluorescent proteins such as mEos2, which change their emission color upon

activation with UV light (usually 405 nm), and photoactivatable fluorescent proteins such as PATagRFP, which change from a dark to fluorescent state upon activation.[11,12] These probes have the advantage of being applicable to living cells, since they are endogenously expressed, and provide specific labeling.

STORM typically uses photoswitchable dye pairs such as Cy3-Cy5. Direct STORM (dSTORM) refers to the use of reversibly photoswitching organic dyes such as Alexa Fluor 647 or Atto 488, which were used in this work.[13] dSTORM dyes can be driven to a long-lived dark state from which they stochastically return to a fluorescent state under specific conditions (discussed below). These dyes are conjugated to the structure of interest using immunocytochemistry, which is both an advantage and disadvantage. Existing protocols which utilize these dyes for widefield imaging can be used, but the antibodies add ~20 nm of distance between the molecule of interest and the label, thus limiting the obtainable resolution. They also require the use of special imaging buffers and an oxygen free environment in order to undergo photoswitching.[14] These buffers generally include a reducing agent and an oxygen scavenging system to minimize photobleaching. This limits dSTORM experiments to fixed specimens.

Experimental procedure

In order to collect the data for PALM imaging, a sparse subset of labels is activated, or made fluorescent, using a small dose of the activation laser. The number of molecules which activate is dependent on the dose of the activation laser. This is controlled so that there is a very low probability that the point spread functions of activated molecules overlap. These molecules are then excited by the excitation laser and imaged until they bleach. A new subset of molecules is then activated and excited until they bleach. This cycle is repeated until either all of the

molecules have been bleached or sufficient data is collected to construct an image (Figure 1.5). For dSTORM, the molecules are driven to a long-lived dark state with the excitation laser and stochastically return to a fluorescent state. No activation laser is generally needed, although it can be used to increase the rate of return to the fluorescent state if needed.[14] After the data is collected, the point spread functions of each individual molecule is fit to a Gaussian function in order to find its location to sub-diffraction limit precision.

Resolution

In theory, the resolution of PALM/STORM type experiments is related to the number of photons collected for each single molecule. The precision with which each molecule is localized is given by

$$\sigma_{x,y}^{\ 2} \approx \frac{s^2 + a^2/12}{N} + \frac{4\sqrt{\pi} s^3 b^2}{a N^2} \qquad \textbf{(1.2)}$$

where s is the standard deviation of the Gaussian which approximates the PSF, N is the number of detected photons, b is the number of background photons collected and a is the pixel size.[15] Simplifying, $\sigma_{x,y}$ is proportional to $1/\sqrt{N}$. For this reason high laser power densities are used in order to have as many photons collected per camera frame as possible, rather than spreading them out over several frames.

In practice, the resolution of the image is often limited by the labeling density of the sample. To accurately depict a feature, a large enough number of molecules must be detected to fulfill the Nyquist-Shannon sampling criterion.[16] Other factors which play into this include not just the physical labeling density, but also the percentage of fluorophores which actually undergo

the photoactivation or photoswitching process. In the case of fluorescent proteins, this percentage can be quite low. Attempts have been made to characterize this for various fluorophores, but it is dependent on the fluorophore and the experimental conditions.[17] For organic dSTORM dyes the buffer conditions must be correct to allow proper photoswitching or the fluorophores will be permanently bleached and undergo fewer switching cycles.[14] In order to obtain high resolution images, samples for PALM experiments must express a sufficient number of labels which successfully photoactivate. dSTORM samples must have enough binding sites for the labels to achieve an appropriate density and the imaging buffer conditions must be optimized.

Single particle tracking

Aside from obtaining static high resolution images, photoactivatable proteins can also be used to perform single particle tracking (SPT) experiments, or sptPALM.[18] A sparse number of molecules can be activated and their motion can be tracked over time with ~20 nm precision. These types of experiments can also be performed in the absence of photoactivatable fluorophores if there is a sparse number of diffraction limited spots visible in the sample. For example, dilution experiments can be performed where the concentration of labeled molecules is reduced. Or, if there are only a few of the objects of interest present in the cell to begin with, they can be tracked as is described for DNA loci in Chapter 3.

Advances in camera technology now allow scientists to watch the movement of molecules in real time. Electron multiplying CCDs (EMCCDs) provide excellent light detection for single molecule imaging and can even image up to 500 Hz. Motion can now be studied on a wide variety of time-scales.

Information about the properties of the motion under study can be obtained from the particles' trajectories. Mean squared displacement analysis can be performed to assess if the motion is diffusive, directed, or subdiffusive. Heterogeneity in molecular motion can be discovered since SPT allows the observation of single molecules as opposed to bulk measurements, which effectively average over the population. Molecules can also be seen to undergo transitions between different types of motion.

Construction of a superresolution microscope

In order to perform superresolution and SPT experiments, the proper microscope system must be assembled or purchased. At the time of this thesis work, commercial versions of superresolution microscopes were not available. In order to construct a microscope capable of these techniques, time was devoted to the selection, purchase, and setup of the proper components. The original design was based on that of Betzig *et al*..[8] A vibration isolating table equipped with Gimbal piston isolators was installed in order to minimize ground vibrations (TMC). A Nikon Ti-E microscope equipped with a perfect focus system, a TIRF 1.49 NA objective, and a CFI Plan Apo Lambda DM 100X Oil phase contrast objective 1.45 NA was coupled to an Andor iXonEM+ 897 EMCCD camera for detecting single molecules. A tunable Ar^+ laser (Melles Griot), a 405 nm diode laser (CrystaLaser), and a 561 nm Sapphire CW laser (Coherent) were combined and directed into the rear microscope port. Fast shutters (Uniblitz LS2, Vincent Associates) were used to synchronize illumination and image acquisition; and switch between excitation and activation pulses for PALM imaging. An enclosed chamber was built around the microscope stage and was equipped with a temperature control system (Air-

Therm-ATX, World Precision Instruments) in order to keep the sample at a constant temperature and minimize thermal drift (Figure 1.6, 1.7).

Additional post-microscope devices were constructed for simultaneous dual-color imaging and biplane PALM imaging. The biplane PALM device was modeled after the design of Juette *et al*.[19] These devices were designed in collaboration with Benjamin Bratton and constructed in the UW Madison Chemistry Machine Shop. Briefly, the emission from the sample is passed through an aperture to reject any scattered light, then through a collimating lens and either a dichroic mirror or 50/50 beam splitter. The two paths are directed to a focusing lens and then onto the camera chip. In the case of the two-color apparatus the two light paths pass through the appropriate emission filters. For biplane imaging one path passes through an additional lens which acts as the biplane lens (Figure 1.8, 1.9). This defocuses the light so that it focuses on a slightly different plane than the light from the other path. For a detailed description of the design of these devices see Benjamin Bratton's thesis.[20]

Data analysis and image construction

A very important aspect of these superresolution methods is the data analysis. The final product is not a traditional image, but a rendered or reconstructed image. This makes the quality of the image highly dependent on the software used to construct it. Our lab has developed a MATLAB based software suite. It first smooths the images using a bandpass filter to remove high and low frequency noise. This provides a zero based image. A single pixel based threshold is then used to determine which particles are detected. The PSFs of these particles are then fit to a two-dimensional Gaussian function or their centroids are found. For linking molecules in successive frames, tracking is done based on the program written by Crocker and Grier.[21]

Images acquired over long periods of time are drift corrected by tracking fiducial markers added to the sample. Their average movement in x and y is subtracted from the detected molecules' positions for each frame.

Superresolution images are constructed by building a frequency histogram in 2D space. Molecule positions are binned into pixels, the size of which is determined by the resolution of the image (usually 20 x 20 nm). The number of counts, and thus intensity, in each pixel is representative of how many localizations landed in that pixel. This type of rendering provides information about the location of every molecule and how many molecules were detected at a certain position. Alternatively, molecule positions are often displayed as Gaussians with σ equal to the precision with which that molecule was located (dependent on number of photons collected). This provides a slightly more conventional looking image.

Applications of superresolution microscopy

dSTORM of the cytoskeleton in PC12 cells

The cytoskeleton of PC12 cells contains filamentous actin (F-actin) fibers, which are ~7 nm in diameter and are often found in bundles. It has been shown that these fibers play a role in regulating the process of vesicle exocytosis. While electron microscopy can provide high resolution images of the cytoskeleton, the specificity of fluorescent labeling provides a method to image both the F-actin fibers and secretory vesicle content in the same cell. The spatial relationship between these two structures has been studied using TIRF microscopy, but this does not provide the resolution required to see where the vesicles are specifically located in relation to individual F-actin bundles.[22] Chapter 2 describes the first dSTORM images of F-actin in PC12

cells before, and at various time points after, cell stimulation. Two-color images of F-actin and vesicles are also shown. The F-actin structure reorganizes upon stimulation. F-actin bundles, which are present before stimulation, depolymerize and are absent from the structure 20 s after stimulation. They reform less than 120 s post-stimulation. Vesicles were positioned in regions of lower F-actin density. In addition, dSTORM images of vesicles were obtained and analyzed. Vesicles were determined to have an average diameter of 134 ± 40 nm.

SPT of DNA loci in E. coli

Individual DNA loci in *E. coli* can be fluorescently labeled using a GFP-ParB/*parS* system. Fluorescence from this system appears as a diffraction limited spot. Since there are only ~1-8 copies of each locus per cell in our growth conditions, these individual foci are well separated and can be tracked in time using SPT. In Chapter 3, we describe the tracking of DNA loci at time-scales which are 30x faster than those reported at the time of this work. This provides information about the inherent motion of the DNA polymer in the cell environment. These studies of DNA motion have also been used as a benchmark to determine the partitioning of RNA polymerase molecules into different biologically relevant states.[23] Possible drawbacks of the GFP-ParB/*parS* labeling scheme are also discussed.

Spatial distribution of DNA loci in the short dimension of E. coli

DNA loci in *E. coli* have been shown to be highly organized along the axial (long) dimension of the cell.[24-31] Little work has been done to determine if there is also organization along the radial (short) dimension of the cell. Chapter 4 discusses the organization of DNA loci along this short dimension. Individual loci were found to have specific organization. The

majority of studied loci were located preferentially away from the center of the short axis. The spatial distributions of the loci varied with cellular growth conditions and in general were less peripherally located in cells grown in less rich medium. These results suggest that on average the *E coli.* nucleoid exhibits some degree of hollowness.

Summary

With the development of superresolution microscopy techniques, it is now possible to study the precise structural organization of biological systems to ~20 nm resolution. It is also possible to track the motion of individual molecules in real time, thus obtaining information about biological processes which was previously out of reach. Heterogeneous motion can now be discerned, whereas it was previously averaged together by bulk measurements.

The construction of our superresolution microscope has added enormous capabilities to the laboratory. It has been used previously to track fast diffusing cytoplasmic proteins in *E. coli*, and obtain superresolution images of ribosomes and RNA polymerase.[23,32,33] This thesis describes the use of the techniques described here as well as this microscope to obtain superresolution images of the cytoskeleton and secretory vesicles in PC12 cells (Chapter 2), study the motion of DNA loci and compare it to that of RNAP molecules to determine the fraction of transcribing RNAP molecules in *E. coli* (Chapter 3), and study the spatial distribution of DNA loci within the cell (Chapter 4). It will continue to be essential for numerous other ongoing and future projects.

Figures

Figure 1.1. TIRF microscopy. **(Top)** Schematic of switching from epifluorescence to TIRF. In epifluorescence the beam travels straight through the objective (left). As the beam is moved off of the central axis of the objective it is refracted at an angle (middle). When this angle surpasses the critical angle, the beam is totally internally reflected (right). **(Bottom)** The entire cell is illuminated using epifluorescence (left). In TIRF only the bottom ~200 nm of the cell is illuminated (right). Top figure reproduced with modifications from the web.[34] Bottom figure reproduced with modifications from Balagopalan *et al*..[35]

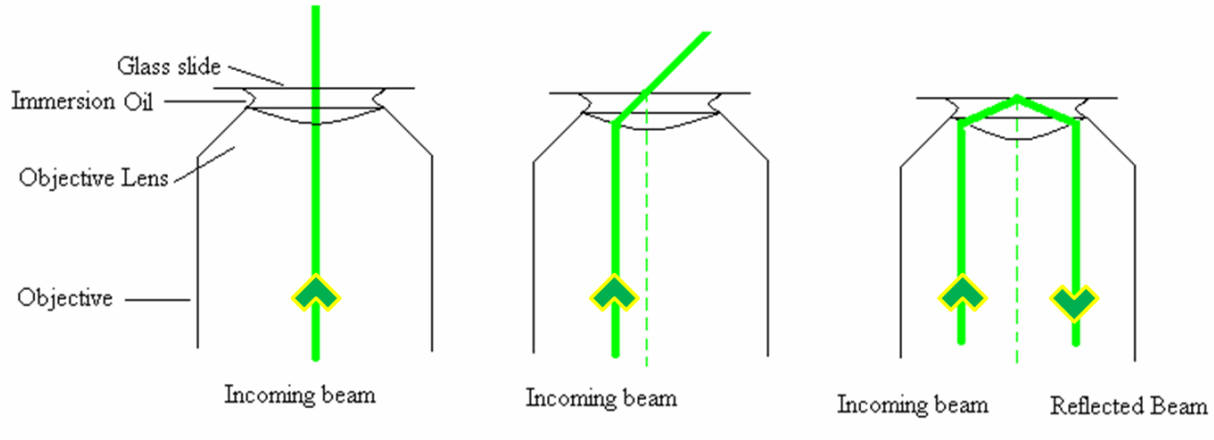

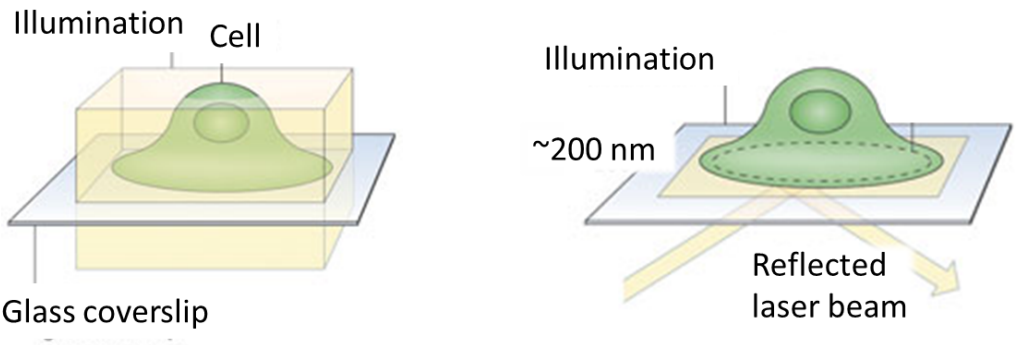

Figure 1.2. Structured illumination microscopy (SIM). The sample is illuminated with a pattern of sinusoidal stripes. The fine details of the structure, which were previously unresolvable, interact with the patterned light and form moiré fringes. The orientation and phase of the pattern is varied and the information from the moiré fringes is used to reconstruct the higher frequency information of the finer details of the structure. Image reproduced from Schermelleh *et al*..[36]

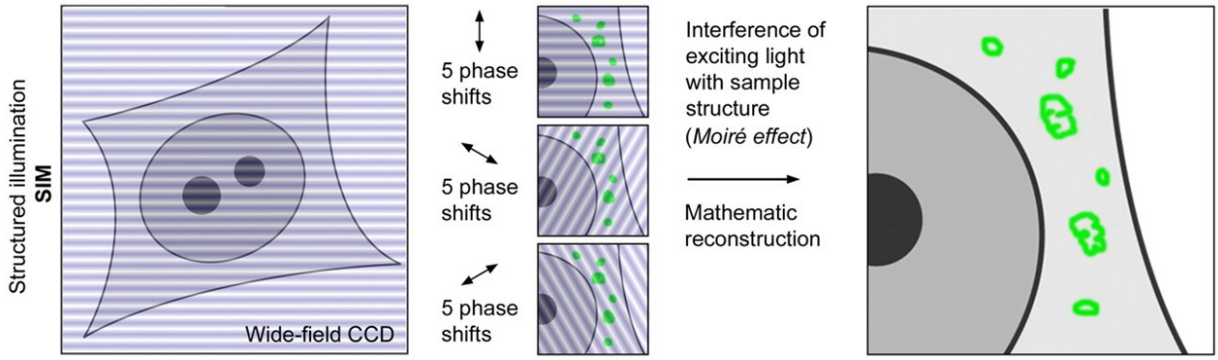

Figure 1.3. Locating a single molecule. The emission point-spread function (PSF) from one molecule can be well fit to a Gaussian or centroid function in order to precisely determine its location to ~5 nm in theory, ~20 nm in practice, depending on the number of photons collected.

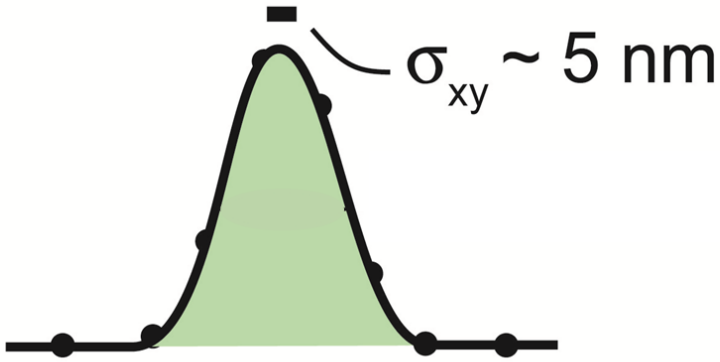

Figure 1.4. The diffraction limit. The emission PSF from an emitting molecule can be represented by an airy disk (yellow). Two molecules can be resolved if their PSFs are well separated (left). As the molecules get closer together, their PSFs begin to overlap until they are closer than the diffraction limit (right). The positions of these molecules can no longer be resolved. Figure reproduced from the web.[37]

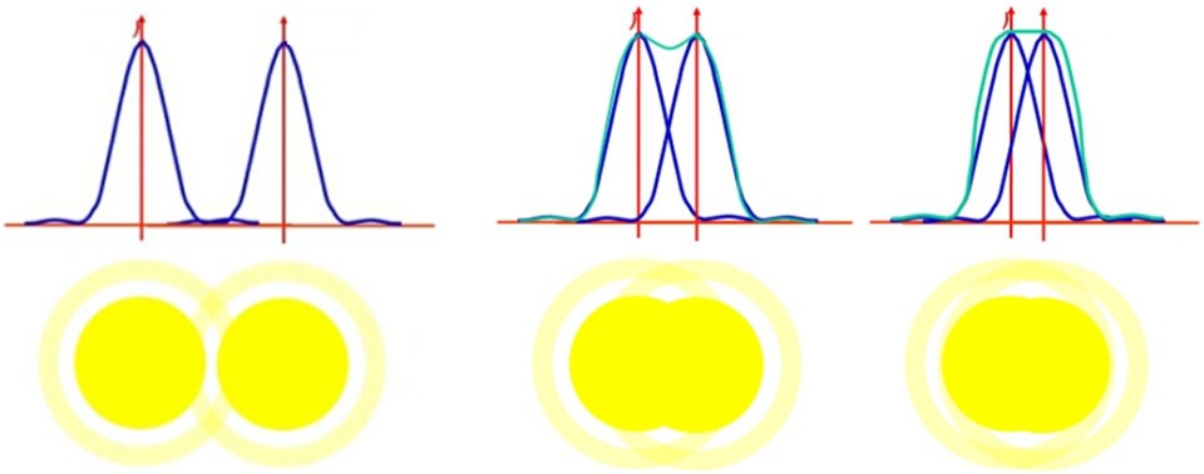

Figure 1.5. PALM experiment schematic using mEos2 as an example. Initially all of the mEos2 molecules emit green light when excited with 488 nm light. A sparse subset of labels is then activated using a small dose of the 405 nm (λ_1) activation laser. This changes the molecules' chromophore so that they now fluoresce in the orange channel when excited by 561 nm (λ_2) light. The number of molecules which activate is dependent on the dose of the activation laser. This is controlled so that there is a very low probability that the point spread functions of activated molecules overlap. These molecules are then excited by λ_2 until they bleach. A new subset of molecules is then activated and excited until they bleach. This cycle is repeated until either all of the molecules have been activated and bleached or sufficient data is collected to construct an image. Figure created by J. C. Weisshaar and then modified.

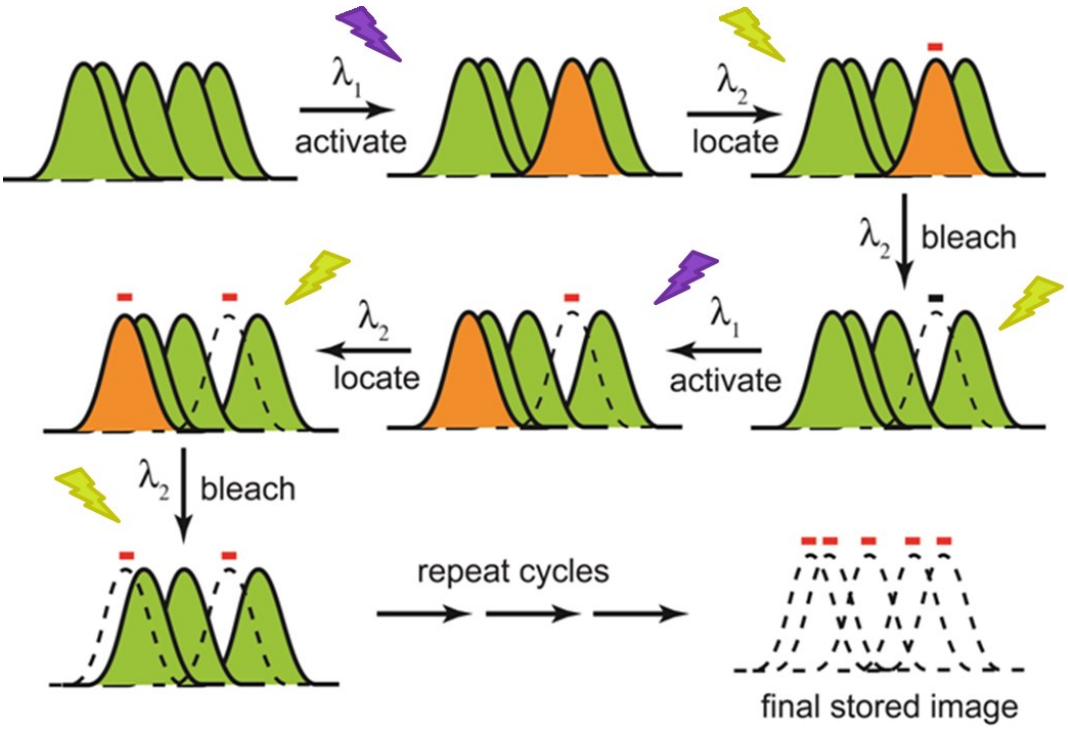

Figure 1.6. Homebuilt superresolution microscope setup. Optical schematic and microscope enclosure for maintaining temperature.

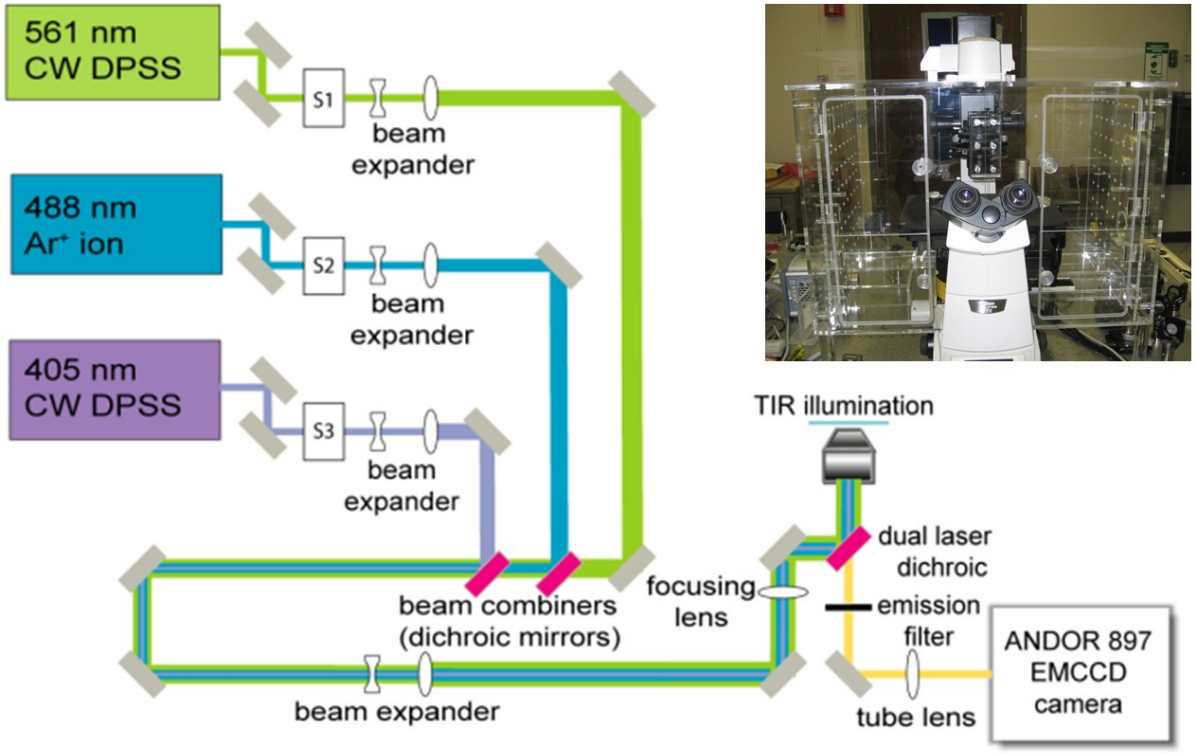

Figure 1.7. Homebuilt superresolution microscope.

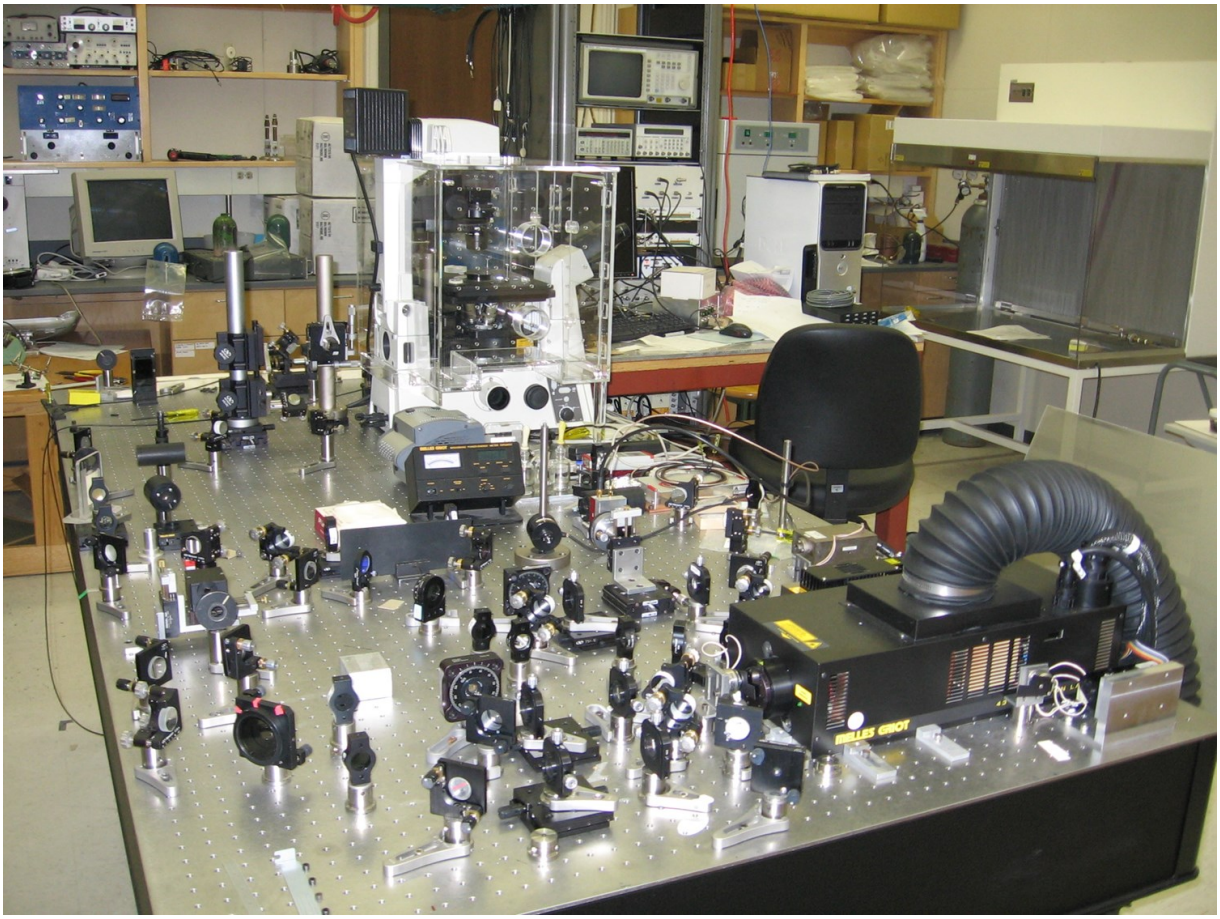

Figure 1.8. Schematic of dual-color and biplane device. For dual-color imaging the biplane lens is removed and emission filters are added to both light paths. Figure by Benjamin Bratton and Renée Dalrymple.

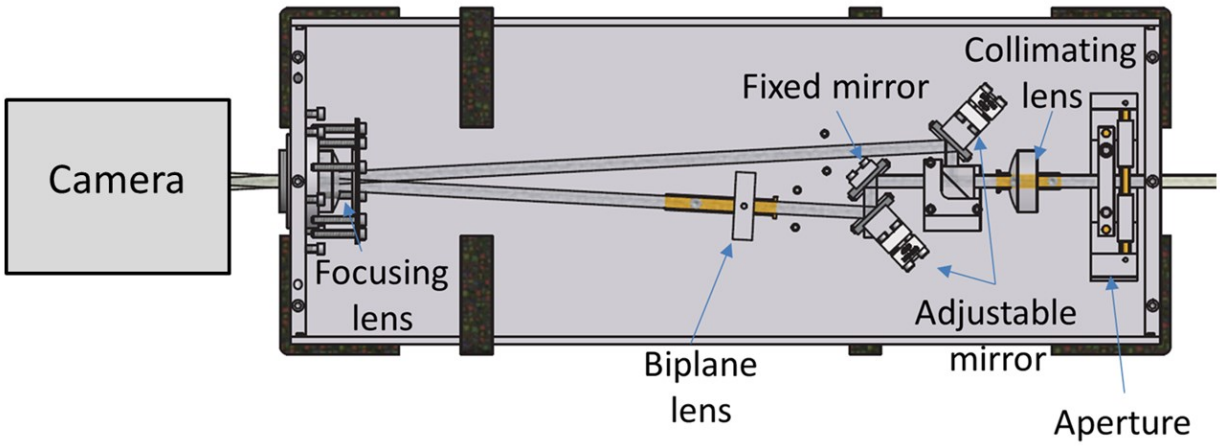

Figure 1.9. Dual color and biplane device.

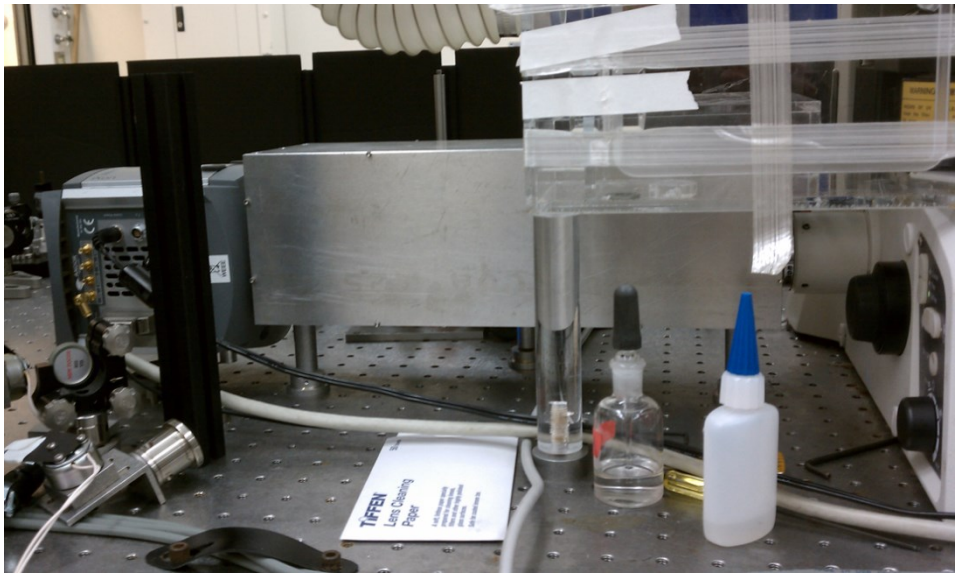

References

1 Abbe, E. Beiträge zur Theorie des Mikroskops und der mikroskopischen Wahrnehmung. *Archiv für mikroskopische Anatomie* **9**, 413-418 (1873).

2 Rayleigh, L. On the theory of optical images, with special reference to the microscope. *Philos. Mag.* **42**, 167-195 (1896).

3 Cremer, C. & Cremer, T. Considerations on a laser-scanning-microscope with high resolution and depth of field. *Microscopica acta*, 31-44 (1974).

4 Sheppard, C. & Wilson, T. The theory of the direct-view confocal microscope. *Journal of Microscopy* **124**, 107-117 (1981).

5 Heintzmann, R. & Cremer, C. G. 185-196.

6 Gustafsson, M. G. L. Surpassing the lateral resolution limit by a factor of two using structured illumination microscopy. *Journal of Microscopy* **198**, 82-87, doi:10.1046/j.1365-2818.2000.00710.x (2000).

7 Gustafsson, M. G. L. *et al.* Three-Dimensional Resolution Doubling in Wide-Field Fluorescence Microscopy by Structured Illumination. *Biophysical journal* **94**, 4957-4970 (2008).

8 Betzig, E. *et al.* Imaging Intracellular Fluorescent Proteins at Nanometer Resolution. *Science* **313**, 1642-1645, doi:10.1126/science.1127344 (2006).

9 Hess, S. T., Girirajan, T. P. K. & Mason, M. D. Ultra-High Resolution Imaging by Fluorescence Photoactivation Localization Microscopy. *Biophysical journal* **91**, 4258-4272 (2006).

10 Rust, M. J., Bates, M. & Zhuang, X. Sub-diffraction-limit imaging by stochastic optical reconstruction microscopy (STORM). *Nat Methods* **3**, 793-795 (2006).

11 McKinney, S. A., Murphy, C. S., Hazelwood, K. L., Davidson, M. W. & Looger, L. L. A bright and photostable photoconvertible fluorescent protein for fusion tags. *Nature Methods* **6**, 131-133 (2009).

12 Subach, F. V., Patterson, G. H., Renz, M., Lippincott-Schwartz, J. & Verkhusha, V. V. Bright Monomeric Photoactivatable Red Fluorescent Protein for Two-Color Super-Resolution sptPALM of Live Cells. *Journal of the American Chemical Society* **132**, 6481-6491, doi:10.1021/ja100906g (2010).

13 Heilemann, M. *et al.* Subdiffraction-Resolution Fluorescence Imaging with Conventional Fluorescent Probes. *Angewandte Chemie International Edition* **47**, 6172-6176, doi:10.1002/anie.200802376 (2008).

14 Dempsey, G. T., Vaughan, J. C., Chen, K. H., Bates, M. & Zhuang, X. Evaluation of fluorophores for optimal performance in localization-based super-resolution imaging. *Nature Methods* **8**, 1027–1036 (2011).

15 Thompson, R. E., Larson, D. R. & Webb, W. W. Precise nanometer localization analysis for individual fluorescent probes. *Biophys J.* **82**, 2775–2783 (2002).

16 Shannon, C. E. Communication in the Presence of Noise. *Proceedings of the Institute of Radio Engineers* **37**, 10-21 (1949).

17 Renz, M. & Lippincott-Schwartz, J. Single-Molecule Counting with Palm. *Biophysical journal* **100**, 350a, doi:http://dx.doi.org/10.1016/j.bpj.2010.12.2106 (2011).

18 Manley, S., Gillette, J. M. & Lippincott-Schwartz, J. in *Methods in Enzymology* Vol. Volume 475 (ed G. Walter Nils) 109-120 (Academic Press, 2010).

19 Juette, M. F. *et al.* Three-dimensional sub-100 nm resolution fluorescence microscopy of thick samples. *Nat Methods.* **5**, 527-529 (2008).

20 Bratton, B. P. *Dynamics of RNA Polymerase and DNA foci in live Escherichia coli* PhD thesis, University of Wisconsin, (2011).

21 Crocker, J. C. & Grier, D. G. Methods of digital video microscopy for colloidal studies. *Journal of Colloid and Interface Science* **179**, 298-310 (1996).

22 Kielar-Grevstad, D. M., Dalrymple, R. M., Weisshaar, J. C. & Martin., T. F. J. *Characterization of the Role of F-Actin in Neuroendocrine Secretion: Multiple Signals and Multiple Roles*.

23 Bakshi, S., Dalrymple, R. M., Li, W., Choi, H. & Weisshaar, J. C. *Partitioning of RNA Polymerase Activity in Live E. coli from Analysis of Single-molecule Diffusive Trajectories* (2013).

24 Wiggins, P. A., Cheveralls, K. C., Martin, J. S., Lintner, R. & Kondev, J. Strong intranucleoid interactions organize the Escherichia coli chromosome into a nucleoid filament. *Proceedings of the National Academy of Sciences* **107**, 4991-4995, doi:10.1073/pnas.0912062107 (2010).

25 Niki, H., Yamaichi, Y. & Hiraga, S. Dynamic organization of chromosomal DNA in Escherichia coli. *Genes & Development* **14**, 212-223, doi:10.1101/gad.14.2.212 (2000).

26 Roos, M. *et al.* Cellular localization of oriC during the cell cycle of Escherichia coli as analyzed by fluorescent in situ hybridization. *Biochimie* **81**, 797-802, doi:http://dx.doi.org/10.1016/S0300-9084(99)00218-7 (1999).

27 Bates, D. & Kleckner, N. Chromosome and Replisome Dynamics in E. coli: Loss of Sister Cohesion Triggers Global Chromosome Movement and Mediates Chromosome Segregation. *Cell* **121**, 899-911, doi:http://dx.doi.org/10.1016/j.cell.2005.04.013 (2005).

28 Wang, X., Possoz, C. & Sherratt, D. J. Dancing around the divisome: asymmetric chromosome segregation in Escherichia coli. *Genes & Development* **19**, 2367-2377, doi:10.1101/gad.345305 (2005).

29 Wang, X., Liu, X., Possoz, C. & Sherratt, D. J. The two Escherichia coli chromosome arms locate to separate cell halves. *Genes & Development* **20**, 1727-1731, doi:10.1101/gad.388406 (2006).

30 Nielsen, H. J., Li, Y., Youngren, B., Hansen, F. G. & Austin, S. Progressive segregation of the Escherichia coli chromosome. *Molecular Microbiology* **61**, 383-393, doi:10.1111/j.1365-2958.2006.05245.x (2006).

31 Nielsen, H. J., Ottesen, J. R., Youngren, B., Austin, S. J. & Hansen, F. G. The Escherichia coli chromosome is organized with the left and right chromosome arms in separate cell halves. *Molecular Microbiology* **62**, 331-338, doi:10.1111/j.1365-2958.2006.05346.x (2006).

32 Bakshi, S., Bratton, Benjamin P. & Weisshaar, J. C. Subdiffraction-Limit Study of Kaede Diffusion and Spatial Distribution in Live Escherichia coli. *Biophysical journal* **101**, 2535-2544 (2011).

33 Bakshi, S., Siryaporn, A., Goulian, M. & Weisshaar, J. C. Superresolution imaging of ribosomes and RNA polymerase in live Escherichia coli cells. *Molecular Microbiology* **85**, 21-38, doi:10.1111/j.1365-2958.2012.08081.x (2012).

34 <http://www.biophysics.leidenuniv.nl/fvl/Theses/EmanuelaFesta.pdf>

35 Balagopalan, L., Sherman, E., Barr, V. A. & Samelson, L. E. Imaging techniques for assaying lymphocyte activation in action. *Nature Reviews Immunology* **11**, 21-33 (2011).

36 Schermelleh, L., Heintzmann, R. & Leonhardt, H. A guide to super-resolution fluorescence microscopy. *The Journal of Cell Biology* **190**, 165-175, doi:10.1083/jcb.201002018 (2010).

37 *Resolution*, <http://astronomy.swinburne.edu.au/cms/astro/cosmos/R/Resolution>

Chapter 2

Superresolution imaging of the F-actin cytoskeleton in PC12 cells

This work was done in collaboration with Elle Kielar-Grevstad in Tom Martin's group in the UW Madison Biochemistry Department. Elle prepared the samples, we collectively designed the experiments and performed the imaging, and I processed the data and constructed the images.

Introduction

Exocytosis is an extremely important process by which eukaryotic cells release contents from a secretory vesicle to the extracellular space or cell membrane. For example, in the case of neuronal exocytosis the contents may be neurotransmitters which are delivered to a receptor site across the synapse, thus allowing the brain to pass messages to the rest of the body (Figure 2.1). Regulated exocytosis occurs in response to a stimulus and an increase in intracellular calcium, Ca^{2+}. This can be invoked by an increase in K^{+} which depolarizes the cell membrane and causes Ca^{2+} channels to open.

There are numerous factors which have been implicated in regulating exocytosis, one of which is the actin cytoskeleton.[1] The cytoskeleton contains filamentous actin (F-actin).

Individual fibers are ~7 nm in diameter and form bundles. Vesicles have been seen to reside in cage-like structures of F-actin (Figure 2.2).[2-5] Upon cell stimulation F-actin has been shown to reorganize its structure.[6,7] This has been shown in PC12 cells (pheochromocytoma cell 12) with widefield total internal reflection fluorescence (TIRF) microscopy by the Martin lab.[8] They simultaneously monitored single vesicle dynamics and the F-actin cytoskeleton before, during, and after cell stimulation with K^+. They observed that the intensity of the F-actin signal in the cell first decreases and then increases again, suggesting a breakdown of the F-actin structure followed by reformation. While the F-actin structure has been studied by TIRF microscopy, the resolution of these images is on the order of 250 nm, so the details of the structure cannot be resolved.

The actin cytoskeleton has been imaged at high resolution in chromaffin cells using electron microscopy (EM).[5] It has also been imaged in epithelial and fibroblast cells using 3D dual-objective STORM; however, the location of the vesicles has not been simultaneously imaged.[9] In this work we describe the use of superresolution fluorescence microscopy to image the F-actin structure and its response to stimulation in PC12 cells. Dual color imaging was used to also image the vesicles and see how their locations relate to the F-actin structure.

Materials and methods

Cell culture

PC12 cells were cultured in Dulbecco's modified Eagle's medium supplemented with 5% horse serum and 5% calf serum at 10% CO_2 and 37 °C.

Labeling scheme

F-actin was imaged using the actin binding molecule Alexa Fluor 647 phalloidin, hereafter called Alexa 647 phalloidin. This molecule is commercially available (Life Technologies) and widely used for actin labeling. Alexa 647 is a very suitable dye for the superresolution imaging technique dSTORM because it undergoes rapid photoswitching in the proper imaging conditions. For dual color experiments where the vesicles were labeled, chromogranin B (CgB), a secretory vesicle content protein, was stained with Atto 488.

Immunocytochemistry

Cells were plated on poly-DL-lysine and collagen coated glass bottom dishes (MatTek Corp.) and left overnight in media. They were then washed once in 2 mL of cytoskeletal buffer (CB) (10 mM MES, 150 mM NaCl, 5 mM EGTA, 5 mM Glucose, 5mM $MgCl_2$; pH 6.1). They were then fixed for 15 min in 4 % formaldehyde and washed once with CB + 0.1 M Glycine. Fiducial markers (100 nm TetraSpeck Fluorescent Microspheres, Invitrogen) were added at a 1:200 dilution in CB and allowed to sit overnight at 4 ^{o}C. The addition of the fiducial markers at this point in the sample preparation was determined to be critical to their ability to adhere to the surface. The cells were then permeabilized and blocked with 0.5 mL of 10 % FBS with 0.2 %

TritonX-100 in CB for 30 min at room temperature. For dual color labeling of the vesicles and F-actin, chromogranin B (CgB), a secretory vesicle protein was stained. The cells were washed once with CB buffer and then stained with the primary CgB monoclonal antibody (Pel-Freeze Biologics) at a 1:1000 dilution for one hour at room temperature. They were rinsed twice with CB, then stained with the secondary antibody (1:100 dilution of Atto-488 GAM IgG1 (Enzo)) as well as the F-actin stain (1:50 dilution of Alexa 647 phalloidin (Molecular Probes) for one hour at room temperature. They were then rinsed once with CB and fixed again with 4 % formaldehyde for 15 min at room temperature. They were then put in CB + 0.1 M Glycine and stored at 4 °C until imaging.

Samples were prepared similarly for dSTORM imaging of the vesicles labeled with Alexa 647 (secondary antibody Alexa 647 goat-anti-mouse IgG).

dSTORM imaging

For proper photoswitching of the dyes to occur, a special imaging buffer must be used. This buffer contains a reducing agent (MEA) and an oxygen scavenging system (glucose oxidase and catalase) to minimize photobleaching. Imaging buffer was made fresh on ice before each sample was imaged. It contained 100 mM MEA for Alexa 647 imaging (2 mM for Atto 488 dSTORM imaging), 0.7 mg/mL Glucose Oxidase, 0.34 mg/mL Catalase), and 0.1 mg/mL glucose in TN buffer (50 mM Tris 10 mM NaCl pH 8.0).

Immediately before imaging, the cells were rinsed once with TN buffer and then 180 uL of imaging buffer was added to the well of the MatTek dish. The well was covered with a glass coverslip and sealed with vacuum grease (Figure 2.3). This allowed the same sample dish to be

imaged more than once since the sealing coverslip could be removed and the imaging buffer replaced.

dSTORM images were acquired using an N-STORM system by Nikon in total internal reflection fluorescence (TIRF) mode using a Nikon Apo TIRF 100x/1.49 Oil objective (MRDO1991). Alexa 647 and Atto 488 were excited with 647 nm and 488 nm lasers on an Agilent Technology MLC 400B laser launch. Laser powers were adjusted to maintain a sparse density of fluorescent molecules while optimizing the signal to noise level. The power density of the 647 nm beam was ~1-3 kW/cm^2. 16 ms frames were taken continuously for 40,000 frames or until switching had ceased. The emission was focused on an Andor iXon Ultra 897 EMCCD camera. Image acquisition was controlled with Elements AR 4.13.04. The Nikon Perfect Focus System was used to minimize drift in z.

Data analysis

Locating molecules and superresolution image generation

Data analysis was accomplished using a custom peak finding and tracking program in MATLAB as described earlier.[10] Briefly, the raw data was smoothed using a bandpass filter in order to obtain a zero-based image. A single pixel intensity threshold was used to determine which bright spots were molecules (Figure 2.4). The molecules' sub-pixel locations were determined by finding the centroid of the diffraction limited spots. Molecules persisting for multiple frames were linked into a trajectory using a modified MATLAB version of the tracking program written by Crocker and Grier.[11]

In order to account for sample drift over the course of the experiment, 100 nm diameter fiducial markers (TetraSpeck beads, Invitrogen) were tracked throughout the course of the experiment. A linear transformation of the molecules' position data was performed by subtracting the average displacement of the fiducials on a per frame basis. This appeared to be sufficient for our system, but more complicated algorithms could be applied in the event of warping or nonlinear movement of the sample.

Once the drift corrected subpixel locations of the molecules were determined, the superresolution image was generated. A frequency histogram was constructed with a 20 nm by 20 nm pixel size. Each time a molecule's position was found in a particular pixel the count in that pixel increased. Molecules often last for more than one frame before they bleach. Only the first frame in which the molecule was present was plotted in order to avoid counting the same switching event twice. If the molecule is lost for a frame and then returns, it was counted as a new molecule.

In order to overlay a widefield image on the superresolution image, the widefield image was scaled up to the same size as the superresolution image. For example, if the pixel size in the widefield image was 100 nm and it was 20 nm for the superresolution image, the widefield image was scaled by five. The widefield image was then linearly transformed so that the fiducials, which were visible in both images, were aligned.

Results

Superresolution imaging of F-actin in PC12 cells

Superresolution images of F-actin in resting cells show large filamentous structures as well as an underlying web-like structure (Figure 2.5). These large fibers range from ~45-83 ± 9 nm in width and likely represent bundles of single fibers.

Strong stimulation changes the F-actin structure

In order to see the differences in F-actin structure after stimulation, cells were stimulated with 95 mM K^+ and then immediately fixed at different time points: within 20 seconds and after two minutes. Cells fixed after 20 seconds had lost the larger filamentous structures while the web-like structures remained (Figure 2.6). After two minutes the filaments had begun to reform (Figure 2.7). This is the first time the effects of stimulation on the F-actin structure have been seen at this resolution in PC12 cells.

F-actin fibers are still evident with lower molecule density

There were considerably fewer molecules detected for the sample fixed 20 seconds post-stimulation. This could be due to the depolymerization of F-actin from stimulation, or it could be due to lower labeling density of that particular sample. If the labeling density becomes too low the Nyquist-Shannon sampling criterion may no longer be met and the F-actin fibers may not be resolved.[12] In order to test if F-actin fibers would still be resolvable at that molecule density, the data from the pre-stimulation cell in Figure 2.5 was rendered with only a fraction of the molecules (~8%) so that the number of molecules/pixel approximately matched that of the 20

s post-stimulation cell (Figure 2.8). While they are less pronounced, the fibers are still visible in this rendering and it looks significantly different from the 20 s post-stimulation cell. The fact that the F-actin structure looks different 20 s after stimulation is not an artifact of detecting fewer molecules.

Vesicles reside in areas of lower F-actin density

In order to see how the locations of vesicles relate to the actin structure, dual color imaging was performed. A widefield TIRF image of the vesicles was taken and then dSTORM imaging of F-actin was performed. The widefield image was overlayed on the rendered dSTORM image. Visually, it appears that vesicles often reside in areas devoid of actin (Figure 2.9). It is difficult to quantify the extent of their anticorrelation because it is complicated by the fact that there are multiple layers of actin. The TIRF field likely extends ~200 nm into the sample and the vesicles are approximately 100 nm in diameter. This means that it is possible to have a layer of actin above the vesicle. This would make the vesicle appear to be colocalized with actin in *x* and *y* when they could in fact be in different *z* planes. The fact that the vesicles appear to be in areas devoid of actin is likely an underestimation of the extent of their anticorrelation.

In order to determine how often this actually occurs, 3D imaging could be performed. This would be possible using either astigmatism, which is available on the N-STORM system used here, or Biplane PALM, for which a device has been constructed in our lab. This would provide approximately 50 nm resolution in z and may help determine the degree of anticorrelation more accurately.

Measurement of vesicle diameter

In order to more precisely measure the size of the vesicles, dSTORM imaging of CgB labeled with Alexa 647 was performed. It became clear that bright vesicles in the widefield TIRF image often consist of multiple vesicles when imaged using dSTORM (Figure 2.10). Well isolated vesicles were determined to have an average diameter of 134 ± 40 nm. This was accomplished by drawing a linescan through the dSTORM image of well isolated vesicles and measuring their FWHM (Figure 2.11). The average FWHM was found to be 95 ± 25 nm (Figure 2.12). The FWHM is not an accurate measure for the diameter of the vesicles because it systematically underestimates their size.

In order to correct for this underestimation, a simulation was performed in which spheres of varying diameters (20-400 nm at 10 nm intervals) were filled with random positions to represent the distribution of the vesicle content labels in the experiment. Since there is localization error present in the measured molecule position data, error was added to these positions (Figure 2.13). Random numbers from a Gaussian distribution with standard deviation, σ were added to the positions in the sphere. A histogram of these simulated positions with error was then generated along one dimension (y) to simulate a linescan through the vesicle. The data was binned with 20 nm bin widths to match the pixel size of the rendered dSTORM images. The FWHM of these histograms was then measured by interpolating between the bin heights to get the values at the half maximum of the histogram (Figure 2.14, top). This simulation was done for 500 spheres of each size. Their measured FWHM was plotted verses the actual diameter. This was repeated for different values of σ (Figure 2.14, bottom). When the localization error is small there is a linear relationship between the measured FWHM and the actual diameter. When

the localization error becomes larger relative to the diameter, the curves begin to flatten out. This adds uncertainty to the measurement. This simulation was used as a calibration curve to convert the measured FWHM of the vesicles to the true vesicle diameter.

In order to obtain the actual vesicle diameters we must have a measure for σ. Ideally, multiple switching events of the same molecule would be used to measure the precision with which the molecule is detected, however this would not include the contribution of the drift correction over the entire acquisition. For this reason, the localization error of the fiducial markers was used. This is a good proxy for the localization error because they are somewhat comparable in brightness to the single molecules. At the beginning of the acquisition the fiducials were brighter than the molecules, but they bleach throughout the acquisition until they are actually dimmer than the single Alexa 647 molecules. The positions of the fiducials throughout the entire acquisition were included in this analysis.

The standard deviations of the *x* and *y* positions of the fiducials were measured by determining the FWHM of a histogram of their positions (5.3 nm bins) and converting to σ using $FWHM = 2\sqrt{2\ ln2}\sigma$. The average σ was found to be 8.7 ± 1.7 nm (Figure 2.15). The true diameters of the vesicles were then determined using the simulated calibration curve with σ = 10 nm. A straight line was fit to this curve (Figure 2.16). Given the average measured FWHM of 95 ± 25 nm the true average vesicle diameter was found to be 134 ± 40 nm.

Two color dSTORM imaging of F-actin and vesicles

Two color dSTORM was performed in order to see more accurately where the vesicles are located relative to the actin structure. Actin was imaged using Alexa 647 phalloidin and the

vesicle protein CgB was stained with Atto 488. We did not have great success getting Atto 488 to photoswitch. The signal to noise of the images was reduced because it appeared that there was a haze of fluorescence present. This was likely due to molecules which were not being switched to the dark state. It is possible that increasing the laser power would help with this problem; however, this would require the purchase of a higher power laser. Another problem may be that the imaging buffer needs to be further optimized. Different concentrations of the reducing agent (MEA) were tried. Of the concentrations tested, it was found that 2 mM provided the best photoswitching. However, this is not the ideal concentration for Alexa 647 (100 mM) (Figure 2.17). Further work is necessary to achieve a good quality dual color dSTORM image. Imaging buffer conditions can be optimized or different fluorophores such as Cy3b can be used to stain the vesicles.

Discussion and conclusions

F-actin rearranges upon stimulation

It has been shown that the F-actin structure is disrupted upon stimulation in several cell types.[6,7] Widefield fluorescence microscopy and electron microscopy of chromaffin cells have shown that areas of F-actin disassemble upon stimulation with nicotine.[5,6] The rearrangement of F-actin upon stimulation has been observed simultaneously with vesicle fusion events in PC12 cells using TIRF microscopy.[8] The total fluorescence signal in the cell was seen to decrease upon stimulation and then increase within about a minute indicating depolymerization and then repolymerization.[8] In this work we show never before observed superresolution images of the pre and post stimulation F-actin structure in PC12 cells.

We observe that prior to stimulation there are large F-actin fibers present. At 20 s post stimulation these large fibers have depolymerized and are completely absent from the structure. It should be noted however, that not all of the F-actin has depolymerized, as the underlying "web" of F-actin remains. This structure likely provides the cages in which docked vesicles reside. Our results show that 20 s post stimulation vesicles still appear to reside in areas of decreased F-actin density. These results agree with a study by Giner *et al.* from 2005 in which they observed that upon depolarization with 59 mM KCl the cortical cytoskeleton disassembles. F-actin was observed to be transferred from the cortical area to the cytosol. It was hypothesized that the previously horizontal fibers reoriented forming channel-like structures perpendicular to the cell membrane.[7] These channels could be used to shuttle vesicles to the surface and appear as the web like structure observed here. This idea that the actin moves from the cell surface towards the interior is consistent with the disruption of the F-actin structure observed here, and the fact that there were fewer Alexa-647 phalloidin molecules observed at the surface 20 s after stimulation.

At 120 s post stimulation the large F-actin fibers have repolymerized, which is consistent with previous observations. Giner *et al*. saw that the F-actin structure recovers in 80-100 seconds in chromaffin cells, and Kielar-Grevstad *et al.* made similar observations in PC12 cells.[7,8] This repolymerization acts as an important regulator of the fusion process. When repolymerization of F-actin is blocked, there is an increase in the number of fusion events.[8] Apparently these fibers serve as a barrier to further fusion events.

Vesicles are found in F-actin cages

The F-actin structure and its relationship to secretory granules has been studied by a variety of methods. None of them provide a high resolution picture of its structure as well as the locations of the vesicles, as is demonstrated here. F-actin has been shown to have a cage-like structure by a number of studies.[2-5] The F-actin cage size in chromaffin cells has been measured to be ~600 nm diameter in the cell interior and ~400 nm diameter in the cortical region.[3] The structure of F-actin and the size of the cages were found to affect vesicle movement with vesicles moving more in areas in the interior of the cell with larger cages. Vesicle movement is mostly restricted at the cell surface, possibly due to the small F-actin cages.[8]

These cages have been found to be sites of exocytosis in chromaffin cells.[2] Components of the secretory machinery, syntaxin-1 and synaptotagmin-1, and voltage-dependent Ca^{2+} channels (VDCCs) were found at the borders of the cages. Our results show that vesicles are in fact located in cage like structures and hint that perhaps the vesicles are located nearer the edges of the cages than in the center. In order to truly investigate this, in the future, the dual color superresolution studies should be perfected.

Vesicle diameter measurements match those from EM studies

Here we provide the first superresolution fluorescence measurements of the diameter of PC12 cell vesicles. Previously, Lang *et al.* measured PC12 cell vesicle diameters using deconvolution of a confocal image. A line scan was drawn through the intensity from a dense-core granule in the z dimension. They obtained a FWHM of 380 ± 10 nm.[13] This measurement is artificially large due to the limited resolution of the system, especially in the z dimension in

which the measurement was made. Our work improves this resolution and achieves a measurement (134 ± 40 nm) which is much closer in value to those made by electron microscopy (EM) by Schubert *et al.* (158 ± 1 nm diameter) and Tooze *et al.* (120 nm core diameter).[14,15] The fact that our results verify those from EM is comforting considering the vast differences in sample preparation. Our results however, are still from fixed cells so we cannot rule out the possibility that there may be artifacts from fixation in the measurements. In the future, it is feasible to repeat these measurements in live cells since the vesicles at the cell surface are generally not very mobile.

Figures

Figure 2.1. Cartoon of the synapse with vesicle fusion event circled in red. Image altered and reproduced from the web.[16]

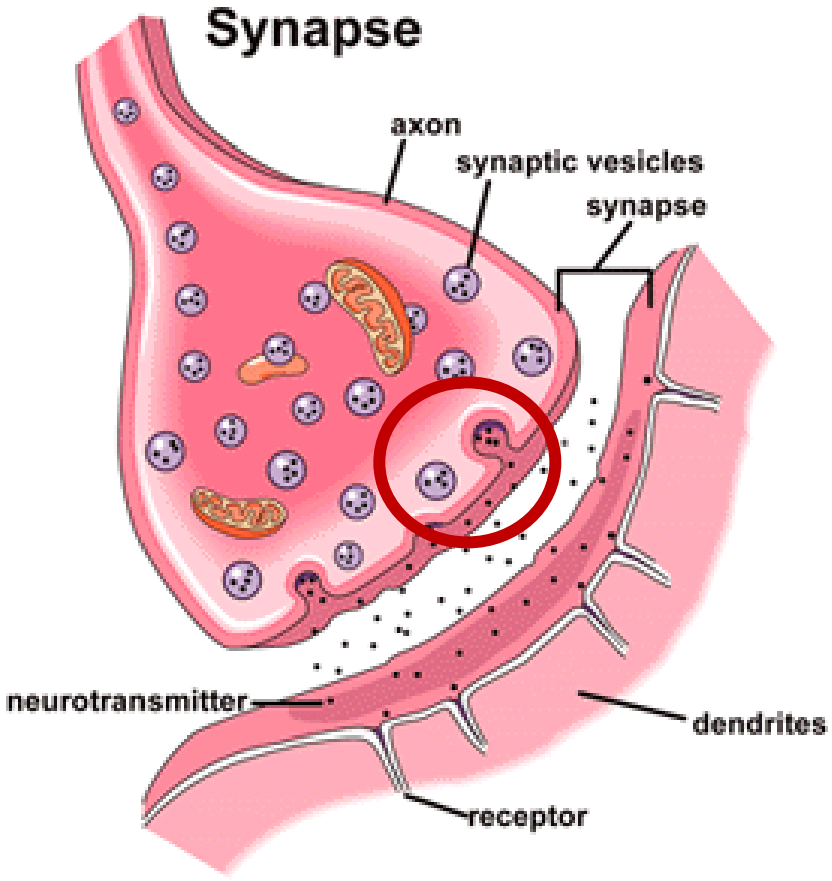

Figure 2.2. Schematic of a PC12 cell with F-actin in green and vesicles in yellow. Vesicles reside in areas of less dense F-actin. Figure reproduced with alterations from the web.[17]

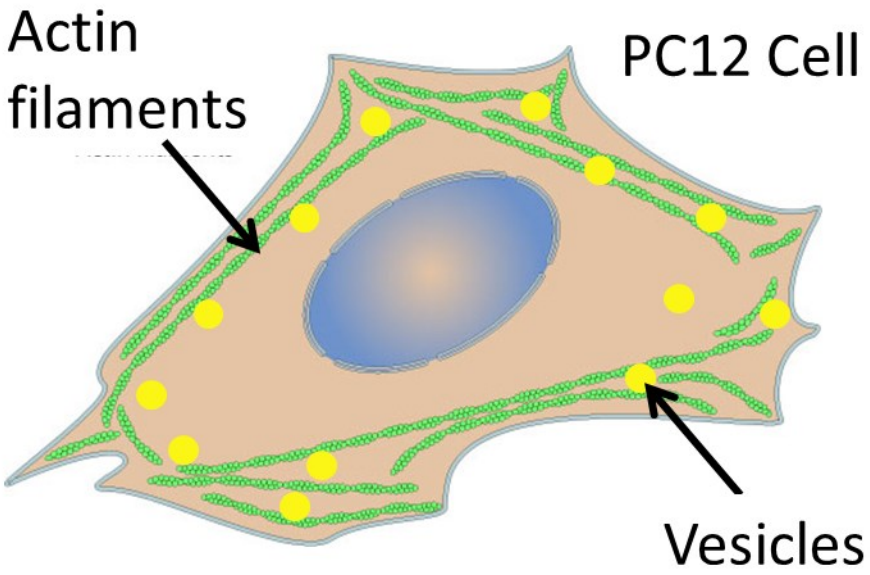

Figure 2.3. Image of prepared chamber. Cells were plated in the well of a glass bottom dish (MatTek Corp.). For imaging, 180 μL of imaging buffer was added to the well. Vacuum grease was used to seal a coverslip on top of the well.

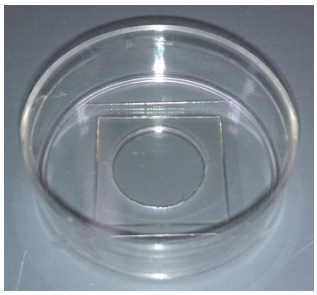

Figure 2.4. Custom analysis program for peak finding, tracking, and drift correction (written by Colin Ingram and modified to add drift correction for this work). **(Top)** Example of a frame of raw data. **(Middle)** The same frame as in **(Top)** that has been smoothed using a bandpass filter. **(Bottom)** Detected molecule centers and blue boxes in which centroid fitting was performed.

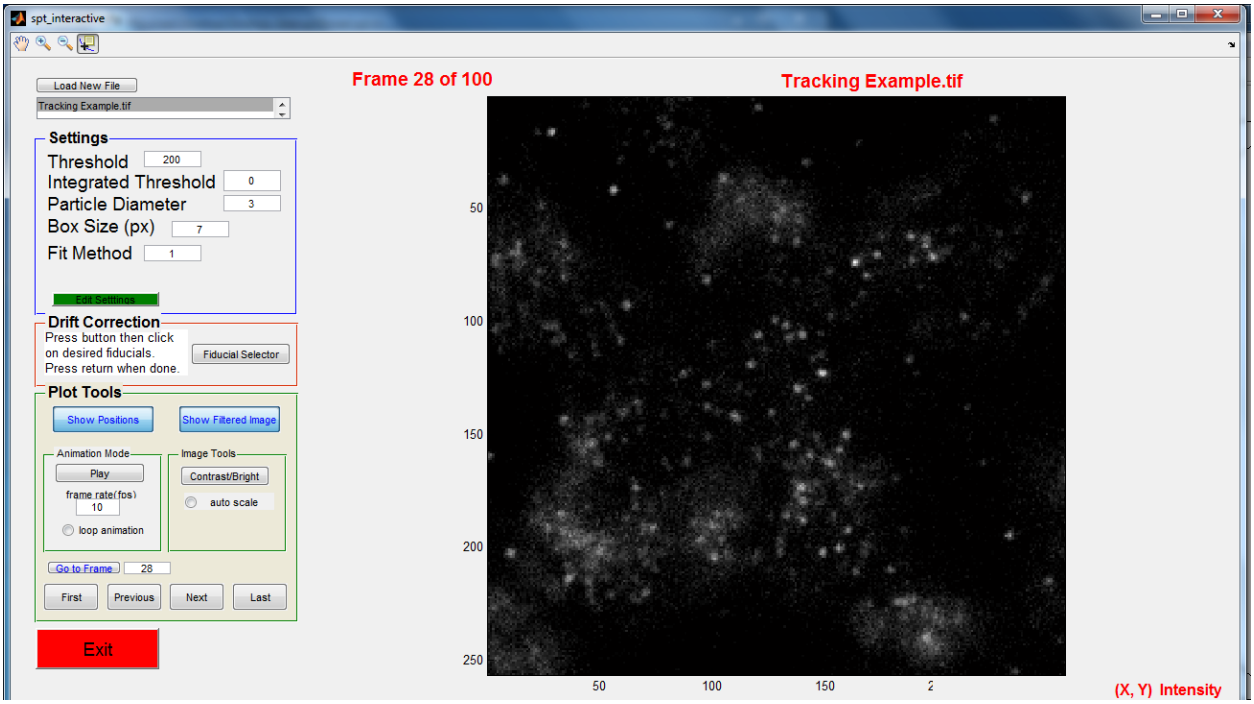

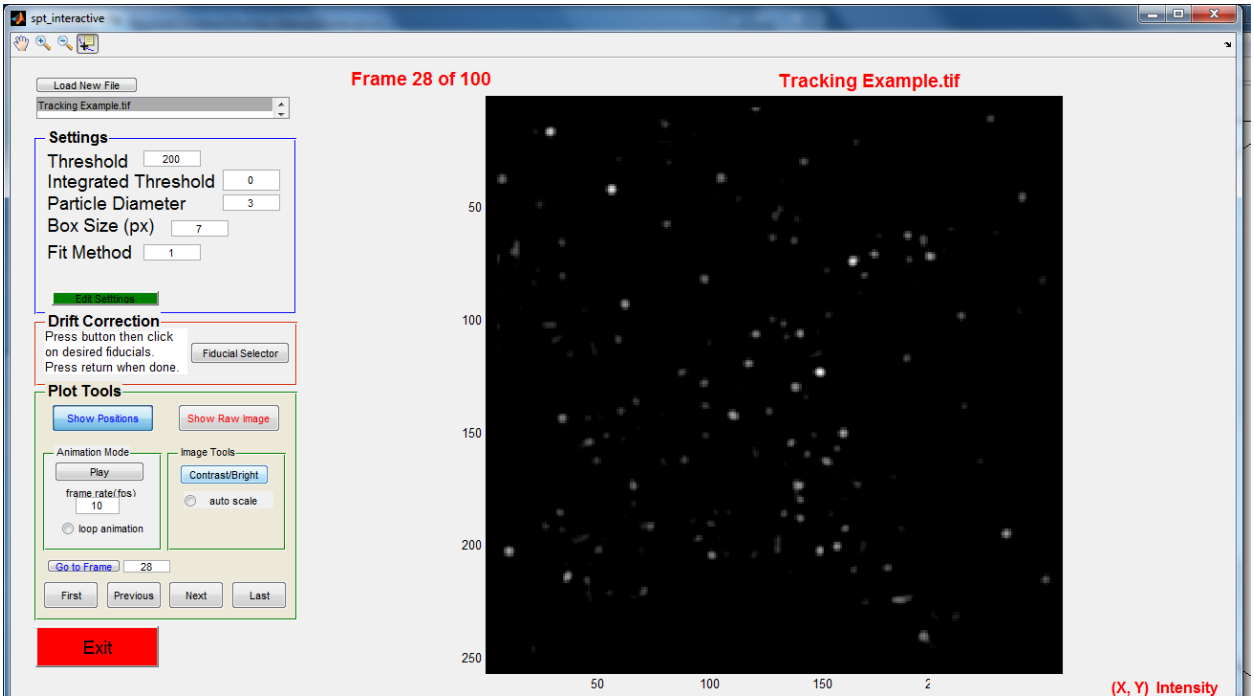
spt_interactive
Load New File
Tracking Example.tif
Settings
Threshold 200
Integrated Threshold 0
Particle Diameter 3
Box Size (px) 7
Fit Method 1
Edit Settings
Drift Correction
Press button then click on desired fiducials. Press return when done.
Fiducial Selector
Plot Tools
Show Positions
Show Raw Image
Animation Mode
Play
frame rate(fps) 10
loop animation
Image Tools
Contrast/Bright
auto scale
Go to Frame 28
First
Previous
Next
Last
Exit
Frame 28 of 100
Tracking Example.tif
50
100
150
200
250
50
100
150
(X, Y) Intensity

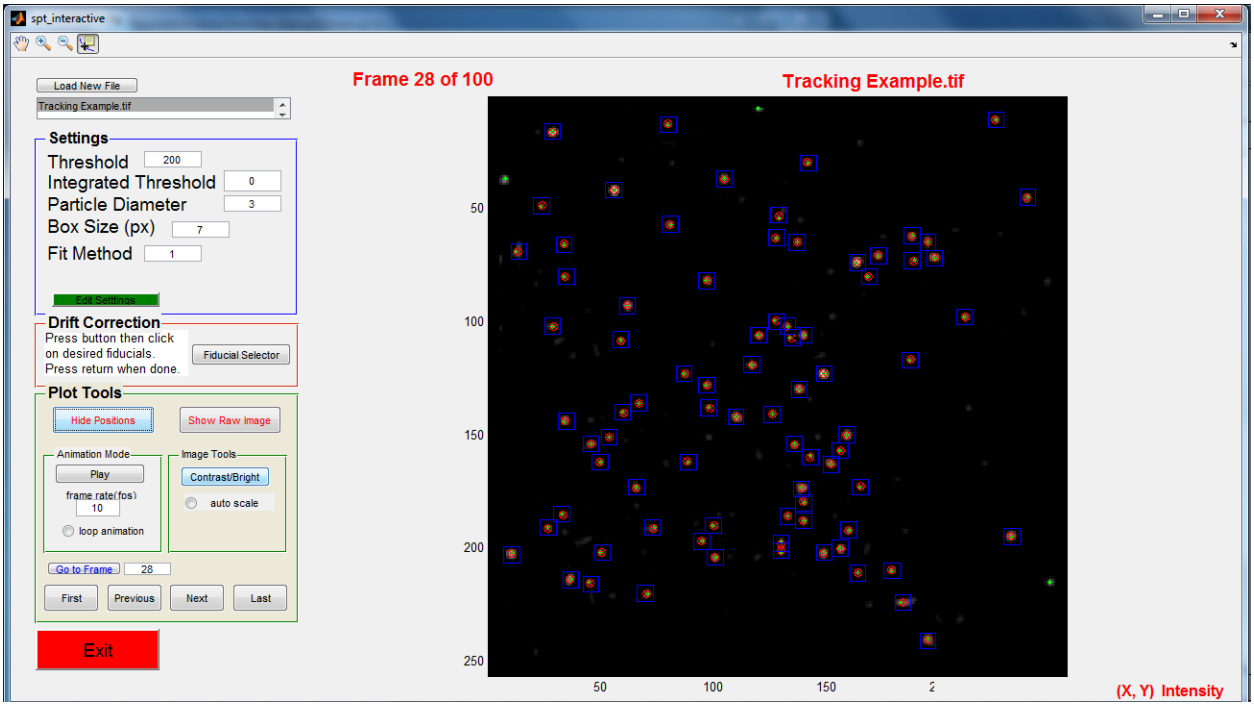
spt_interactive
Load New File
Tracking Example.tif
Settings
Threshold 200
Integrated Threshold 0
Particle Diameter 3
Box Size (px) 7
Fit Method 1
Edit Settings
Drift Correction
Press button then click on desired fiducials. Press return when done.
Fiducial Selector
Plot Tools
Hide Positions
Show Raw Image
Animation Mode
Play
frame rate(fps) 10
loop animation
Image Tools
Contrast/Bright
auto scale
Go to Frame 28
First
Previous
Next
Last
Exit
Frame 28 of 100
Tracking Example.tif
50
100
150
200
250
50
100
150
(X, Y) Intensity

Figure 2.5. Example of the increased resolution of dSTORM imaging compared to widefield TIRF. **(Left)** Conventional widefield TIRF image of Alexa 647 phalloidin in a resting cell. **(Right)** dSTORM image of the cell at left. **(Bottom)** Zoomed in region shows the presence of large F-actin fibers or bundles.

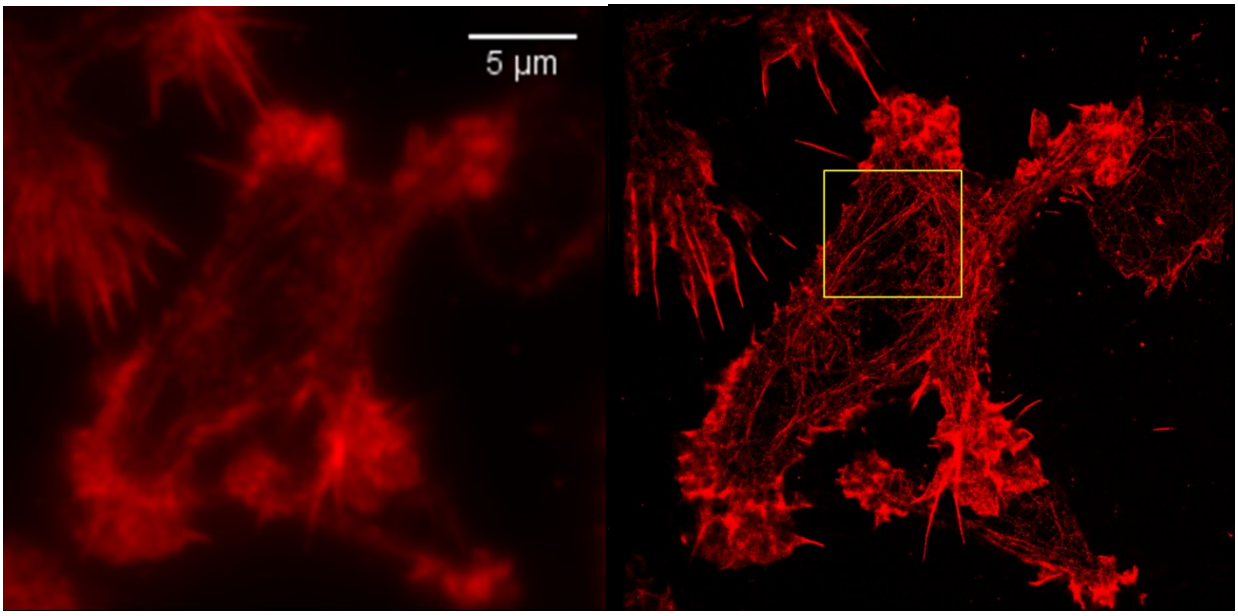

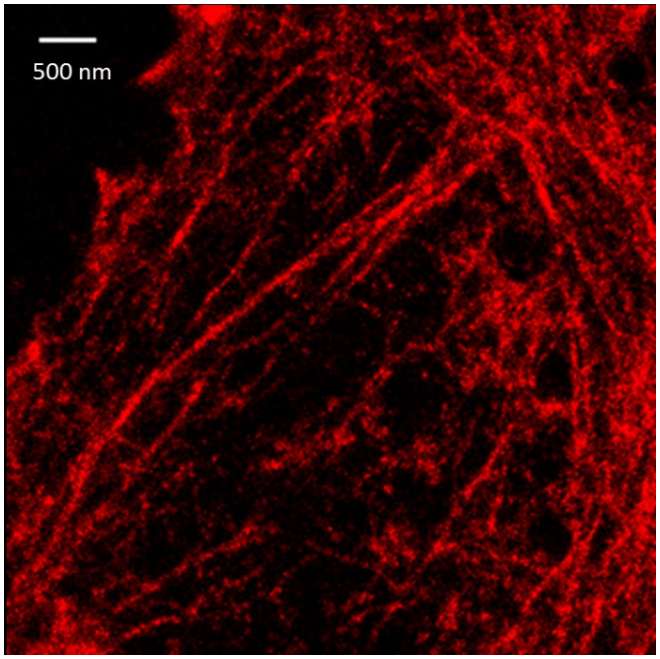

Figure 2.6. Large F-actin fibers are lost 20 s after stimulation. **(Top)** dSTORM image of a cell 20 s post-stimulation. **(Bottom)** Zoomed in region showing loss of fibers, but retention of small scale web like organization.

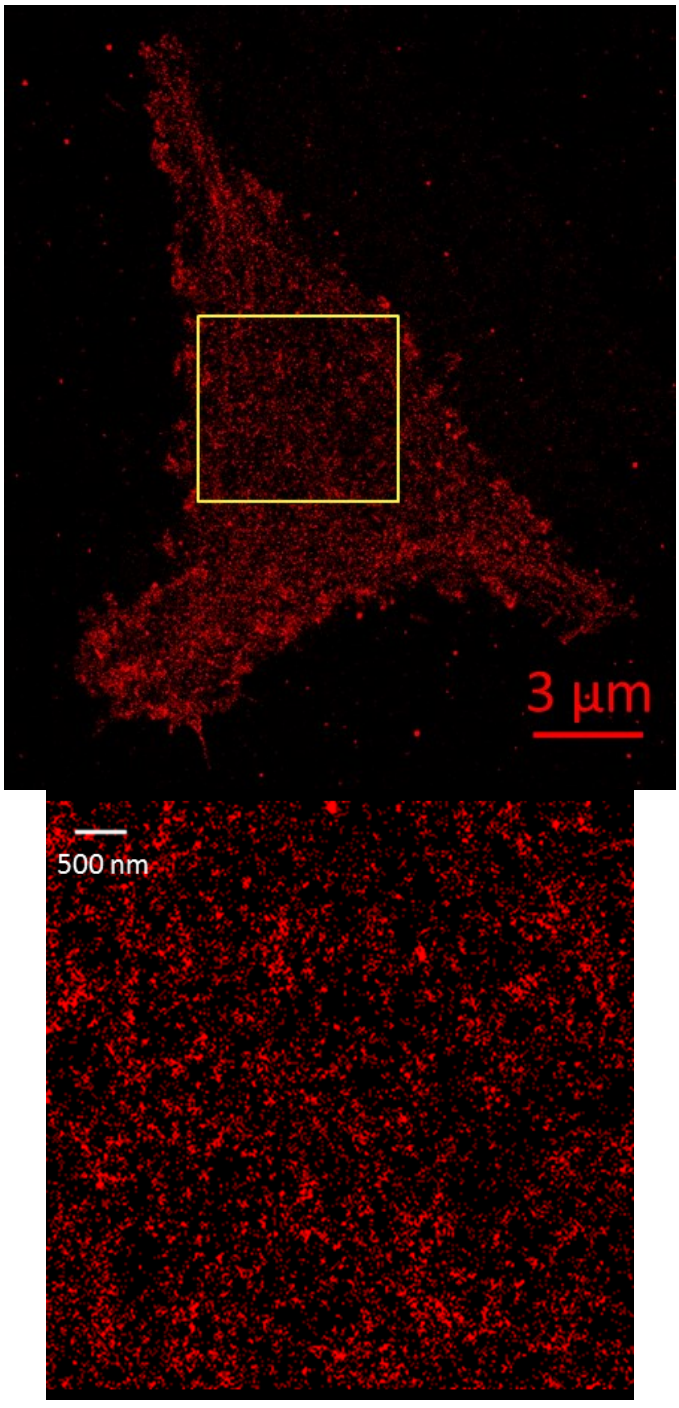

Figure 2.7. Large fibers repolymerize after 120 s. **(Top)** dSTORM image of a cell 120 s post-stimulation. **(Bottom)** Zoomed in region showing reformation of large fibers.

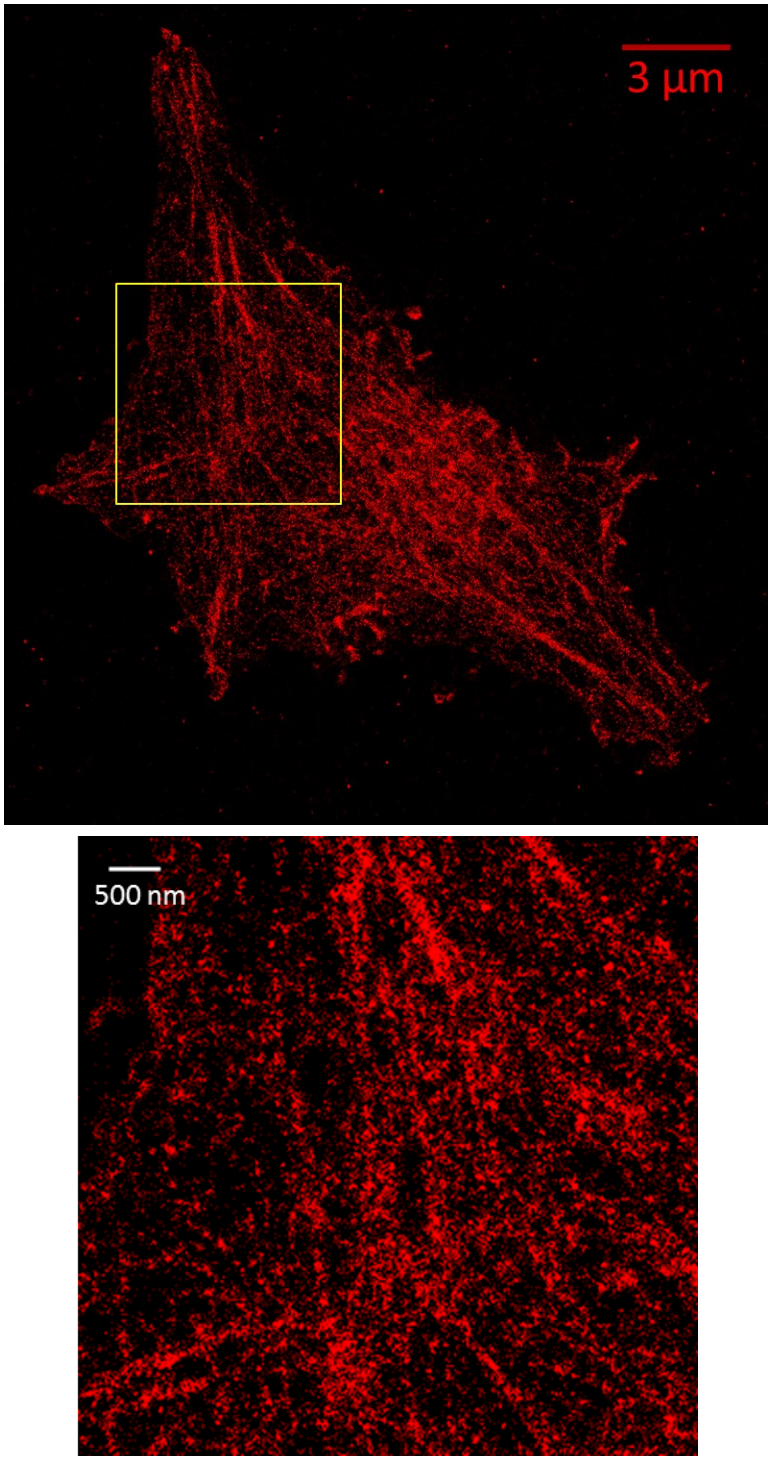

Figure 2.8. **(Top)** Image from Figure 2.5 re-rendered with ~8% of the original molecules to match the molecules/pixel of the 20 s image in Figure 2.6. **(Bottom)** Fibers are still visible despite the reduced molecule density. There is a pronounced difference between the pre-stimulation and 20 s post-stimulation images that is not due to low detected molecule density.

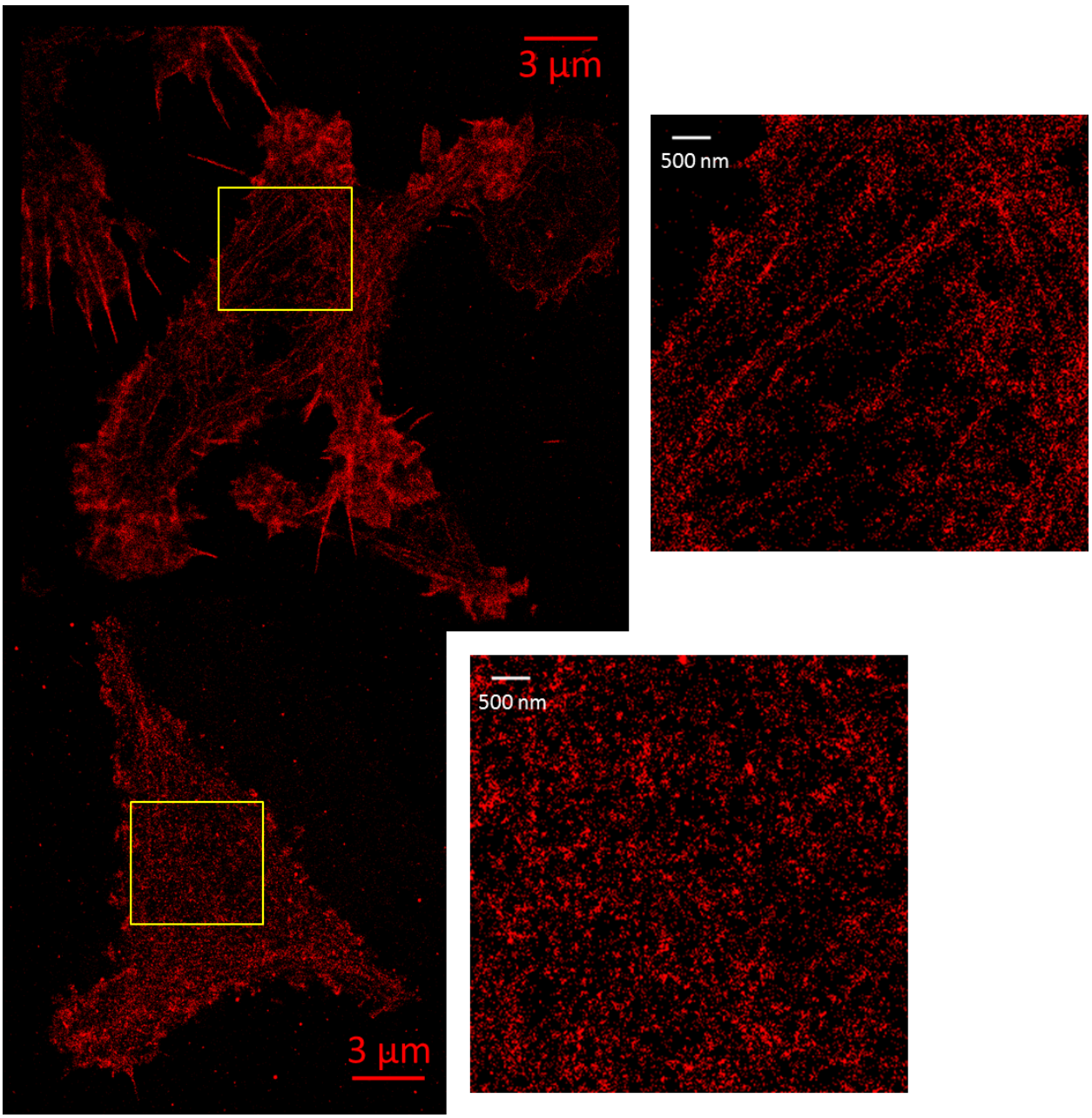

Figure 2.9. Vesicles are found in areas which have less dense F-actin. **(Row 1)** dSTORM image of pre-stimulation cell. **(Row 2)** Images as in row 1, but with widefield vesicle image overlayed. **(Row 3)** Cell 20 s post-stimulation with widefield vesicle image overlayed. **(Row 4)** Cell 120 s post-stimulation with widefield vesicle image overlayed.

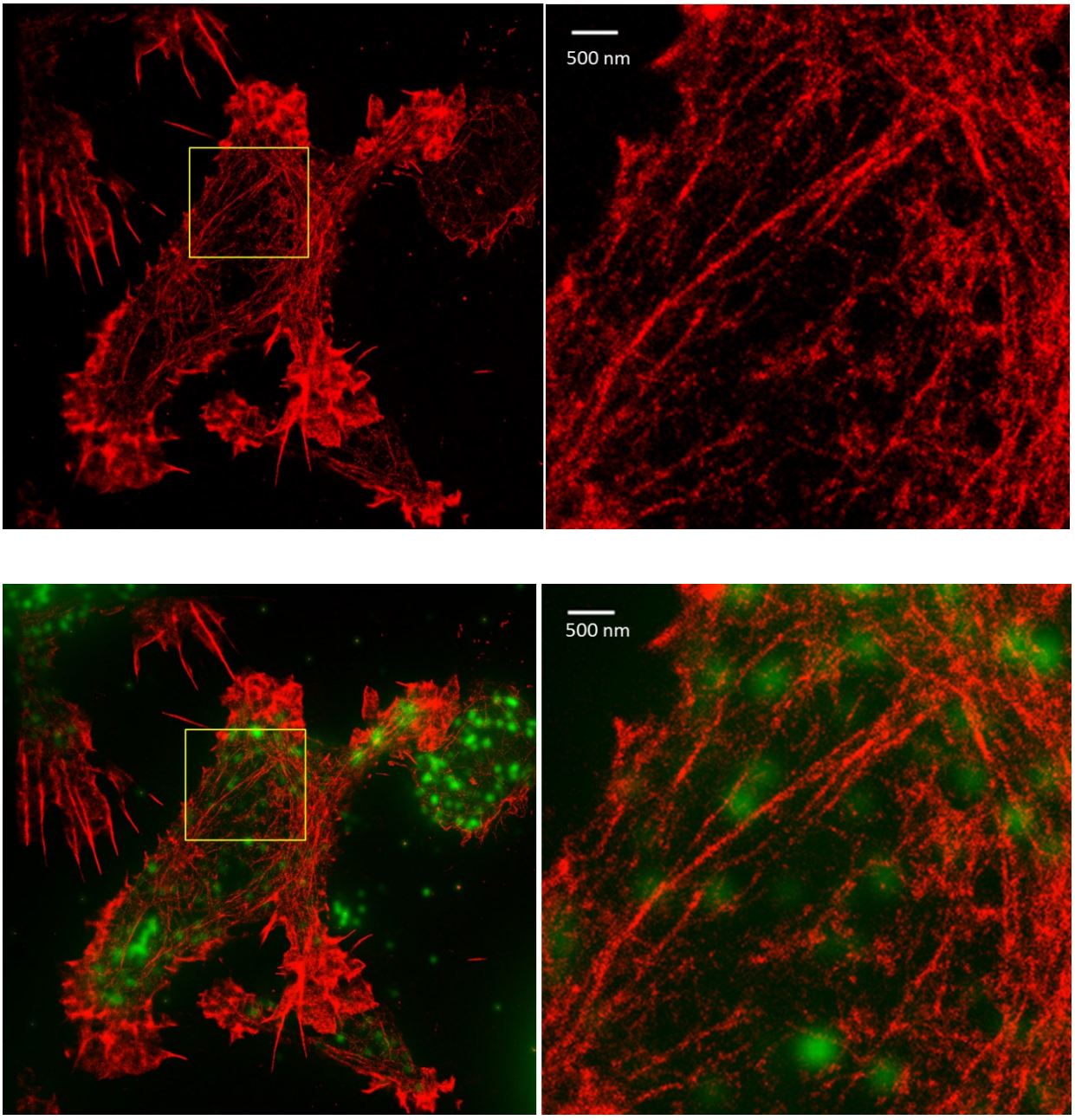

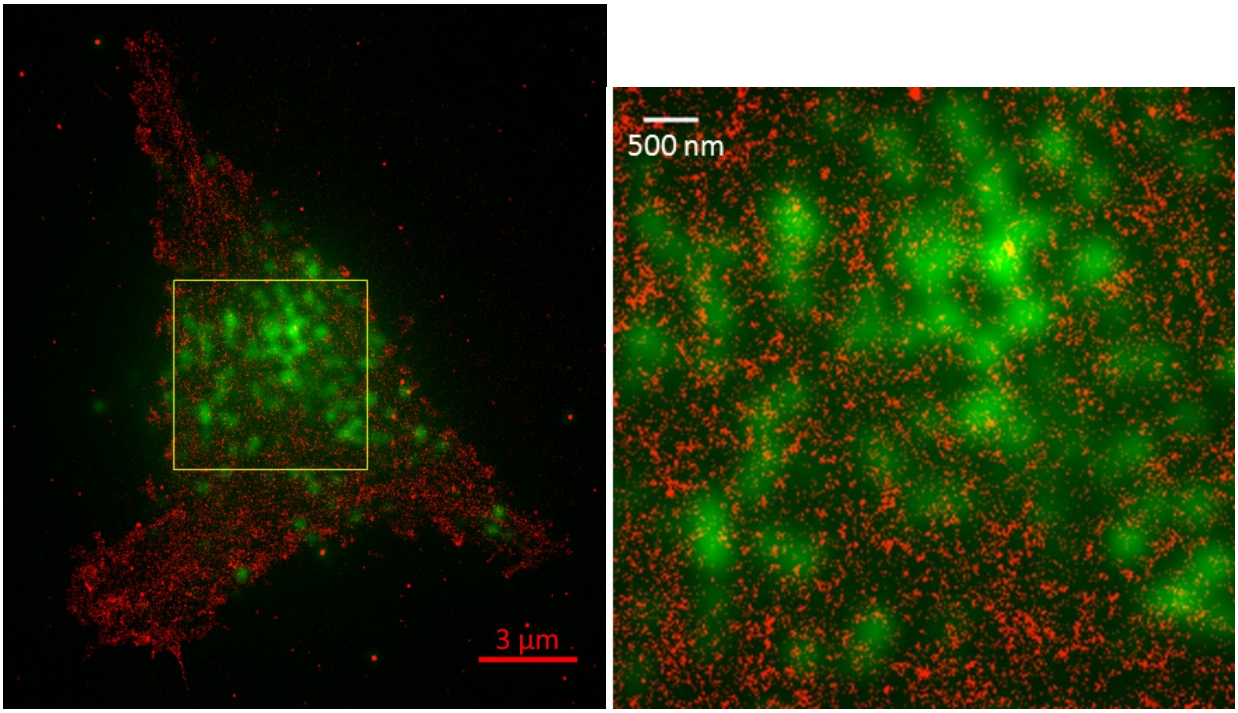
3 µm
500 nm

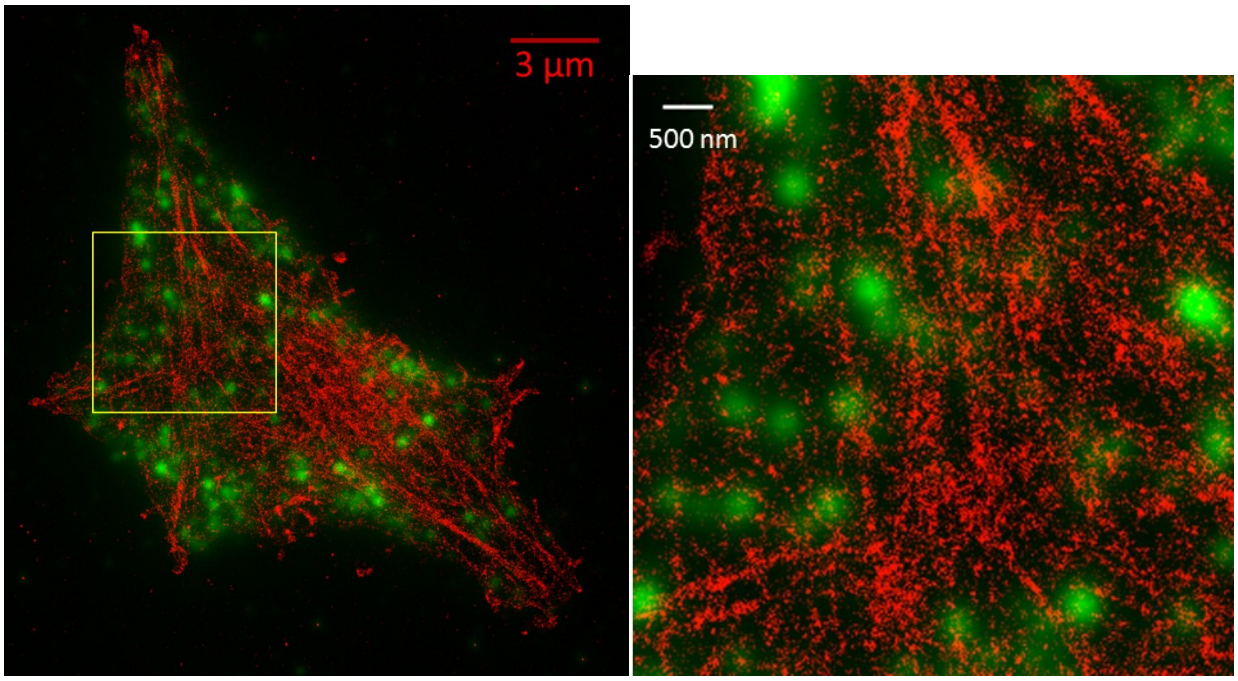
3 µm
500 nm

Figure 2.10. dSTORM images of vesicles (CgB stained with Alexa 647). Conventional widefield TIRF image of vesicles **(Left)** and zoomed in region **(Top right)**. **(Bottom right)** dSTORM image of vesicles in the same region as above.

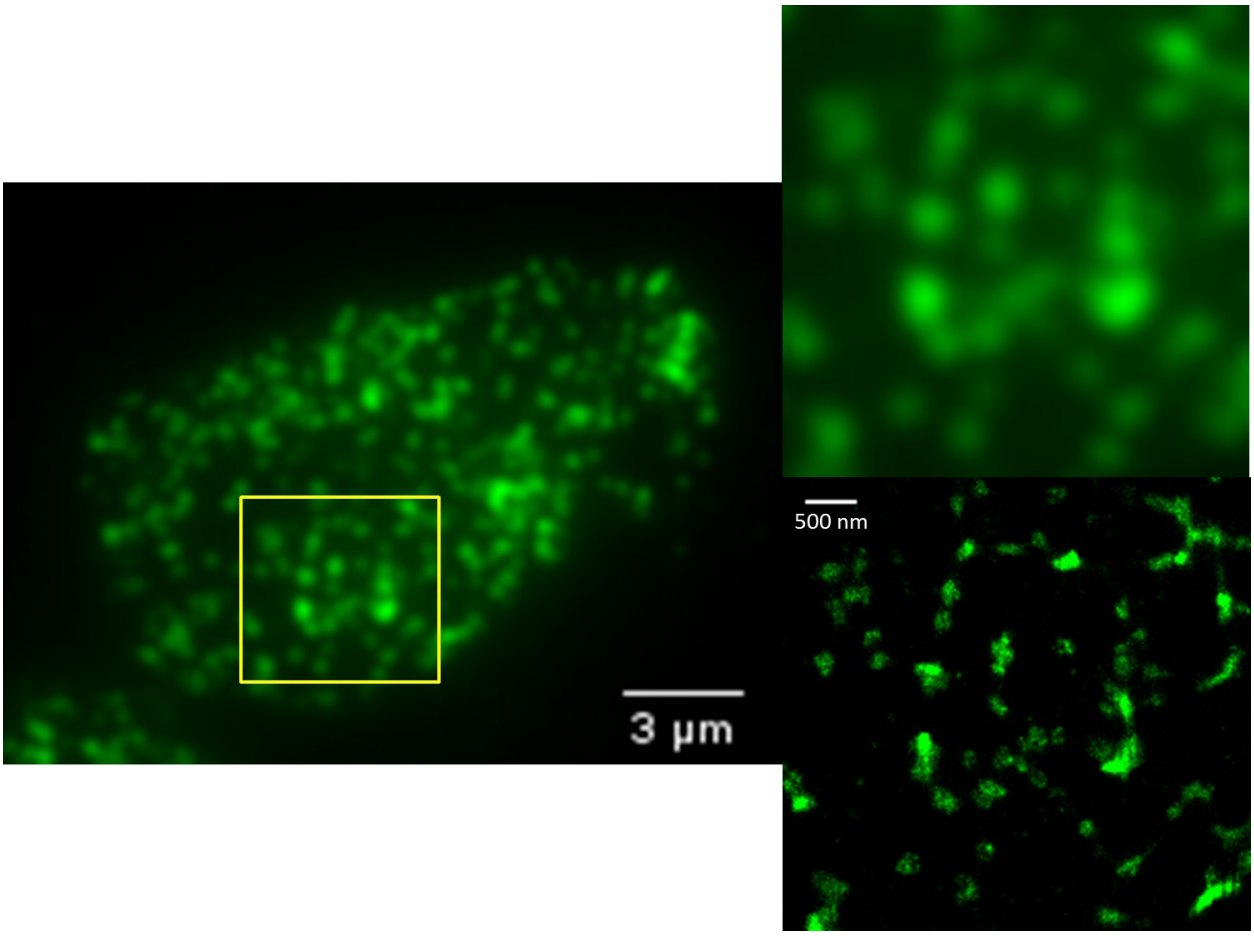

Figure 2.11. Measurement of vesicle diameter. **(Top)** Linescan through a representative vesicle. **(Bottom)** Plot of counts verses distance for the linescan. The profile has a FWHM of ~90 nm.

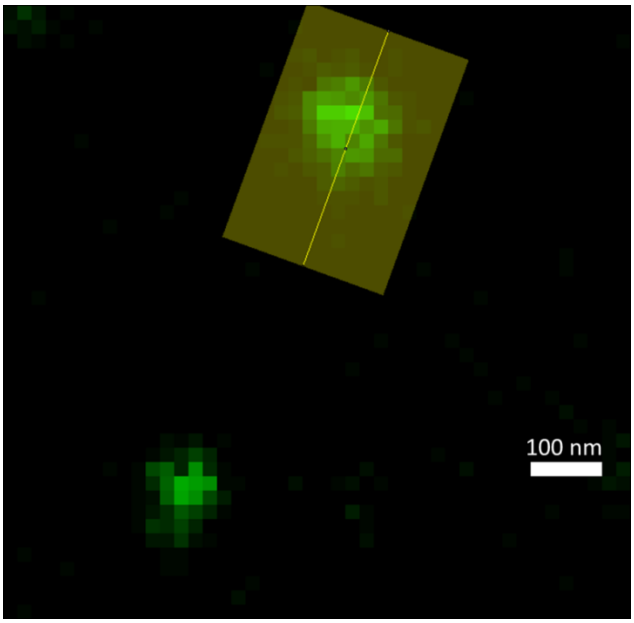

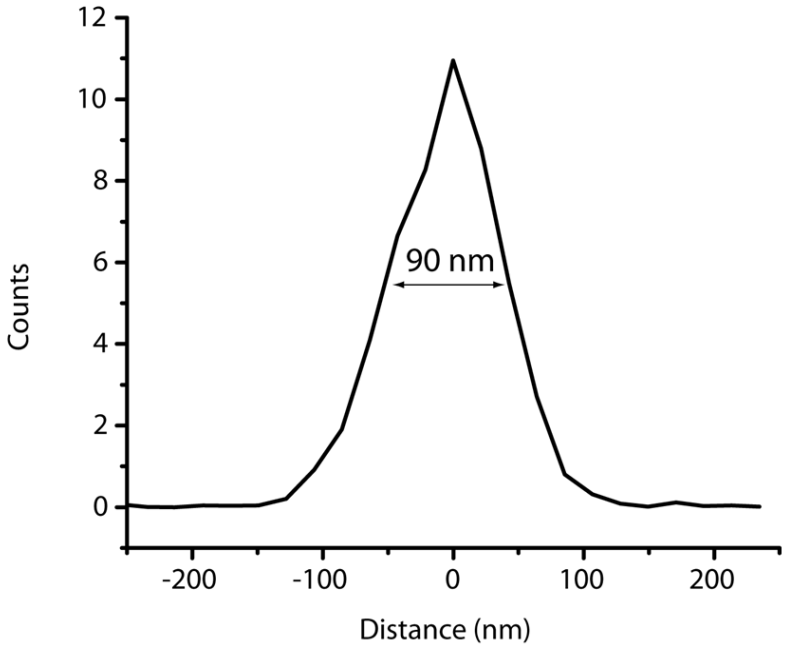

Figure 2.12. Histogram of measured FWHM of 46 vesicles.

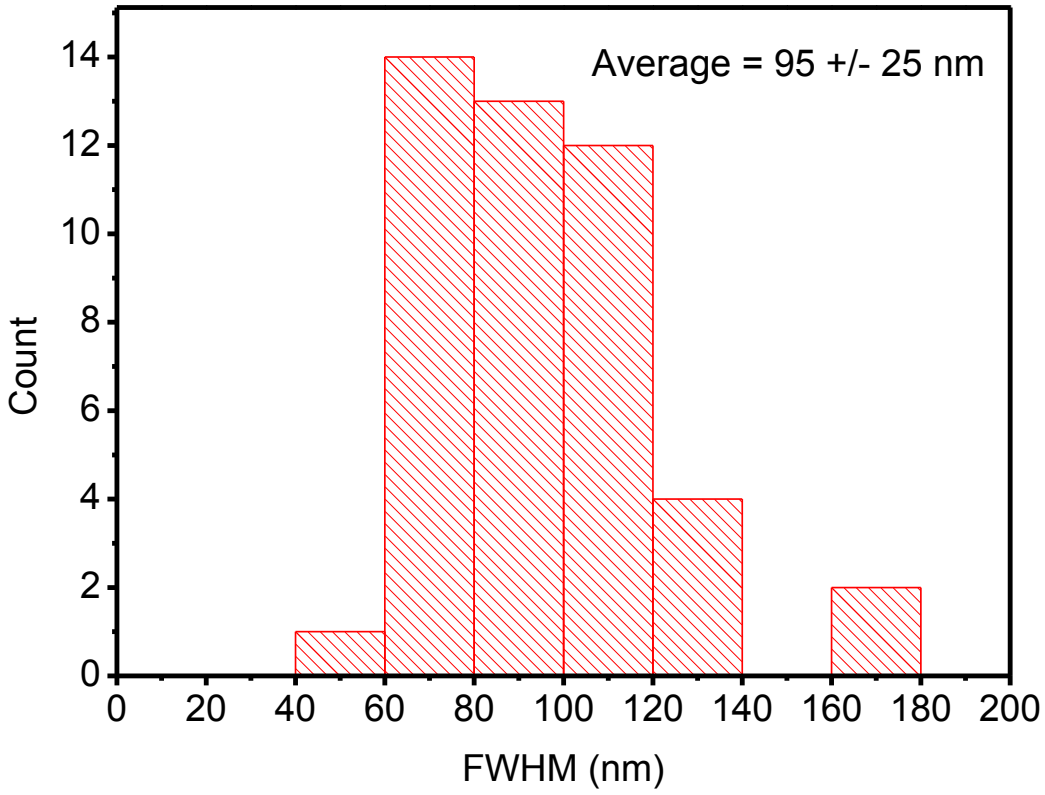

Figure 2.13. Simulation of random positions in a 100 nm diameter sphere. **(Top)** No localization error. **(Bottom)** Positions with localization error (σ = 10 nm) added.

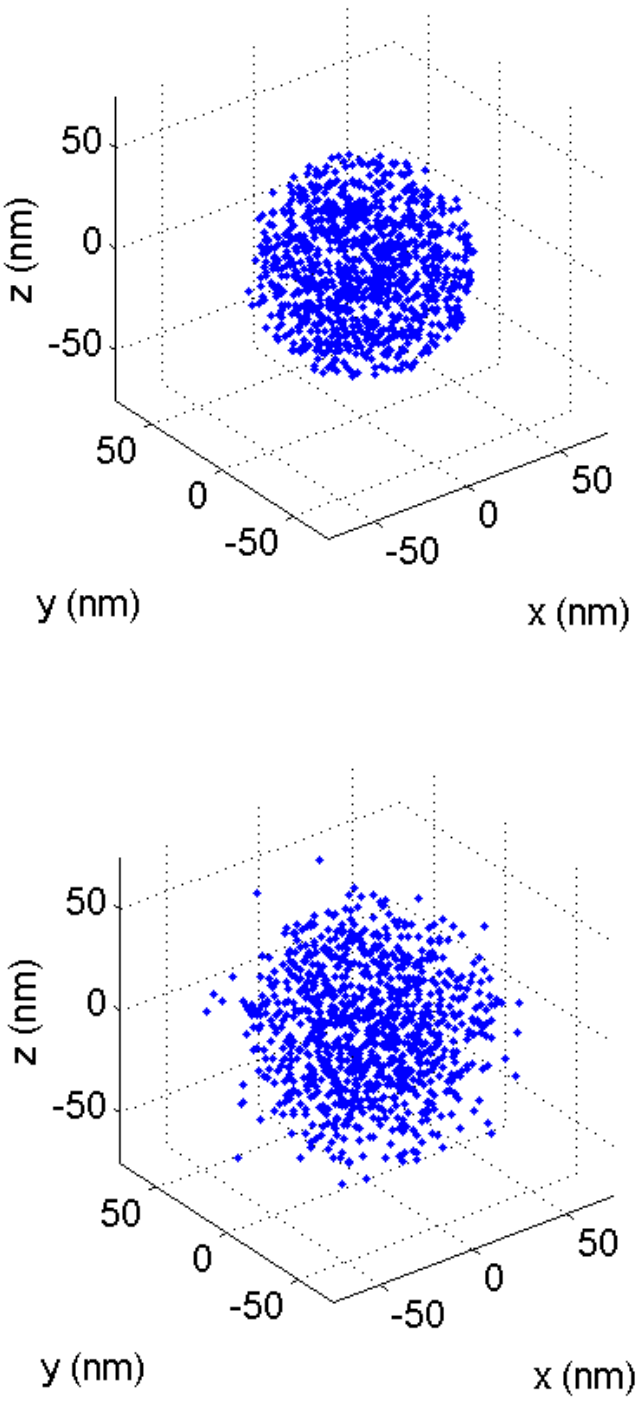

Figure 2.14. Measured FWHM verses actual sphere diameter depends on localization error. **(Top)** Example FWHM measurement for simulation in Figure 2.13 (Bottom). All the positions were projected onto a single dimension (*y*) and binned by 20 nm to match the pixel size in the rendered dSTORM images. FWHM of this sphere was measured to be 69 nm. **(Bottom)** Random error with σ values from 0 to 50 nm was added to the simulated positions. The measured FWHM for 500 simulated spheres was plotted verses the actual sphere diameter for various σ values. This was used as a calibration for using FWHM to measure vesicle diameter. The average measured FWHM of the vesicles was 95 ± 25 nm (dashed black line).

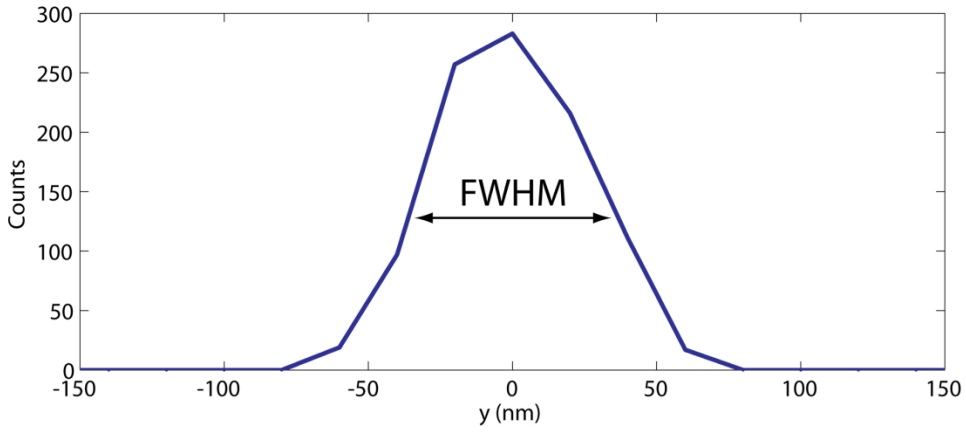

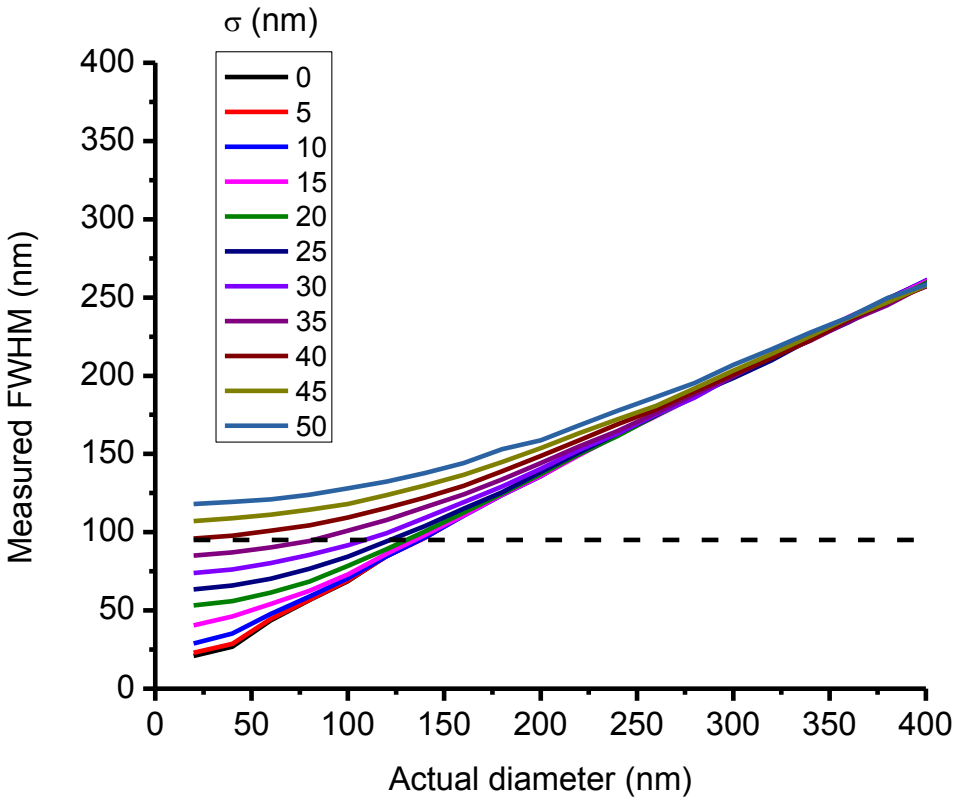
σ (nm)
0
5
10
15
20
25
30
35
40
45
50
Measured FWHM (nm)
Actual diameter (nm)
0
50
100
150
200
250
300
350
400

Figure 2.15. Determination of the localization error. The localization error of the fiducial markers was used as an approximate measure of the overall localization error. The standard deviation of the *x* and *y* positions of the fiducials were measured and had an average of 8.7 ± 1.7 nm.

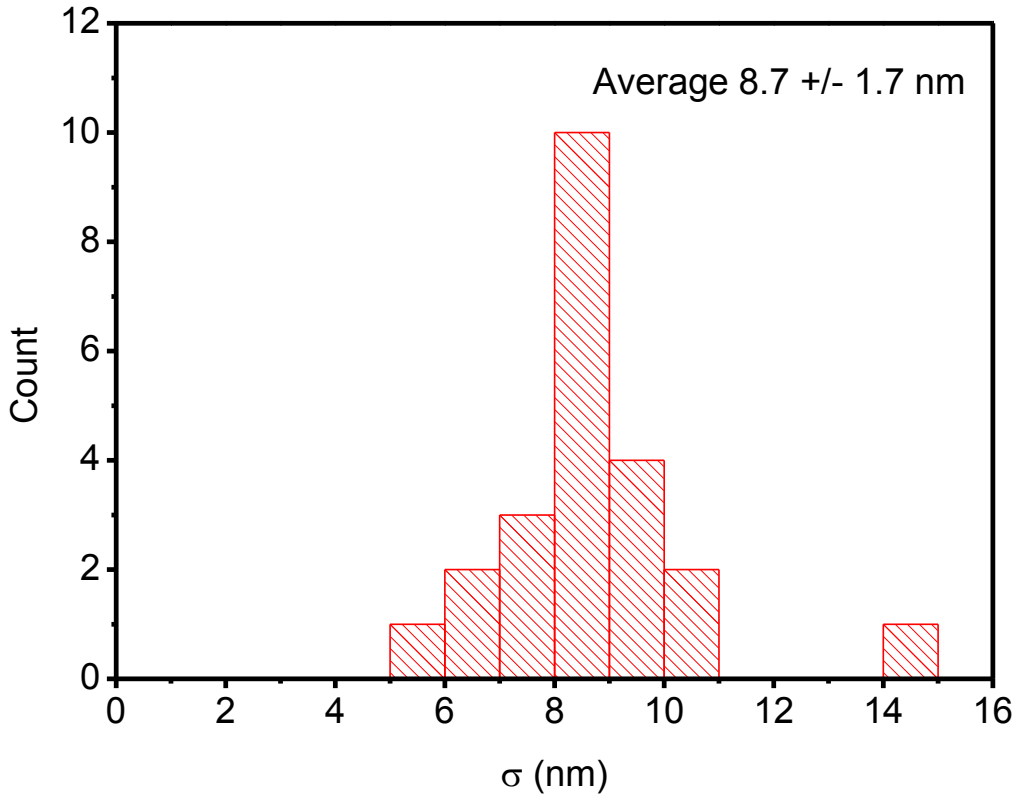

Figure 2.16. Determination of the actual vesicle diameter. Since the localization error was approximated to be 8.7 nm, the simulation shown in Figure 2.13 for σ = 10 nm was used to calculate the actual vesicle diameter. A line was fit to the simulated data and was used to calculate the actual diameter (134 ± 40 nm) given the average FWHM of 95 ± 25 nm.

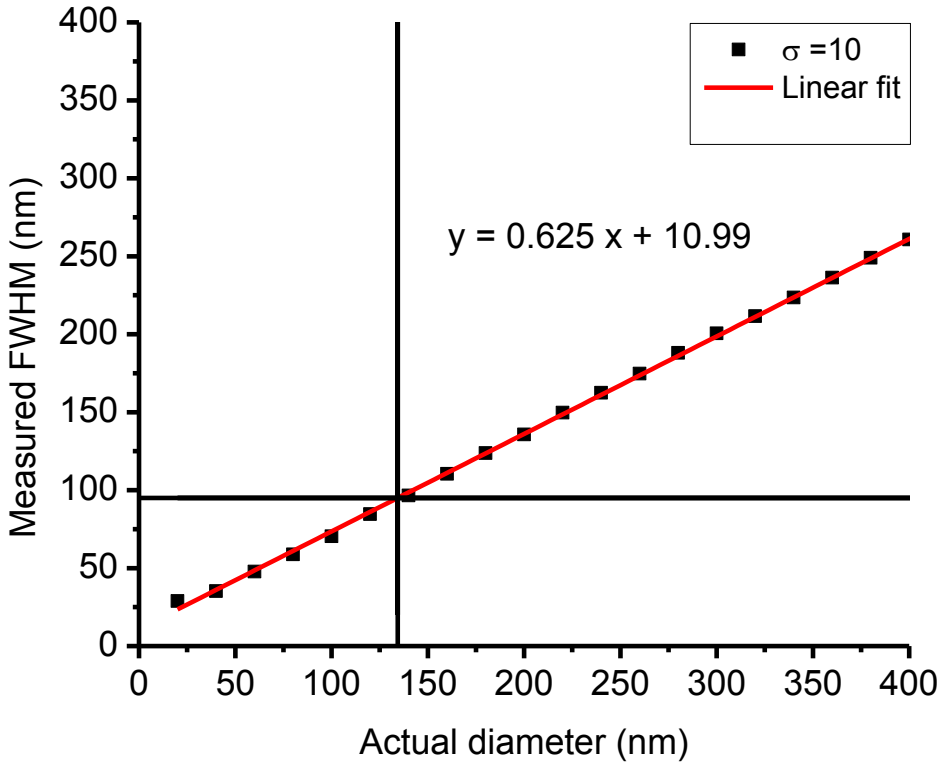

Figure 2.17. Two color dSTORM imaging of Alexa 647 phalloidin and Atto 488 CgB using 2 mM MEA.

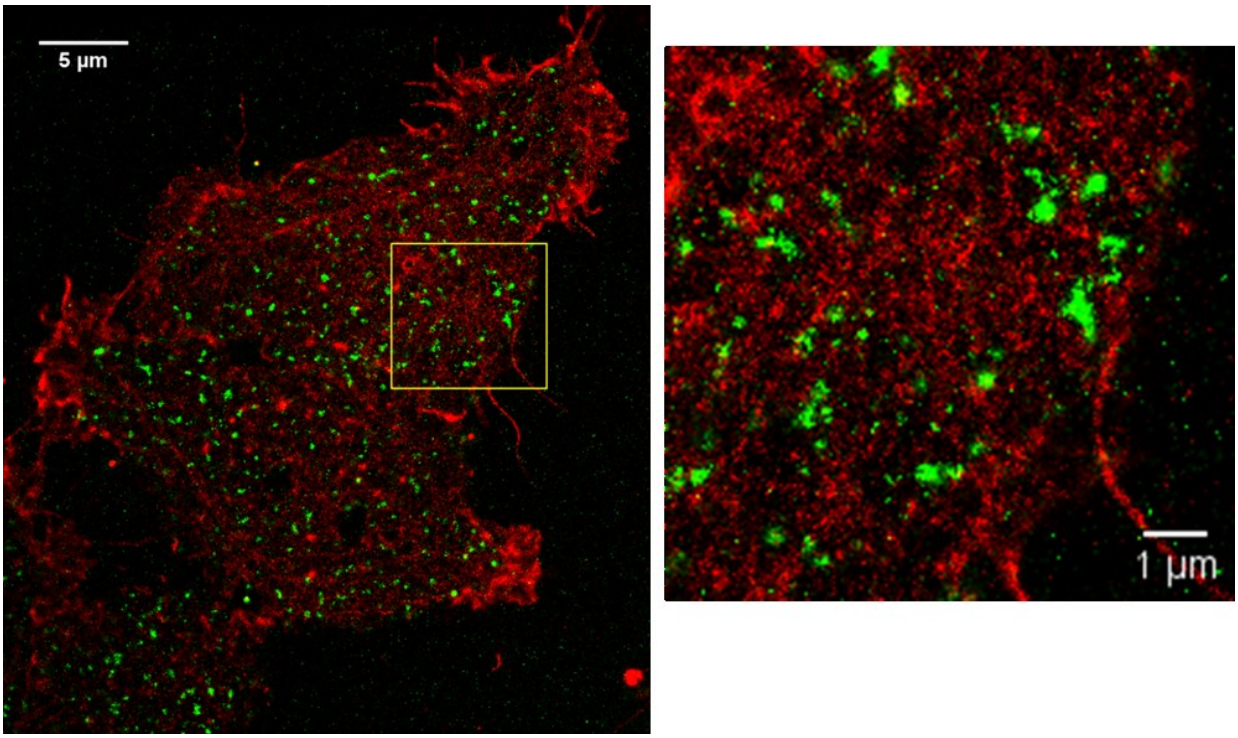

References

1 Orci, L., Gabbay, K. H. & Malaisse, W. J. Pancreatic Beta-Cell Web: Its Possible Role in Insulin Secretion. *Science* **175**, 1128-1130, doi:10.1126/science.175.4026.1128 (1972).

2 Torregrosa-Hetland, C. J. *et al.* The F-actin cortical network is a major factor influencing the organization of the secretory machinery in chromaffin cells. *J Cell Sci* **124**, 727-734 (2011).

3 Giner, D. *et al.* Vesicle movements are governed by the size and dynamics of F-actin cytoskeletal structures in bovine chromaffin cells. *Neuroscience* **146**, 659-669, doi:http://dx.doi.org/10.1016/j.neuroscience.2007.02.039 (2007).

4 Ñeco, P., Giner, D., Del Mar Francés, M., Viniegra, S. & Gutiérrez, L. M. Differential participation of actin- and tubulin-based vesicle transport systems during secretion in bovine chromaffin cells. *European Journal of Neuroscience* **18**, 733-742, doi:10.1046/j.1460-9568.2003.02801.x (2003).

5 Tchakarov, L. E., Zhang, L., Rosé, S. D., Tang, R. & Trifaró, J.-M. Light and Electron Microscopic Study of Changes in the Organization of the Cortical Actin Cytoskeleton During Chromaffin Cell Secretion. *Journal of Histochemistry & Cytochemistry* **46**, 193-203, doi:10.1177/002215549804600208 (1998).

6 Vitale, M. L., Rodríguez Del Castillo, A., Tchakarov, L. & Trifaró, J. M. Cortical filamentous actin disassembly and scinderin redistribution during chromaffin cell stimulation precede exocytosis, a phenomenon not exhibited by gelsolin. *The Journal of Cell Biology* **113**, 1057-1067, doi:10.1083/jcb.113.5.1057 (1991).

7 Giner, D. *et al.* Real-time dynamics of the F-actin cytoskeleton during secretion from chromaffin cells. *J Cell Sci* **118**, 2871-2880 (2005).

8 Kielar-Grevstad, D. M., Dalrymple, R. M., Weisshaar, J. C. & Martin, T. F. J. *Characterization of the Role of F-Actin in Neuroendocrine Secretion: Multiple Signals and Multiple Roles* (University of Wisconsin-Madison, Madison).

9 Xu, K., Babcock, H. P. & Zhuang, X. Dual-objective STORM reveals three-dimensional filament organization in the actin cytoskeleton. *Nature Methods* **9**, 185–188 (2012).

10 Wang, T., Ingram, C. & Weisshaar, J. C. Model Lipid Bilayer with Facile Diffusion of Lipids and Integral Membrane Proteins. *Langmuir* **26**, 11157-11164, doi:10.1021/la101046r (2010).

11 Crocker, J. C. & Grier, D. G. Methods of Digital Video Microscopy for Colloidal Studies. *Journal of Colloid and Interface Science* **179**, 298-310, doi:http://dx.doi.org/10.1006/jcis.1996.0217 (1996).

12 Shannon, C. E. Communication in the Presence of Noise. *Proceedings of the Institute of Radio Engineers* **37**, 10-21 (1949).

13 Lang, T. *et al.* Role of Actin Cortex in the Subplasmalemmal Transport of Secretory Granules in PC-12 Cells. *Biophysical Journal* **78**, 2863-2877, doi:http://dx.doi.org/10.1016/S0006-3495(00)76828-7 (2000).

14 Schubert, D., LaCorbiere, M., Klier, F. G. & Steinbach, J. H. The modulation of neurotransmitter synthesis by steroid hormones and insulin. *Brain Research* **190**, 67-79, doi:http://dx.doi.org/10.1016/0006-8993(80)91160-9 (1980).

15 Tooze, S. A., Flatmark, T., Tooze, J. & Huttner, W. B. Characterization of the immature secretory granule, an intermediate in granule biogenesis. *The Journal of Cell Biology* **115**, 1491-1503, doi:10.1083/jcb.115.6.1491 (1991).

16 *Neuron to Glia Synapses on Axons?*, <http://scienceblogs.com/purepedantry/2007/03/06/neuron-to-glia-synapse-on-axon/> (2007).

17 <http://www.erin.utoronto.ca/~w3bio315/lecture12.htm>

Chapter 3

Short-time DNA loci diffusion in *E. coli*

Introduction

The *E. coli* chromosome is much more organized than previously believed. It was shown to be organized on a large scale by Niki et al. 2000, and Valens *et al.* 2004, who described the existence of chromosomal macrodomains.[1, 2] These domains include the *ori*, *ter*, Right, Left, Non-Structured (NS) Right and NS Left domains (Figure 3.1). These are regions which were shown to be distinct through studies of long distance DNA interactions. Site-specific recombination was used to determine the probability that certain sites collide with one another.[2] The different domains are made up of large regions of the chromosome which were shown to collide only with regions in the same domain. Alternatively, the NS domains were able to interact with their flanking domains and thus were considered to be less constrained.

Developments in fluorescence microscopy and labeling techniques have allowed scientists to label specific locations on the *E. coli* chromosome in order to learn about the organization and dynamics of individual DNA loci. Li *et al.* developed a GFP-ParB/*parS* system in which a *parS* sequence is inserted into the chromosome at the desired location, or locus.[3] Inactive, truncated ParB proteins with a GFP fused to them (GFP-Δ30ParB) bind at this site and spread out to adjoining sequences creating a bright diffraction limited spot (Figure 3.2). These diffraction limited spots can then be located and tracked in the live cell.

The ensemble-averaged mean squared displacement (*MSD*) in two dimensions can be calculated as

$$MSD = \langle(\vec{R}(\tau) - \vec{R}(0))^2\rangle, \quad \textbf{(3.1)}$$

where $\vec{R}(\tau)$ is the focus' position at time lag τ. *MSD*(τ) curves can be used to learn about the underlying dynamics of foci movement. The analytical form of *MSD* is

$$MSD = 4D_{app}\tau^{\alpha} \quad \textbf{(3.2)}$$

where D_{app} is the apparent diffusion coefficient, and α is the subdiffusive scaling exponent. *MSD*(τ) curves which are linear (*MSD*(τ) proportional to τ, α = 1) represent Brownian motion or pure diffusion. If the curve bends upwards the foci are undergoing superdiffusion, or directed motion, and the curve goes as τ^2. If it bends over and *MSD*(τ) goes as τ^{α} with $\alpha < 1$, then the foci motion can be characterized as anomalous subdiffusion. In order to probe the type of anomalous subdiffusion, mathematical models that describe the motion have been employed. One of these models is fractional Langevin motion (FLM). The trajectory of a particle undergoing FLM exhibits long-range temporal correlations that lead to anomalous motion.[4]

The *MSD* curve also provides information about the localization precision of the measurement. The *y*-intercept of the curve (or offset) can be thought of as how much a stationary object appeared to move over multiple measurements. It is roughly equal to $4\sigma^2$ where σ is the localization precision of the measurement.[5]

Many labs have used the GFP-ParB/*parS* labeling system to track DNA loci during the long-time process of DNA replication and segregation (tens of minutes). A few labs have also

studied the shorter-time dynamics of the DNA loci in order to learn about the physical properties of the nucleoid and its environment. In 2008, Espeli *et al*. examined the mobility of loci in different regions of the chromosome.[6] They tracked foci for five minutes with 10 s intervals and then for 1 min with 1 s intervals. They showed that loci in the nonstructured (NS) regions appear less confined than loci in the structured macrodomains (MDs). They estimated that loci in the NS regions move in a "cage" which is 2-4 times larger than that of the structured MDs and travel ~5x further in 5 min than loci in structured MDs.

In a series of two papers, Weber *et al*. also tracked chromosomal loci using the GFP-ParB/*parS* system for 1-100 s at 1 s intervals.[7,8] They characterized the loci motion as subdiffusion with $\alpha = 0.39 \pm 0.04$. This value was found to be constant for six different loci distributed around the chromosome. They proposed that the subdiffusive motion is due to the viscoelasticity of the cytoplasm. They further characterized the motion as fractional Langevin motion (FLM) using a velocity autocorrelation function, $C(\nu)$. This function exhibits a negative peak, suggesting the loci have a tendency to move back towards their previous positions.

In this chapter, we seek to extend these DNA loci diffusion measurements to a time-scale which is 30x faster. We show that in contrast to studies at longer time-scales, a focus in the NS region moves similarly to other tested loci.[6] We also obtain α values in the range of 0.31-0.39 which are similar to those observed previously at longer time-scales.[9] In addition, we show that proper controls must be performed when using the GFP-ParB/*parS* labeling scheme to ensure that the multiple bound copies of GFP do not interfere with the DNA motion. A dependence of $MSD(\tau)$ on trajectory length was observed. $MSD(\tau)$ curves for longer trajectories have smaller initial slopes indicating slower motion. This likely correlates to foci brightness and thus the

number of bound GFP-ParB copies indicating that the physical bulk of the GFP-ParB/*parS* system interferes with loci motion.

Materials and methods

Bacterial strains

The ter, *rrnG* (RLG11967), *rrnD* (RLG10679), and *oriC* strains were constructed by the Gourse lab at UW Madison using the method described by Nielsen *et al.,* and are in a VH1000 background.[7] For example, for *rrnG*, a P1*parS* site and a kanamycin resistance gene were inserted near *rrnG* using the primers 5'-TTCCGCCGCCGGAAATGAATATTCACAGCATCAGGGGATGCGATAAAAAGCCGAAGCCTTAAAC-3' and 5'-CCGGTGCTTGCACCGGCGACATCCCAGGCCAAATCCTTCCCACAGCTTTAGAGCGTTTTGCGAT-3'. The Left-1, NSR-1, Right-2, and NSL-2 strains were obtained from Espeli *et al.*.[6] They have chloramphenicol resistance and are in an MG1655 background. The plasmid pALA2705 P1 ParB-GFP (RLG7493), has ampicillin resistance.[3] It was transformed into the *ter*, *rrnG* (RLG11967), *rrnD* (RLG10679), and *oriC* strains using the TSS protocol.[10] It was expressed in cells without being induced as was done in Nielsen *et al*..[7] The construct used for imaging chromosomally expressed RNAP-β'-mEos2 (HC1) was constructed by Heejun Choi. It contains a translational fusion of mEos2 to the C-terminus of *rpoC*. This strain was constructed as described in Bakshi *et al.*.[11]

Cell growth and sample preparation

Overnight cultures were grown from freezer stock in a hot air shaker at 37° C in either EZ rich, defined medium ("EZRDM", 0.28 Osm, 20% 5x EZ supplement, 10% ACGU, 10% 10x MOPS buffer without potassium or NaCl, 1.32 M K_2HPO_4, 0.2% glucose, 0.076 M NaCl) [12] or chemically defined MOPS-buffered minimal medium ("MBM", 0.28 Osm, 10% MOPS buffer without potassium or NaCl, 1.34 M K_2HPO_4, 0.2% glucose, 0.098 M NaCl) [12,13] as stated. Sub-dilutions were made at a ratio of at least 1:100 and were allowed to grow to mid log phase until an optical density (OD) between 0.3 and 0.6 was reached. 150 µL of cells were plated in stick-on gasket chambers (Invitrogen) on poly-L-lysine coated coverslips which had been pretreated by sonication in acetone then 1M KOH (Figure 3.3). After sitting for ~2 min, the chambers were rinsed with fresh warm medium to remove any unadhered cells. The chambers were sealed to avoid evaporation of the growth medium. These chambers allowed for a greater number of useable cells to be imaged per field of view (~35) in comparison to a slide/coverslip preparation which often contains a lot of unadhered cells. The exception to this is that the foci tracking data performed at 10 Hz was obtained in the slide/coverslip configuration with 7.2 uL of medium plus cells placed on the slide. A poly-L-lysine coverslip, cleaned as above, was placed on top and was sealed with nail polish.

Imaging

Fluorescently labeled (GFP-ParB/*parS*) chromosomal loci were excited with a 488 nm Ar^+ laser (Melles Griot, Carlsbad, CA). The 488 nm power density at the sample was adjusted to provide sufficient signal to noise while maximizing the number of frames the molecule could be tracked for. The average power density was in the range of ~0.1- 0.5 kW/cm^2.

Images were acquired using a Nikon Eclipse Ti inverted microscope and a 1.45 NA oil immersion objective (CFI Plan Apo Lambda DM 100X Oil). After focusing at the midplane of the cells using phase contrast imaging, the focus at the sample was maintained with the Nikon perfect focus system. Emission was collected through a 525/50 emission filter (ET 525/50M Chroma). An additional 1.5x tube lens was used to increase the magnification. Overall there was 150x magnification with each pixel corresponding to 105×105 nm^2 at the sample. Images were recorded on a back-illuminated EMCCD camera with 16 μm x 16 μm pixels (iXon DV-887, Andor Technology, Connecticut). The camera was driven with Andor Solis software. Imaging was performed at 37° C or room temperature (25° C) by using a home-built chamber around the microscope stage which utilizes an Air-Therm-ATX heating unit (Figure 3.4).

For the short-time diffusion movies, foci were tracked at 33 Hz in frame transfer mode or at 10 Hz with 20 ms exposure time (as specified). These times were chosen to probe different diffusion time-scales and still freeze foci motion while minimizing bleaching.

Shutters (Uniblitz LS2, Vincent Associates, and Lambda SC *Smart*Shutter, Sutter Instrument Company) and a Four Channel Digital Delay/Pulse Generator (DG535, Stanford Research Systems Inc) were used to control the timing of the laser pulses and to switch between the phase contrast and fluorescence images.

Data analysis

Peak finding

Data analysis was accomplished using a custom peak finding and tracking program as described earlier.[14] Briefly, the raw data was smoothed using a bandpass filter in order to obtain

a zero-based image. A single pixel intensity threshold was used to determine which bright spots are foci. The foci's sub-pixel locations were found by fitting the diffraction limited spots with a Gaussian function or determining their centroid. The Gaussian function was sometimes used over finding the centroid because of its improved performance in cases where the signal to noise level is low. For example, cells grown in EZRDM have dimmer foci and higher in cell background intensity. Alternatively, when there is good signal to noise these methods have been shown to perform comparably, so the centroid was found to reduce computational time.

Tracking and MSD analysis

For tracking, molecules in successive frames are linked together using a modified MATLAB version of the tracking program written by Crocker and Grier.[15] Mean-squared displacement analysis was carried out as described earlier.[16] The population-averaged mean-square displacement (*MSD*) vs lag time (τ) is calculated by:

$$MSD_r(\tau) = \frac{1}{NM}\sum_i \sum_m \left[r_i(m\Delta t + \tau) - r_i(m\Delta t)\right]^2 \qquad \textbf{(3.3)}$$

where $r_i(t)$ is the particle position in trajectory i at time t, τ is the lag time, N is the total number of trajectories, and Δt is the time between frames. M is the cutoff length for the trajectories. Any trajectory shorter than this was rejected and any trajectory longer than this was truncated to M steps. The index m runs from 0 to the largest possible value M given the lag time and the trajectory length. Individual foci's estimated diffusion constants were calculated by:

$$D_i(\tau) = \frac{1}{4\tau M}\sum_m [r_i(m\Delta t + \tau) - r_i(m\Delta t)]^2 \,. \qquad \textbf{(3.4)}$$

The velocity autocorrelation function (C_v) was calculated by

$$\boldsymbol{C_v^{(\delta)}(\tau) = \langle \vec{v}(t+\tau) \cdot \vec{v}(t) \rangle}, \quad \textbf{(3.5)}$$

where

$$\boldsymbol{\vec{v}(t) = \frac{1}{\delta}\left[\vec{R}(t+\delta) - \vec{R}(t)\right]} \quad \textbf{(3.6)}$$

is the velocity of the molecule, $\vec{R}(t)$ is the position of the focus, τ is the time lag, and δ is the time step. The curves were then normalized by

$$\boldsymbol{C_v^{(\delta)}(\tau = 0)}. \quad \textbf{(3.7)}$$

See Figure 3.5 for a pictorial explanation of this calculation.

Results and discussion

Short-time diffusion in MBM

DNA loci in cells grown in MBM were tracked at 33 Hz in frame transfer mode (continuous frames). This is thirty times faster than previously reported DNA loci tracking at the time of these experiments.[6,9,17] At this fast time-scale, foci mostly jiggle in place, with trajectories not escaping very far on a several second time scale (Figure 3.6). Trajectories were truncated to 100 frames and *MSD*(τ) was plotted. Mean-squared displacement curves show that at this time-scale, foci located in different macrodomains diffuse with very similar apparent

diffusion constants. The exception is that Left-1 appears to move slightly faster (Figure 3.7). This includes the NSL-2 focus which is located in the NS region.

33 Hz vs 10 Hz tracking

Three of the loci (NSL-2, *rrnG*, and Left-1) were also tracked at 10 Hz with 20 ms exposure times. When this data is truncated to 30 frames (to match the timescale of the 33 Hz data) and plotted on the same axes as the 33 Hz data, the two curves do not match (Figure 3.8). The $MSD(\tau)$ curves for the 10 Hz data have a larger initial slope.

There are several possible reasons for this. These experimental data sets were taken months apart and under slightly different conditions. The 33 Hz data was taken on cells plated in the stick-on gasket chambers while the 10 Hz data was taken on cells plated in a slide/coverslip sandwich. There was less medium (7.2 μL) available to the cells in the case of the slide/coverslip sandwich. The stick-on chamber on the other hand had ~150 μL of medium available to the cells. It was also fresh medium, not the medium the cells were growing in, due to the rinsing step of the sample prep. Perhaps this made a difference in the cell dynamics due to different nutrient or oxygen levels present.

It is also possible that since these experiments were performed on different days the amount of instrument drift could have been different. We have shown that on a 1 s timescale at room temperature the amount of instrument drift is significantly less than the measured diffusion of the foci (Figure 3.9a). This was done for another study in which we have compared the diffusion of DNA loci to slow moving RNAP molecules. Cells expressing RNAP-β'-mEos2 were fixed and single RNAP-β'-mEos2 molecules were photoactivated and then tracked. These

molecules are similar to or less bright than the foci tracked here and are a reasonable control for instrument drift.

It is possible, however, that at 37 °C and longer times than 1 s the instrument drift may have had a greater effect. This control experiment should ideally be repeated for the same time-scales studied here. One problem with this approach is that the instrument drift is widely variable from day to day due to environmental conditions. Ideally, the drift should be monitored at the same time that the experimental data is collected. One common approach to doing this is to add fiducial markers, such as fluorescent microspheres to the sample. This presents a challenge when studying *E. coli*: experiments are performed with the focal plane in the center of the cells (either 450 nm or 315 nm from the coverslip surface for cells grown in EZRDM or MBM respectively) at which point the beads are out of focus due to the depth of field of the 1.45 NA objective. One possible alternative is to add fixed cells expressing the fluorescent construct of interest to the sample containing the live cells and use them as the fiducials. One would then have to sort the collected data in a manner which separates the fixed cells from living cells.

Trajectory cutoff length affects MSD(τ)

In calculating $MSD(\tau)$ all the trajectories are cut to a certain length and the remaining steps are thrown out. The cutoff length was changed and there was a drastic effect on $MSD(\tau)$. This is shown for a representative data set (NSL-2 foci in cells grown in MBM and tracked at 33 Hz) in Figure 3.10a. Both the slope and offset of the curves increase with decreasing cutoff length. This suggests that the longer trajectories have a decreased *MSD*. It is possible that the longer trajectories consist of foci which are brighter, allowing them to be tracked for longer.

These brighter foci likely contain more GFP molecules and thus are larger objects. This suggests that labeling DNA loci with a GFP-ParB/*parS* system can in fact alter the DNA motion if a large number of GFP molecules bind to the *parS* site. In order to examine this further, the brightness (average over the whole trajectory of the integrated intensity in a 3 by 3 pixel box around the focus) of the foci was plotted vs trajectory length (Figure 3.10b). The plot shows that many trajectories are both short and have low brightness. As the trajectory cutoff length is decreased, more and more of these molecules are included in the *MSD* calculation. This causes the offset to increase because the localization accuracy of these less bright molecules is lower (higher σ). It causes the *MSD* curves to have a greater slope, perhaps because these less bright foci are decorated with fewer GFP copies.

In order to examine this, the trajectories were grouped by brightness and $MSD(\tau)$ was plotted for each group (Figure 3.11). It was expected that if the brighter foci were larger objects they would move more slowly. Surprisingly, all the brightness groups when cut to 15 frames behave very similarly to the curve which includes all the data, with the exception of the curve for foci with brightness of <500 counts. This curve seems to indicate that these foci move more slowly, but it has considerably fewer trajectories (n=36) included in it and could be affected more by error. The curves of all the data cut to 15 and 100 frames are shown for comparison.

When these same trajectories are grouped by length and then cut off to 15 steps, the longer trajectories (>100 steps) are slower while the shorter trajectories (15-30 steps, and 30-100 steps) move faster, and are very similar to the curve which includes all the data (Figure 3.12). The offsets also decrease with increasing trajectory length suggesting the localization precision is better for the longer trajectories. It is apparent that grouping the data in this manner separates the

slower trajectories from the rest (trajectories with > 100 steps). It is hypothesized that this group of trajectories likely contain foci which are made up of a greater number of GFP-ParB molecules. This causes them to move more slowly. A possible reason why grouping the trajectories by brightness did not detect this is discussed below.

One complication of this analysis is that the beam profile over the field of view was not flat (Figure 3.13). This causes foci at the edge of the field of view to appear dimmer even if they have a large number of GFP copies bound. For this reason the analysis of grouping foci by their brightness is slightly flawed. The measured brightness is not an accurate measurement of the number of GFP molecules bound. This was slightly less of a concern for the 10 Hz data which was taken using a larger beam (Figure 3.13). In order to truly assess whether the number of bound GFP molecules affects the motion, the beam profile should be flat across the field of view so that the foci in different cells are illuminated evenly and bleach at an even rate.

Short-time diffusion in EZRDM

DNA motion as a benchmark for determining the transcribing fraction of RNAP

The motion of Left-1, NSL-2, and *rrnG* were tracked in cells grown in EZRDM at 10 Hz with 20 ms exposure times. The $MSD(\tau)$ curves can be found in Figure 3.14. This data was taken in order to compare it with the motion of RNA polymerase (RNAP) molecules. This project is in collaboration with Somenath Bakshi and Wenting Li who designed and performed the RNAP tracking experiments.

RNAP binds to DNA during transcription events. The DNA motion was used as a benchmark to decide which RNAP molecules were bound (transcribing) and which were in an

unbound state. The *MSD*(τ) curves for trajectories cut to 11 steps are plotted along with that of the "slow" RNAP molecules (D_i < 0. 015μm^2/s) (Figure 3.9). A plot of fixed RNAP molecules is also included as a measurement of the contribution of instrument drift. The slope of the various DNA loci and the slow RNAP molecules' *MSD*(τ) curves are very similar. In addition, the distribution of individual trajectory's Ds are plotted for 3 step RNAP and *rrnG* trajectories. These distributions match very well indicating that the "slow" RNAP molecules are likely bound to DNA. These benchmark DNA motion measurements were critical in determining of the fraction of RNAP which is engaged in transcription. A detailed study of the partitioning of RNAP molecules into different states can be found in Bakshi *et al*..[11]

DNA loci exhibit anomalous diffusion

At these short timescales, we are seeking to measure the inherent jiggling of the DNA polymer itself. The *MSD*(τ) exhibits negative curvature, which indicates that DNA foci undergo anomalous diffusion. This is not explained by confinement by the cell geometry since the trajectories are very compact and do not travel that far on these time-scales. In order to determine the subdiffusive scaling exponent, α values were calculated as the slope of a linear fit to the log(*MSD*) vs log(τ) plots for cells grown in MBM and EZRDM (Figure 3.15, 3.16). The last few data points were excluded from the fitting due to increased noise at large values of τ. The α values are similar for the two growth conditions and range from 0.31-0.39 (Table 1 and 2). These values are consistent with those reported previously for longer time-scales of 1-100 s.[9] Weber *et al*. suggested that these α values are characteristic of a viscoelastic cytoplasm.[9] There is likely also a contribution from the elastic nature of the DNA polymer itself. Our study extends

the time-scale across which α is constant. This should be the case if the viscoelasticity of the DNA polymer and cytoplasm are the cause of the anomalous diffusion.

In order to investigate the type of anomalous diffusion DNA loci undergo at this time-scale, we calculated the velocity autocorrelation function, $C(\nu)$. Weber *et al.* reported that this function can be used to determine if molecules are undergoing fractional Langevin motion (FLM), which states that the steps of the trajectory are not independent.[4,9] If so, they will exhibit long-range temporal correlations in their trajectories and there will be a negative peak in C_v. However, it is also possible that this negative peak appears due to localization error, in which case the negative peaks for each successive time step, δ, will decay to zero.[4]

Weber *et al.* reported that DNA loci undergo FLM at time-scales of 1-100 seconds.[9] We sought to explore if this trend continues down to a time-scale which is a factor of 30 faster. Velocity autocorrelations (C_v) at time steps (δ) from 0.1 s to 5 s ($(\frac{1}{frame\ rate} * \#\ frames \div 2)$ in integer multiples of the frame interval) were calculated for the data taken at 10 Hz for cells grown in MBM (Figure 3.17). C_v at time steps of 0.03 s to 7.5 s were calculated for Left-1 data taken in MBM at 33 Hz (Figure 3.18). The negative peaks of each of these curves have a relatively constant value, but do decay slightly as δ increases. This is more obvious in the 33 Hz Left-1 plot in which the negative peak decays significantly. This may indicate that DNA loci are undergoing FLM, but it is possible that there is a component of localization error present which causes the negative value of the peaks to decay. This is interesting since the 33 Hz data actually had a slightly smaller localization error ($\sigma \approx 16$ nm) than the 10 Hz data ($\sigma \approx 19$ nm) according to the estimated intercept of the $MSD(\tau)$ curves. The difference in σ is likely due to the fact that

more of the downward curvature towards the intercept is captured in the 33 Hz, data resulting in a lower extrapolated intercept. These σ values are actually upper-bounds of the localization error since the initial slopes of the $MSD(\tau)$ curves continue to increase with decreasing time-scales as more of the curvature is captured. Due to these facts, it seems that the data shown here differ slightly from those of Weber *et al*. since the value of the negative peak decays systematically, but it does not seem to be due to measurement error. Perhaps the anomalous diffusion at these short time-scales is not purely explained by the FLM model.

Comparison with a recent study

At the time of this writing, work by Javer *et al*. was published in which they track DNA loci motion at similar time-scales of 0.1-10 s.[18] This study found that there is a dependence of loci motion on chromosomal position. *MSD* reported at a 10 s lag time was seen to vary approximately linearly from *oriC* to *ter*, with *ter* having the smallest displacements. A similar trend was not observed here, in fact the Left-1 locus (which is the closest to *ter* tracked here) was seen have slightly larger displacements while the other loci moved similarly to each other.

In an effort to determine if the focus' intensity affects its motion, Javer *et al*. plot the *MSD* (10 s) vs focus intensity and see that it in fact decreases with increasing intensity by a factor of ~5.[18] However, they suggest that the variation of the motion between the loci persists for most of the intensity ranges; however, it does decrease significantly for the faintest loci. In light of the findings made here, it could be those faintest loci which are least affected by the large size of the GFP-ParB object and reflect the true motion of the loci. In that case there was little difference in the motion of their loci, as observed here. It is also difficult to assess whether

or not the contribution of the *MSD* offset was addressed in their work. It was observed here by eye that the brightness of the foci increased from *oriC* to *ter*, which is consistent with there being fewer loci copies in the cell and thus each copy has more GFP-ParB bound. If the brighter foci have smaller offsets, then the offset would decrease from *oriC* to *ter* causing their reported *MSD* (10 s) to decrease as well, as they observed. The differing offsets obviously complicate the analysis of comparing the motion of the loci and must be considered.

Conclusions

It is clear that the fact that the number of GFP-ParB molecules bound alters the motion of the DNA has huge implications in the field of DNA loci tracking. Careful control experiments need to be performed to ensure that the number of GFP-ParB copies bound to the *parS* site do not affect the motion under study. It has been previously shown that overexpression of the GFP-ParB protein using induction with 100 μM IPTG causes fewer foci to be observed than should have been present as determined by flow cytometry.[3] The high levels of expression were either causing the foci to stick together or some not to be labeled at all. It is now apparent that even without the use of additional induction the GFP-ParB molecules can perturb the system.

Future experiments

Alternate loci labeling scheme

Further studies are needed to confirm whether or not there is an artifact due to the GFP-ParB/*parS* labeling scheme. One way to accomplish this would be to use a fluorescent-repressor-operator system (FROS). Tandem copies of *tet* operator (*tet*O) or lac operator (*lacO*) arrays are inserted into specific regions of the chromosome. A fluorescent protein is then tagged to the Tet repressor (TetR) or Lac repressor (LacI) which is expressed in the cell and binds at the *tetO* or *lacO* sites respectively (Figure 3.19). This system allows for control of the number of fluorescent molecules that bind by inserting a specific number of binding sites into the chromosome. Historically, ~240 copies of the operators were used. With advances in fluorescence detection fewer copies can now be used.[19] This has been demonstrated by Wang *et al.* 2011, and Hensel *et al.* who used an array of only six and three tandem binding sites respectively.[20,21]

This labeling system could help control for artifacts due to the large size of the GFP-ParB/*parS* system, but it would also limit the amount of time one can track the foci before they bleach. In addition, the expression of the fluorescent construct must be regulated in order to allow for clear detection of the site of interest over the background of unbound molecules. Another disadvantage is that due to the limited expression level, not all operator sites are bound by the fluorescent construct. Despite these disadvantages, FROS should allow the motion of DNA loci to be studied with less interference from the labeling method than the GFP-ParB/*parS* system.

Final thoughts

In the future, the results of this work should be verified using an alternative labeling scheme such as FROS. Efforts should be made to make the excitation beam as flat as possible over the field of view. The distribution of GFP-ParB/*parS* foci brightness and their respective motion should be further quantified in order to assess the true effect of the number of GFP-ParB molecules making up each focus. The absolute number of GFP molecules can be estimated by dividing the intensity of the foci by that of a single GFP molecule under the same illumination conditions. This would provide a true estimate of the size of the foci.

Tables

Table 1. α values for cells grown in MBM. Foci tracked at 33 Hz.

	α	Standard Error
oriC	0.33	0.0023
rnD	0.36	0.0012
NSL-2	0.38	0.0013
rrnG	0.32	0.0017
Left-1	0.39	0.0017
rrnC	0.34	8.7E-04

Table 2. α values for cells grown in EZRDM. Foci tracked at 10 Hz with 20 ms exposure time.

	α	Standard Error
NSL-2	0.31	0.0026
rrnG	0.32	0.0028
Left-1	0.34	0.0025

Figures

Figure 3.1. Locations of the macrodomains and *parS* sites on the chromosome map. Figure reproduced with modifications from Valens *et al*., 2004.[2]

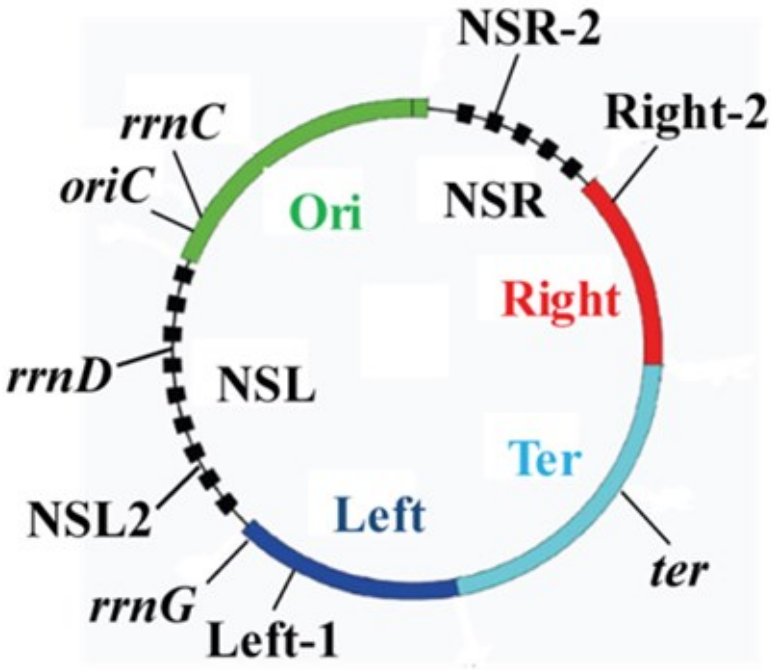

Figure 3.2. Phase contrast image **(Right)**, example of DNA loci (*oriC*) labeled with the GFP-ParB/*parS* labeling scheme **(Left)**.

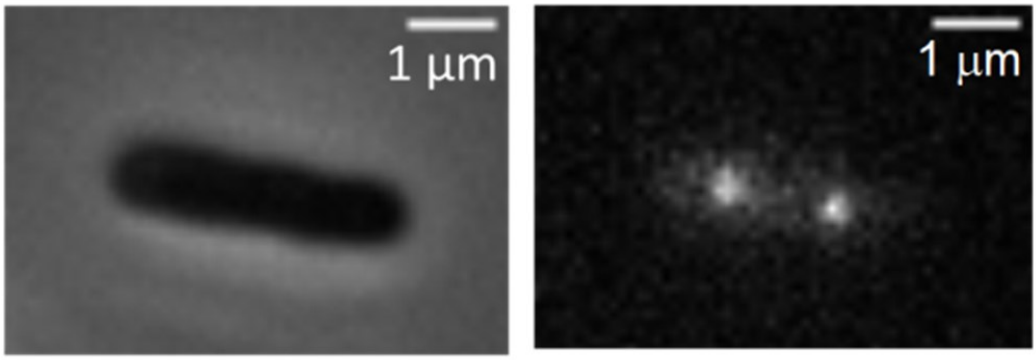

Figure 3.3. Stick-on gasket chambers (Invitrogen) on poly-L-lysine coated coverslip.

Figure 3.4. Home built microscope enclosure used to keep the sample at a specified temperature. Warm air is circulated through tubing by an Air-Therm-ATX heating unit located on a shelf above the microscope.

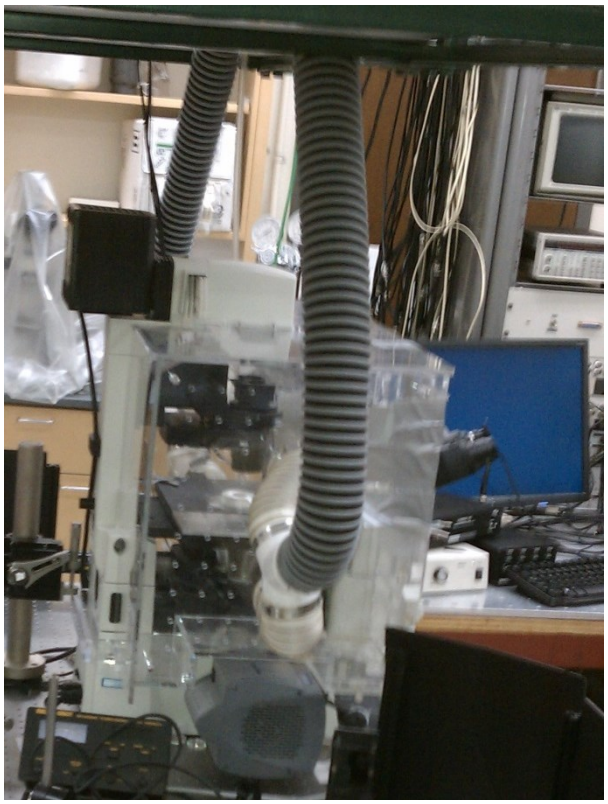

Figure 3.5. Example of how $\vec{v}(t)$ is determined for C_v calculation (equations 3.5-3.7). Given a trajectory with positions from $\vec{R}(t_1)$ to $\vec{R}(t_7)$, $\vec{v}(t)$ is calculated by finding the distance between $\vec{R}(t+\ \delta)$ and $\vec{R}(t)$ and dividing by δ. Examples are shown for δ = 1 and δ = 2. To calculate $C_v^{(\delta)}(\tau)$ the average of the dot product of $\vec{v}(t+\ \tau)$ and $\vec{v}(t)$ is taken.

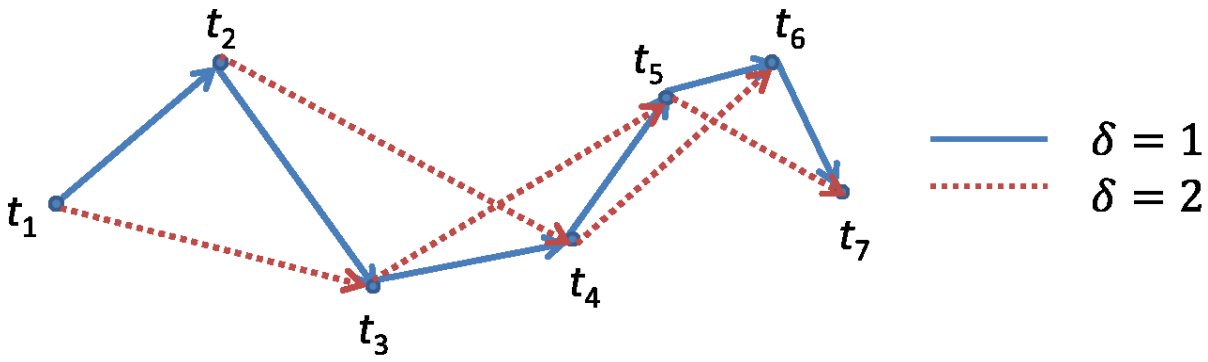

Figure 3.6. Four typical trajectories for *rrnG* foci from cells grown in EZRDM overlaid on the phase contrast image. Trajectories are 10 steps long with 0.1 s steps. They are fairly compact and do not travel far in 1 s.

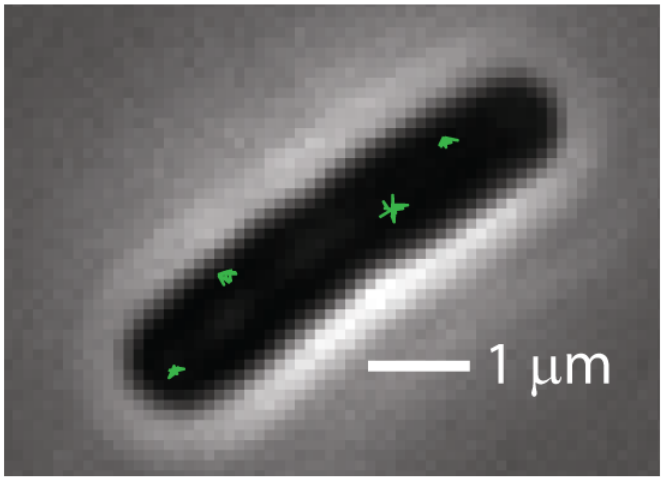

Figure 3.7. MSD(τ) for loci in cells grown in MBM and tracked at 33 Hz. All tested loci exhibit similar diffusion except Left-1, which has a slightly larger slope.

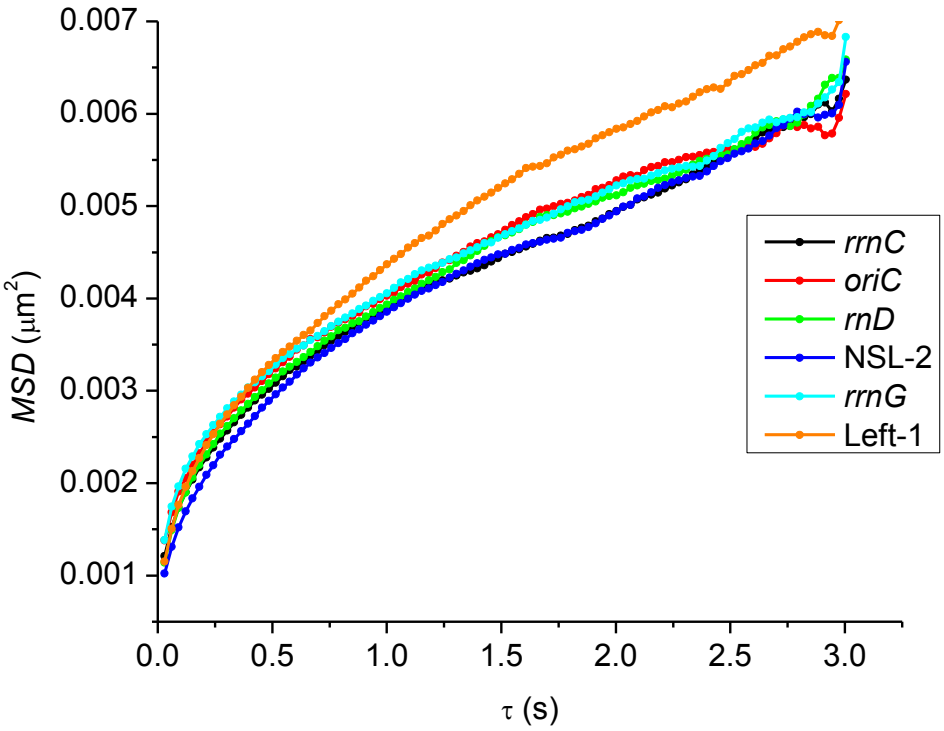

Figure 3.8. (A) *MSD*(τ) for loci in cells grown in MBM and tracked at both 33 Hz and 10 Hz overlaid. **(B)** Zoomed in region of **(A)**.

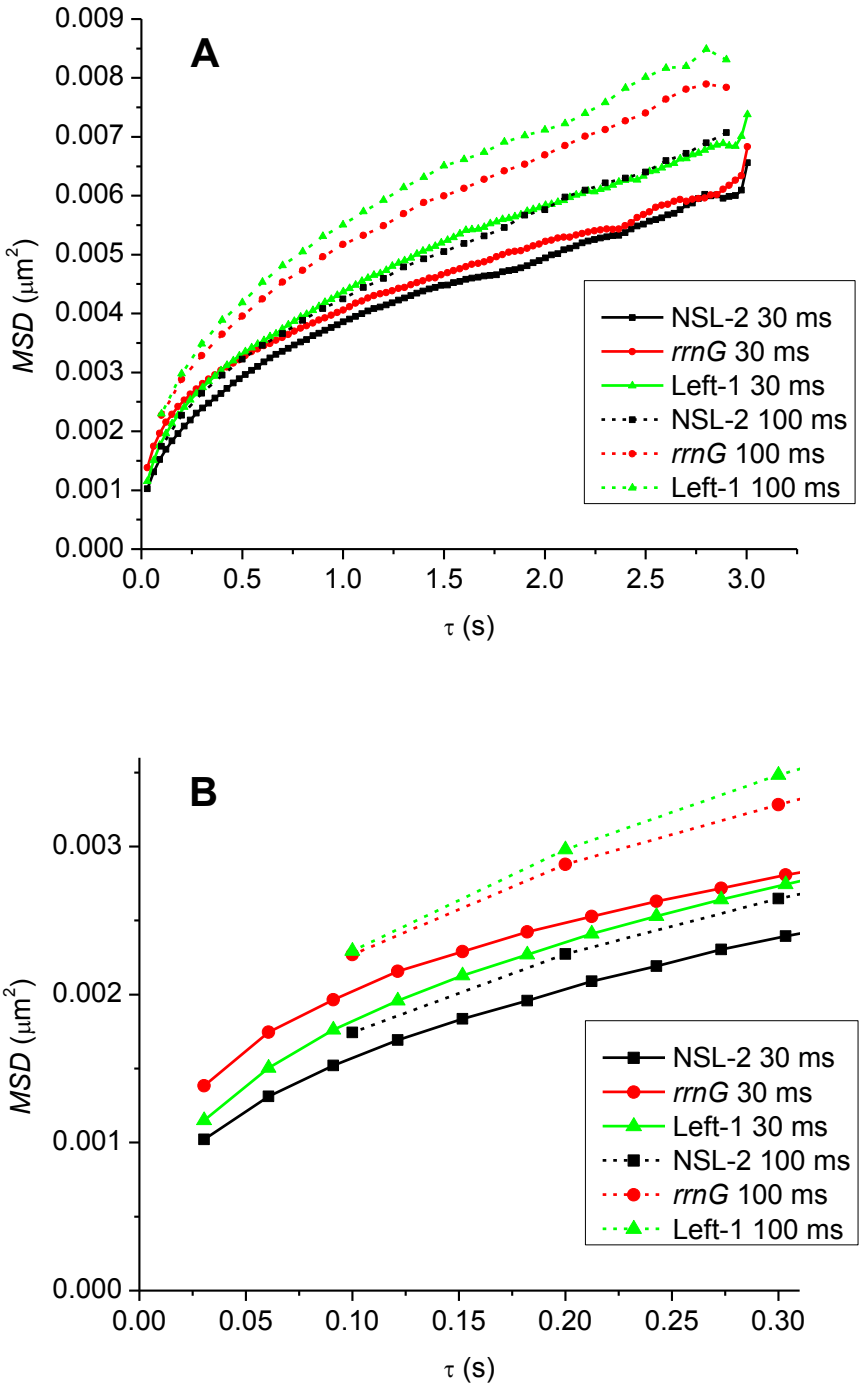

Figure 3.9. (A) Ensemble averaged *MSD*(τ) plots from trajectories truncated to 11 steps for Left-1 (725 trajectories), NSL-2 (968 trajectories), *rrnG* (502 trajectories) and the slow RNAP state (985 trajectories), defined as $D_i < 0.015\ \mu m^2/s$. *MSD* data for RNAP in cells fixed with formaldehyde is also plotted. **(B)** Distribution of D_i from 3-step trajectories of RNAP and *rrnG*. RNAP data by Somenath Bakshi and Wenting Li. Figure by Somenath Bakshi.

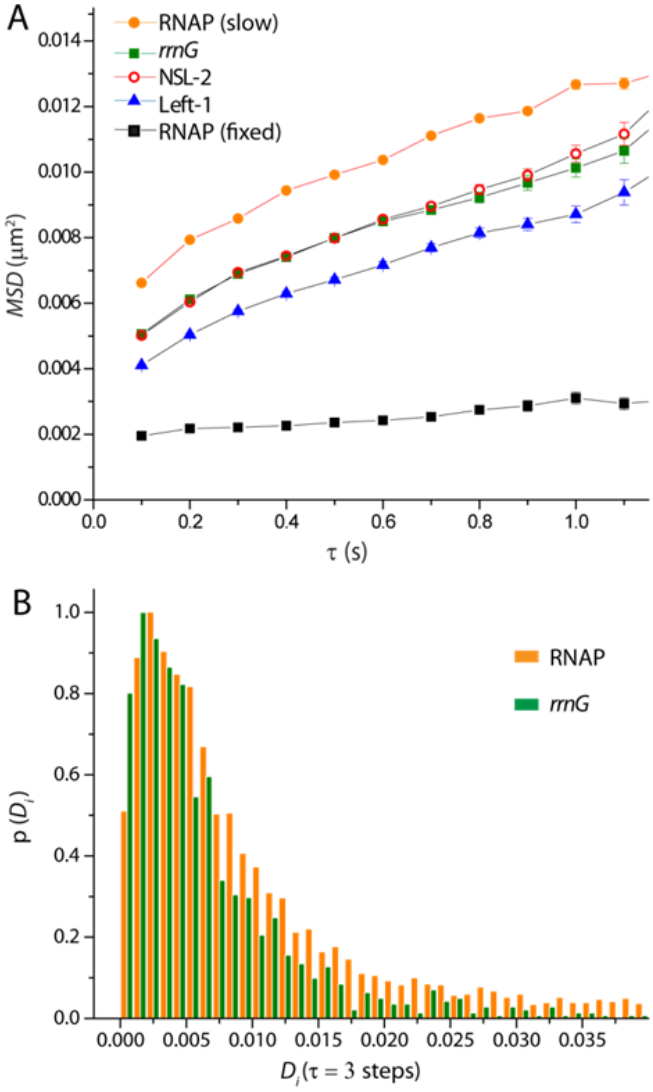

Figure 3.10. **(A)** *MSD*(τ) curves for different cutoff lengths of NSL-2 trajectories at 33 Hz in MBM. **(B)** Plot of trajectory length vs. trajectory brightness indicating which trajectories are used for the different cutoff lengths in **(A)**.

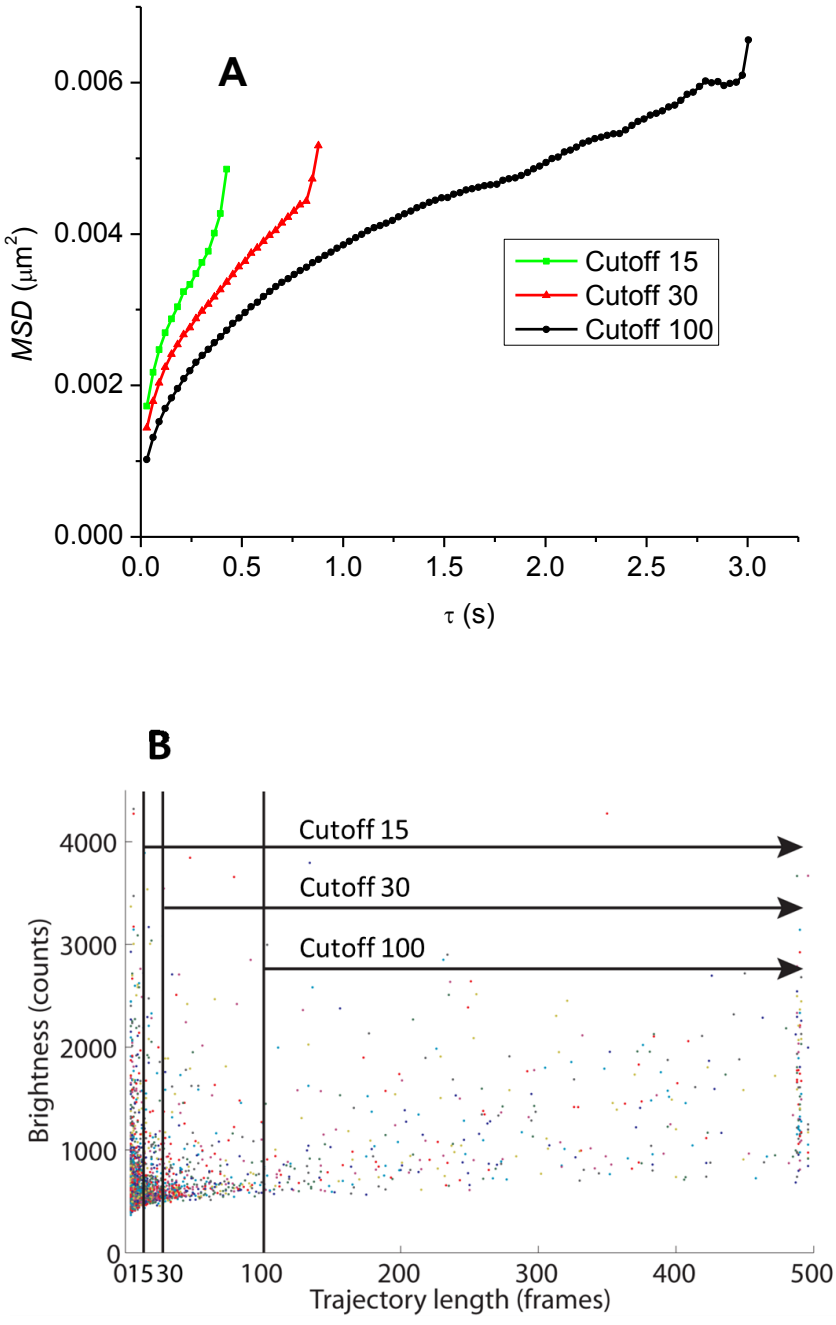

Figure 3.11. **(A)** *MSD*(τ) curves for different trajectory brightness. Curves containing all the data cut to 15 and 100 steps shown for reference. **(B)** Plot of trajectory length vs. trajectory brightness indicating which trajectories are used for the different brightness categories in **(A)**.

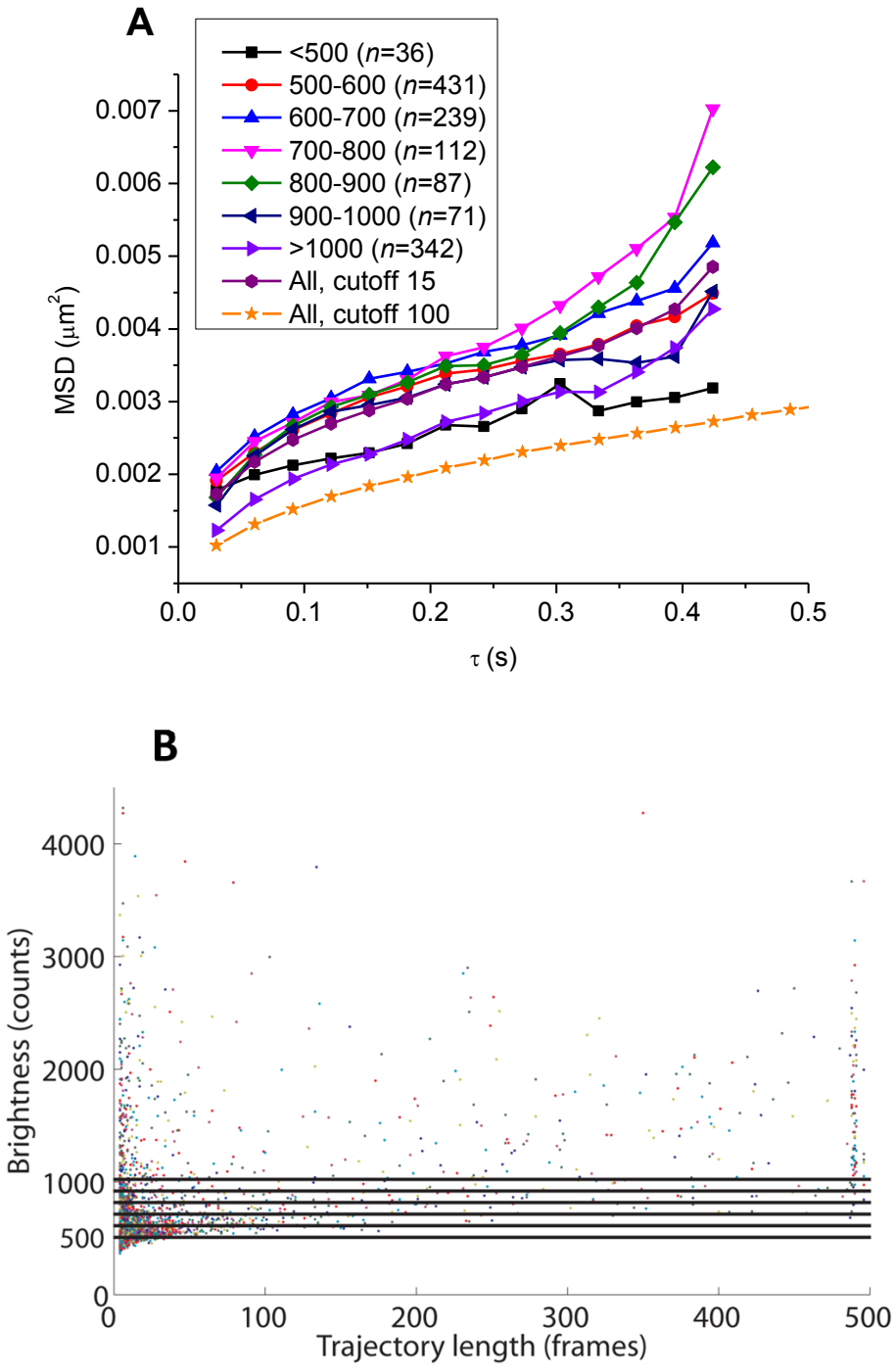

Figure 3.12. **(A)** *MSD*(τ) curves for different trajectory length groups cut to 15 steps. Curve containing all the data cut to 15 steps shown for reference. **(B)** Same as **(A)** with initial value subtracted in order to compare the curvature. **(C)** Plot of trajectory length vs. trajectory brightness indicating which trajectories are used for the different length categories in **(A and B)**.

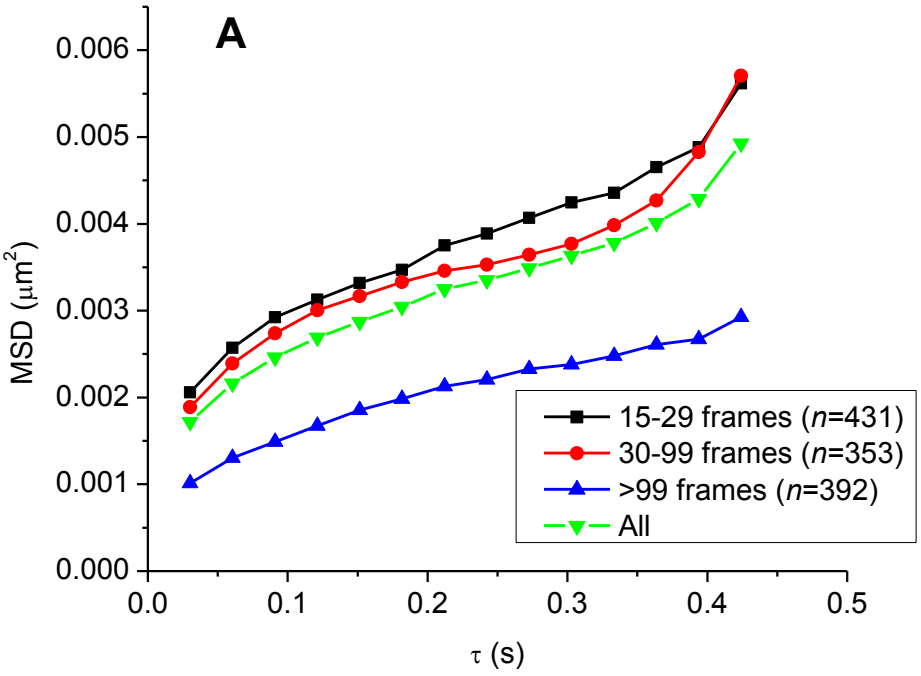

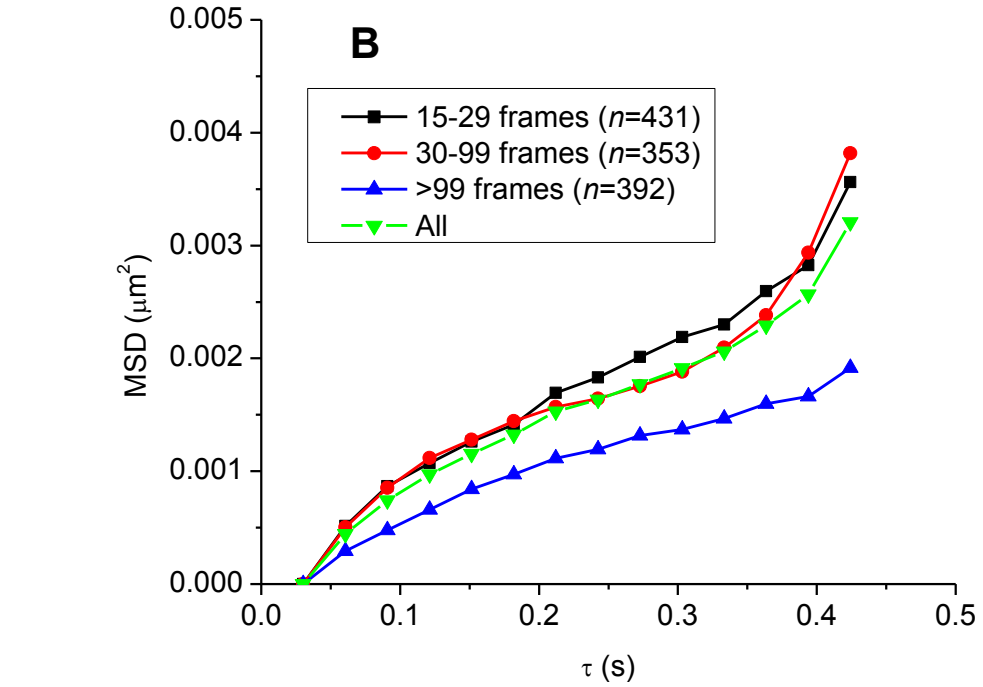
B
15-29 frames (n=431)
30-99 frames (n=353)
>99 frames (n=392)
All
MSD (μm²)
τ (s)
0.000
0.001
0.002
0.003
0.004
0.005
0.0
0.1
0.2
0.3
0.4
0.5

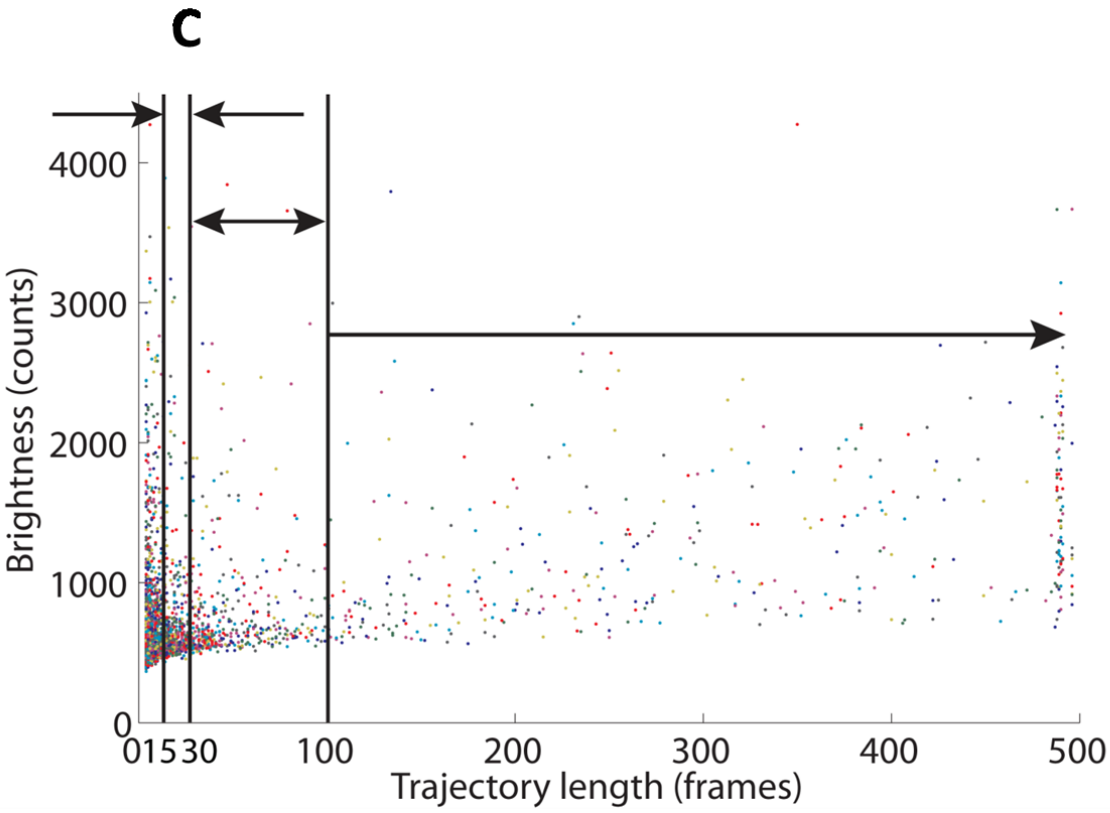
C
Brightness (counts)
Trajectory length (frames)
0
1000
2000
3000
4000
0 1 5 30
100
200
300
400
500

Figure 3.13. 488 nm beam image for 33 Hz data **(Left)** and 10 Hz data **(Right)**. Images are of a fluorescent dye sample. Bottom, profile drawn diagonally through the beam images for the 33 Hz data **(Left)** and 10 Hz data **(Right)**.

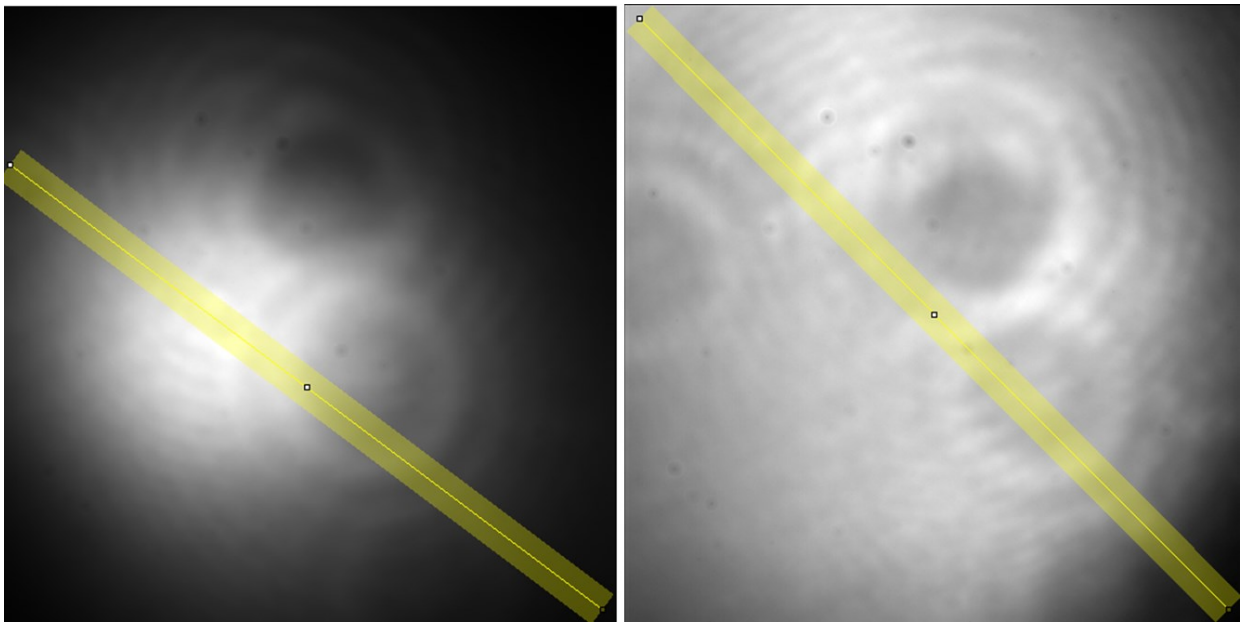

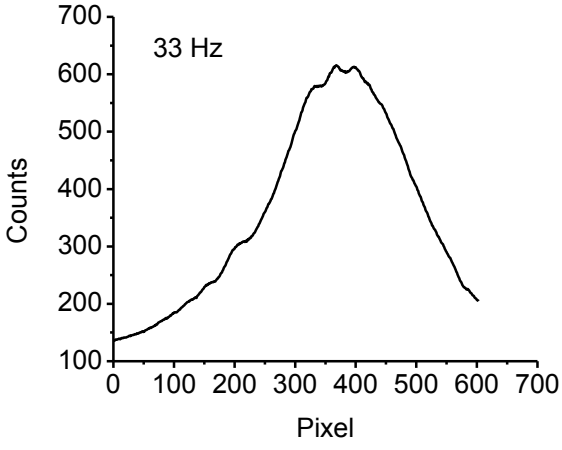

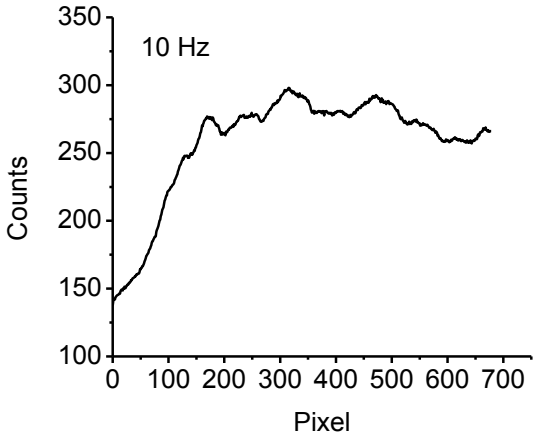

Figure 3.14. (A) *MSD*(τ) plots for cells grown in EZRDM.

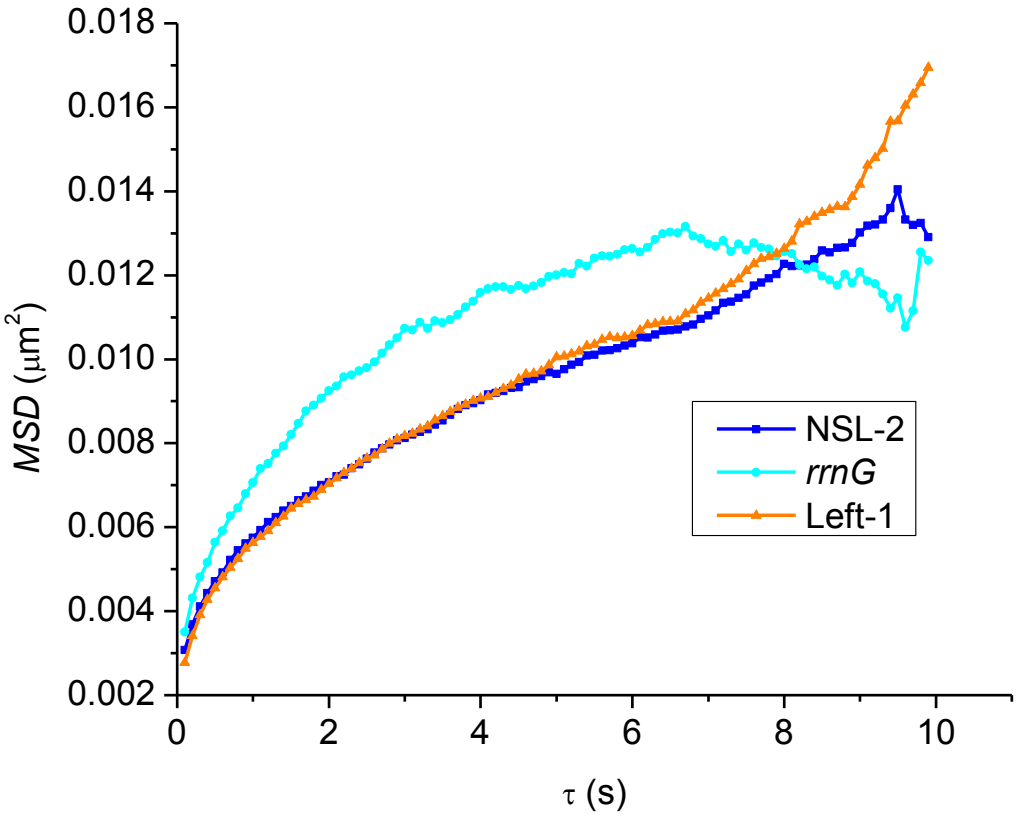

Figure 3.15. Log-log plot of *MSD*(τ) for 33 Hz data from cells grown in MBM, as in Figure 3.7. Lines are linear fits to the data from τ = 0.03-2.09. The last few points were excluded because the curves become noisy at large τ values. Slopes (α values) can be found in Table 1 and range from 0.31 to 0.39. The red and black curves show the slopes for α = 0.31 (black solid line) and α = 0.39 (red dashed line). They have been shifted up and offset from the data for clarity.

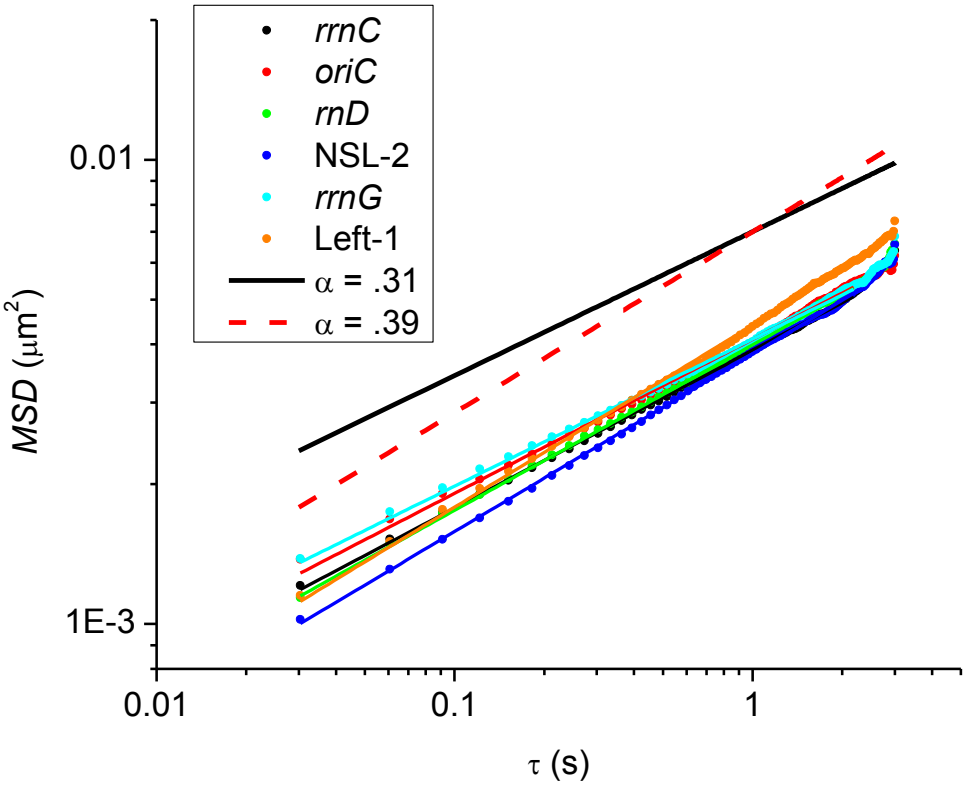

Figure 3.16. Log-log plot of *MSD*(τ) for 10 Hz data from cells grown in EZRDM as in Figure 3.14. Lines are linear fits to the data from τ = 0.1-6.5. The last few points were excluded because the curves become noisy at large τ values. Slopes (α values) can be found in Table 2 and range from 0.31 to 0.34. The red and black curves show the slopes for α = 0.31 (black solid line) and α = 0.34 (red dashed line). They have been shifted up and offset from the data for clarity.

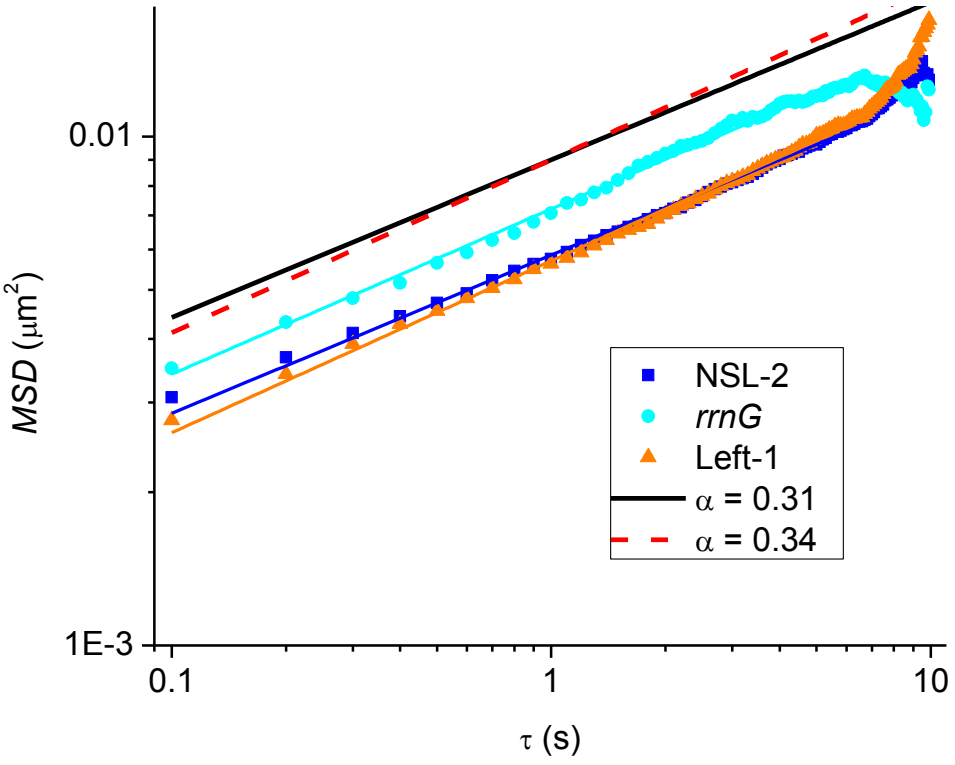

Figure 3.17. Velocity autocorrelation plots for data taken at 10 Hz from cells grown in MBM. Plots are normalized to the value at $\tau = 0$. Values were calculated using equations 3.5-3.7.

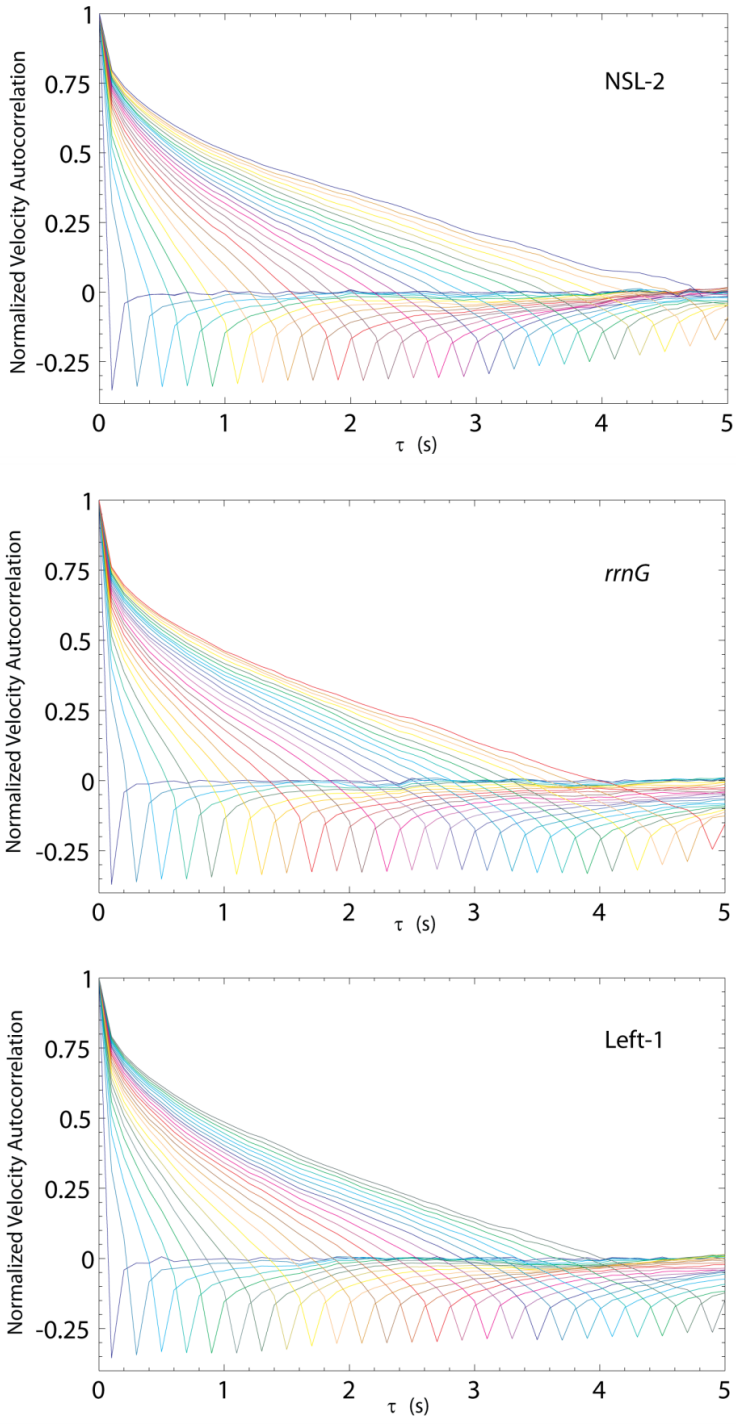

Figure 3.18. Velocity autocorrelation plot for Left-1. Data were taken at 33 Hz from cells grown in MBM.

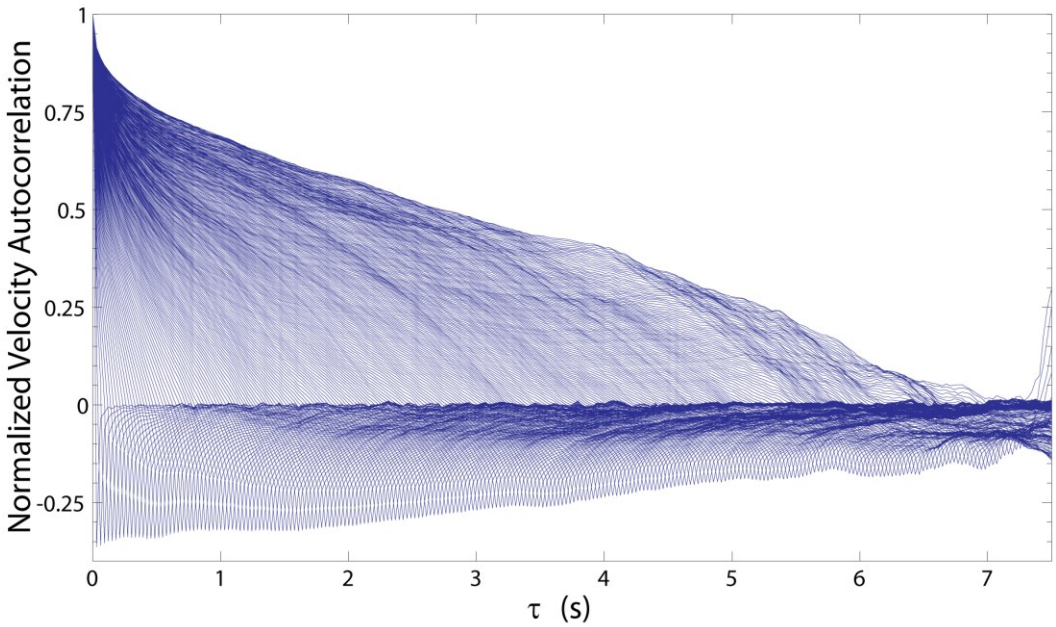

Figure 3.19. Methods of visualizing DNA loci in *E. coli*. **(A)** FROS system. In this example two positions on the chromosome are labeled with different fluorophores. The number of fluorophores which make up a focus can be controlled by the number of *tetO* or *lacO* sites that are inserted. **(B)** GFP-ParB/*parS* system. Multiple GFP-ParB molecules bind to the *parS* site with no method to control the total number. Figure reproduced from Wang *et al.* 2008.[19]

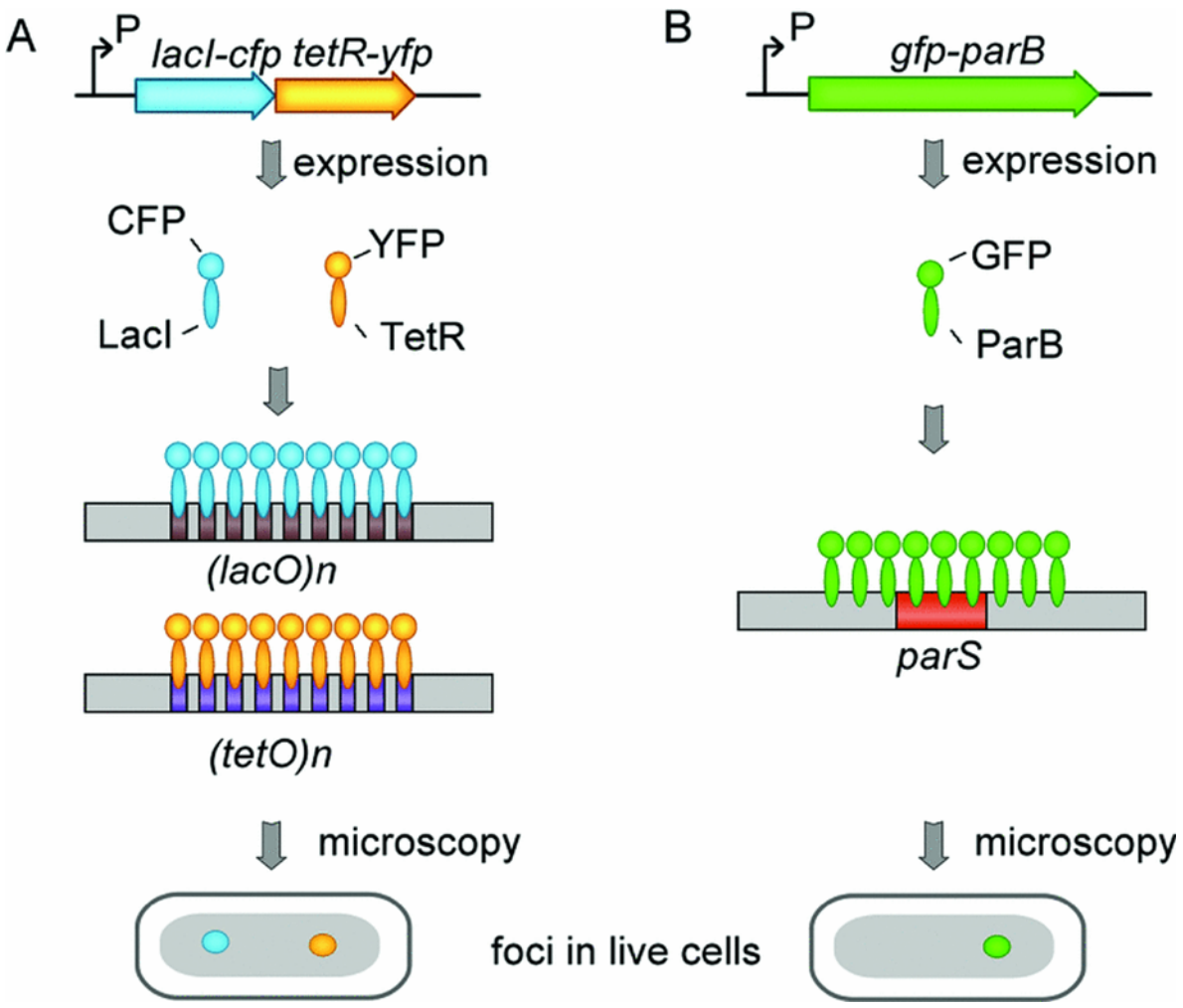

References

1 Niki, H., Yamaichi, Y. & Hiraga, S. Dynamic organization of chromosomal DNA in Escherichia coli. *Genes Dev.* **14**, 212-223 (2000).

2 Valens, M., Penaud, S., Rossignol, M., Cornet, F. & Boccard, F. Macrodomain organization of the Escherichia coli chromosome. *EMBO J.* **23**, 4330-4341 (2004).

3 Li, Y., Sergueev, K. & Austin, S. The segregation of the Escherichia coli origin and terminus of replication. *Molecular Microbiology* **46**, 985-996, doi:10.1046/j.1365-2958.2002.03234.x (2002).

4 Weber, S. C., Thompson, M. A., Moerner, W. E., Spakowitz, A. J. & Theriot, J. A. Analytical Tools To Distinguish the Effects of Localization Error, Confinement, and Medium Elasticity on the Velocity Autocorrelation Function. *Biophysical Journal* **102**, 2443–2450 (2012).

5 Michalet, X. Mean Square Displacement Analysis of Single-Particle Trajectories with Localization Error: Brownian Motion in Isotropic Medium. *Phys Rev E Stat Nonlin Soft Matter Phys.* **82**, 041914 (2010).

6 Espeli, O., Mercier, R. & Boccard, F. DNA dynamics vary according to macrodomain topography in the E. coli chromosome. *Molecular Microbiology* **68**, 1418–1427 (2008).

7 Nielsen, H. J., Li, Y., Youngren, B., Hansen, F. G. & Austin, S. Progressive segregation of the Escherichia coli chromosome. *Molecular Microbiology* **61**, 383-393, doi:10.1111/j.1365-2958.2006.05245.x (2006).

8 Nielsen, H. J., Ottesen, J. R., Youngren, B., Austin, S. J. & Hansen, F. G. The Escherichia coli chromosome is organized with the left and right chromosome arms in separate cell halves. *Molecular Microbiology* **62**, 331-338, doi:10.1111/j.1365-2958.2006.05346.x (2006).

9 Weber, S. C., Spakowitz, A. J. & Theriot, J. A. Bacterial Chromosomal Loci Move Subdiffusively through a Viscoelastic Cytoplasm. *Physical Review Letters* **104**, 238102 (2010).

10 Chung, C. T., Niemela, S. L. & Miller, R. H. One-step preparation of competent Escherichia coli: Transformation and storage of bacterial cells in the same solution. *Proc. Natl. Acad. Sci. USA* **86**, 2172-2175, (1989).

11 Bakshi, S., Dalrymple, R. M., Li, W., Choi, H. & Weisshaar, J. C. *Partitioning of RNA Polymerase Activity in Live E. coli from Analysis of Single-molecule Diffusive Trajectories* (2013).

12 Neidhardt. F. C., Bloch, P. L. & Smith, D. F. Culture Medium for Enterobacteria. *Journal of Bacteriology* **119**, 736-747 (1974).

13 Konopka, M. C., Weisshaar, J. C. & Record, M. T., Jr. Methods of changing biopolymer volume fraction and cytoplasmic solute concentrations for in vivo biophysical studies. *Osmosensing and Osmosignaling* **428**, 487-504, doi:10.1016/s0076-6879(07)28027-9 (2007).

14 Wang, T., Ingram, C. & Weisshaar, J. C. Model Lipid Bilayer with Facile Diffusion of Lipids and Integral Membrane Proteins. *Langmuir* **26**, 11157-11164, doi:10.1021/la101046r (2010).

15 Crocker, J. C. & Grier, D. G. Methods of digital video microscopy for colloidal studies. *J. Colloid Interface Sci.* **179**, 298-310 (1996).

16 Bakshi, S., Bratton, Benjamin P. & Weisshaar, J. C. Subdiffraction-Limit Study of Kaede Diffusion and Spatial Distribution in Live Escherichia coli. *Biophysical journal* **101**, 2535-2544 (2011).

17 Weber, S. C., Spakowitz, A. J. & Theriot, J. A. Nonthermal ATP-dependent fluctuations contribute to the in vivo motion of chromosomal loci. *Proceedings of the National Academy of Sciences*, doi:10.1073/pnas.1119505109 (2012).

18 Javer, A. *et al.* Short-time movement of E. coli chromosomal loci depends on coordinate and subcellular localization. *Nature Communications* **4**, 3003 (2013).

19 Wang, X., Reyes-Lamothe, R. & Sherratt, D. J. Visualizing genetic loci and molecular machines in living bacteria. *Biochemical Society Transactions* **36**, 749–753 (2008).

20 Wang, W., Li, G.-W., Chen, C., Xie, X. S. & Zhuang, X. Chromosome Organization by a Nucleoid-Associated Protein in Live Bacteria. *Science* **333**, 1445-1449, doi:10.1126/science.1204697 (2011).

21 Hensel, Z., Weng, X., Lagda, A. C. & Xiao, J. Transcription-Factor-Mediated DNA Looping Probed by High-Resolution, Single-Molecule Imaging in Live <italic>E. coli</italic> Cells. *PLoS Biol* **11**, e1001591, doi:10.1371/journal.pbio.1001591 (2013).

Chapter 4

Distribution of *E. coli* DNA loci in the short dimension

Introduction

This chapter probes the spatial organization of the *E. coli* chromosome along the short axis of the cell (*y*). Previous studies have found specific organization along the long axis (*x*).[1-8] DNA loci are arranged linearly along *x* according to their position on the chromosome map.[1] This discovery was instrumental in changing the idea that the *E. coli* cell is simply a disordered "bag of protein and DNA" to the fact that it is instead highly organized. We seek here to discover if there is also organization in the previously understudied *y* dimension.

Materials and methods

Bacterial strains

The DNA loci strains which were used are described in Chapter 3. Their positions on the chromosome can be found in Figure 1. To image the nucleoid, Wenting Li created HU-mEos2, which was expressed from plasmid (pASK-IBA3plus). Strain construction details can be found in Bakshi *et al.*.[9]

Cell growth and sample preparation

Cells were grown as described in Chapter 3.

Imaging

For the $P(y)$ studies described here, a phase contrast image was acquired, which was used to determine the shape and location of the cells. A fluorescence image (100 ms exposure) was then taken to locate the fluorescent foci (Figure 2). Data was taken for only ten minutes on each chamber. Microscope details can be found in Chapter 3.

Data analysis

Peak finding was performed as described in Chapter 3.

Cell-based coordinate system

The foci positions were superimposed onto a curvilinear, cell-based coordinate system in order to determine their positions relative to the cell envelope. This is important because it accounts for the curvature of the cells, which greatly affects the $P(y)$ distribution as compared with a rectilinear coordinate system. This was accomplished using the Microbetracker Suite developed by the Jacobs-Wagner lab.[10] First, the cells were outlined and then the central spine of the cell was determined (Figure 3). The original x, y coordinates of the molecules were then transformed to the new cell based coordinate system. This was accomplished by using the piece of the software suite "projectToMesh.m," which finds the perpendicular distance from the center spine of the cell (y') and the distance from one of the cell poles along that center line (x') (Figure 3).

P(y') distributions

In order to determine if there is a preferred *y'* location for a given locus, histograms of their positions were generated. Since there are only a few copies of each locus per cell, data from multiple cells were combined. This provided an average picture of where the loci are located in the *y'* dimension.

The strains in this work came from two different backgrounds (VH1000 and MG1655). In general, MG1655 cells are smaller and grow slower than VH1000 cells due to a mutation which leads to pyrimidine starvation in minimal media. This makes a direct comparison of the radial profiles of cells from these different backgrounds difficult. In order to compare the data from these backgrounds, they were normalized to the average cell radius (value of 0 at the cell center to 1 at the edge). Radius measurements were performed using the method described in Bakshi *et al.* 2011.[11] Briefly, the *y'* distribution of a free photoactivatable cytosolic protein (Kaede) was measured and fit to a model function in order to determine the diameter of the cytoplasm. Half of this value was taken as the radius of the cell. When VH1000 cells are grown in MBM or EZRDM at 37 °C the average radius is 315 ± 26 nm or 445 ± 25 nm, respectively. The average value of the radius for MG1655 cells grown in EZRDM at 37 °C is 424 ± 20 nm. Radius measurements of VH1000 cells grown in EZRDM were performed by Somenath Bakshi. The distributions were also normalized by the total number of foci to obtain the probability of being at a certain *y'* (*P*(*y'*)). *P*(*y'*) histograms consist of data from at least 300 foci.

The *P*(*y'*) distributions were compared to the distribution of a uniformly filled cylinder with *r* equal to the average cell radius and σ equal to the localization precision of the foci

position measurements. This value of σ was determined from the MSD curves for the 33 Hz data in Chapter 3 by extrapolating to obtain the *y*-intercept. The values of σ were calculated as

$$\sigma = \sqrt{\frac{y\ intercept}{4}}. \quad \textbf{(4.1)}$$

The value of σ is 25 nm or 16 nm for the EZRDM or MBM data respectively. These are likely over estimations of the error because the *MSD*(*t*) curves are bent such that their slopes continue to increase at smaller time-scales. This makes the true intercept difficult to acquire through extrapolation. The signal to noise ratio of the foci intensity to background was also higher in these experiments. The data taken for these studies had a longer exposure time (100 ms) vs that of the diffusion studies (30 ms).

Results

DNA loci distributions in the short dimension

DNA loci exhibit different spatial distributions along the short dimension of the cell (*y*'). Raw data histograms can be found in Figures 4 and 5. Normalized *P*(*y'*) distributions are shown in Figures 6 and 7. For cells with a background of VH1000 and grown in moderate growth conditions (EZRDM, doubling time of ~35 min), a locus at *ter* is found on average in the center while other tested loci are found preferentially away from the center. Of the tested positions, the distributions of *rrnG* and *oriC* peak the furthest from the center (approximately 0.65*r* or 290 nm). The *rrnD* distribution peaks about 0.45*r* (200 nm) from the center.

Several loci in the MG1655 background were also grown in EZRDM and studied (NSR-2, Right-2, Left-1) (Figures 5 and 6). The distribution of NSR-2 *y'* positions peaks at 0.5*r* (223 nm), that of Right-2 peaks at 0.55*r* (250 nm), and that of Left-1 peaks at 0.45*r* (200 nm) from the cell center.

In poorer growth conditions (MBM, doubling time of ~60 min), the trend of localization away from the cell center is also present for some loci, but is not as strong (Figures 4 and 7). This is possibly due to the fact that the cells are narrower (315 ± 26 nm radius) so the dip in the *P*(*y*') distributions is harder to resolve. The localization away from the center is still especially noticeable in the *rrnG* distribution, which peaks at ~0.7*r* (220 nm) from the center. The distribution of *oriC* and *rrnD* for the MBM data look very similar to the uniform distribution, although the distribution of *oriC* may be slightly peaked outwards at 0.35*r* (110 nm) from the center. *ter* is more peaked towards the center in EZRDM, while its distribution in MBM appears to have two peaks, one in the center and one at 0.65*r* (205 nm).

Discussion

Comparison with a previous study

There is one other study of DNA loci distributions in the short dimension of the cell by Meile *et al.*.[12] They observed that their *ori* and *right* loci were uniformly distributed in the *y* dimension, *NS-right* localized towards the cell center, and *ter* was located primarily at the periphery.[12] They also sorted the *ter* data by whether there were one or two foci in the cell. The

foci from cells with one focus tended to be more peripherally located. Those from cells with two foci were more centrally located. These results are somewhat similar to the results obtained here for the cells grown in MBM, especially for *ter*; however, the growth conditions are significantly different. They used a YFP-ParB/*parS* labeling system. Cells were grown in M9 medium supplemented with 0.2% casamino acids, 0.4% glucose, 2 μg/ml thiamine, 20 μg/ml leucine, and 20 μg/ml thymine at 42 °C. The cells had a doubling time of 45 min which is between that of our two conditions.[12] The distributions observed for the two different growth conditions studied here differ, so there is reason to believe that the distribution of locus' locations in *y'* is dependent on growth conditions. This makes a direct comparison between the two studies difficult, but it appears that for *ter* an additional peak arises towards the periphery when the cells grow more slowly.

Nucleoid structure determined from HU distribution

In order to examine if the *P*(*y'*) distributions observed here match the distribution of the entire nucleoid, the distribution of the DNA binding protein HU was determined for cells grown in EZRDM (Figure 8). In contrast to the majority of the measured *P*(*y'*)s for individual loci, the HU *P*(*y'*) distribution peaks at the center of the cell. When compared to a model for a uniformly filled cylinder that has a radius equal to that of the cytoplasm (445 ± 25 nm), it is obvious that HU does not uniformly fill the cytoplasm, but is more centrally located. This is quite different from the distributions of the individual DNA loci studied here, most of which peak away from the cell center. Possible reasons for this discrepancy are discussed below.

Labeling artifacts?

GFP-ParB/parS system

There are several possible explanations for the disagreement between the HU and DNA loci distributions. It is possible that the observed distributions are due in part to an artifact of the labeling schemes. The GFP-ParB/*parS* labeling scheme results in ~50-100 copies (roughly estimated from the amount of time it takes a focus to bleach compared to a typical single molecule) of the ParB-GFP protein binding to the DNA locus of interest. Earlier work in our group has shown that ribosomes in *E. coli* tend to be excluded from DNA simply due to their size, and thus are found at the periphery of the cell.[13,14] Since a ribosome has a molecular weight of ~2.7 x 10^6 Da, GFP is 238 amino acids, and ParB is 343 amino acids, and 1 amino acid equals ~110 Da, the GFP-ParB complex is ~63 kDa. This means that if ~43 GFP-ParB proteins were to bind to the *parS* site then the focus would be the size of a ribosome. Although bound to the DNA itself, it is possible that such a large object would tend to be excluded from the rest of the DNA, and thus distribute preferentially towards the periphery of the nucleoid.

In order to test if locus brightness, and thus size, affects its position, we grouped the data by their brightness (integrated intensity in a 3x3 pixel box around the center of the diffraction limited spot in the band passed image). $P(y')$ distributions of different brightness groups were compared (Figure 9). A two sample Kolmogorov-Smirnov test (kstest2, MATLAB) was used to determine the likelihood that the different curves came from different distributions. This test computes the maximum absolute difference between the cumulative distribution functions (CDF) of the two distributions. The value of the CDF at x is the proportion of values from the distribution which are less than or equal to x. The test either accepts or rejects the null

hypothesis that the two distributions come from the same distribution at a certain significance level, α. The test reports a *p* value which is the probability of observing a test statistic as extreme as, or more extreme than, the observed value under the null hypothesis. This *p* value is then compared to α to decide whether to reject the null hypothesis.

For *oriC*, *rrnD*, and *ter* the null hypothesis that they came from the same distribution could not be rejected at α = 0.05 (*p* equals 0.72 for *oriC*, 0.62 for *rrnD*, 0.79 for *ter* comparing data for 0-2500 and >5000 counts, and 0.66 for *ter* comparing data for 2500-5000 and >5000 counts). *rrnG* however, had significantly smaller *p* values at 0.02 for the curves for counts between 0-5000 and 5000-10000, and 0.01 for counts between 0- 5000 and >10000 leading to a rejection of the null hypothesis that they came from the same distribution at α = 0.05. However, if only the foci with brightness <10,000 counts are considered, the distribution still peaks at almost 300 nm from the center of the cell (Figure 9 red and black curves).

It cannot be ruled out that even the dimmest loci consist of enough ParB-GFP molecules to be large enough objects to be forced outwards. However, if this were the case one could argue that *ter* should also be located towards the outside of the cell and it is peaked primarily in the center of the cell for the EZRDM data.

Does HU bind evenly to the DNA?

It is also possible that HU does not bind uniformly to DNA. Yazdi, Marko *et al.* used labeled DNA binding proteins as a marker for the nucleoid. They described a haze around the nucleoid when they used HU-GFP as opposed to Fis-GFP.[15] They attributed this to HU not binding as tightly to the DNA as Fis. If the DNA is actually hollow, unbound HU could cause

our $P(y')$ distribution to be artificially filled in in the center. However, it is unlikely that this would result in the observed HU distribution, which can be well represented by that of a uniformly filled cylinder (of smaller radius than the cytoplasm) (unpublished data). Also, in our experiments performed by Wenting Li, we likely only obtain positional information for HU molecules which are tightly bound to DNA. Those that are not bound are likely diffusing so quickly that they will not be resolved at our exposure times. In order to be sure that the HU distribution properly represents the distribution of the nucleoid it should be verified with a second labeling scheme, perhaps Fis-GFP.

The nucleoid may be hollow

If the observed loci distributions are representative of the entire nucleoid, they suggest that the overall nucleoid structure is slightly hollow or less dense in the center. This is in line with recent suggestions that the nucleoid is arranged in a coiled or helical pattern.[15,16] It is possible, although not necessary, for a helical shape to be hollow in the center. Yazdi *et al.* studied the *E. coli* chromosome using the nucleoid-associated protein Fis labeled with GFP by an inducible gene. They used epifluorescence imaging, z stacks and deconvolution to show that the nucleoid appears as a coil rather than a disorganized mass. This was observed for cells grown in three different growth mediums: LB, minimal M9, and minimal AB media. They also repeated their studies and obtained similar results using the DNA-binding protein HU fused to GFP.[15] Fisher *et al*. visualized the nucleoid by labeling HU via its HupA subunit (HupA-mCherry) and saw that it is a helical ellipsoid. When cross-sections perpendicular to the nucleoid length were examined, many slices exhibited two areas of high intensity stacked on top of each other, while others exhibited a single “bulls-eye” pattern. This was interpreted by the authors as longitudinal

bundles of DNA and is consistent with our observation of $P(y')$ plots peaking away from the center of the cell. The observed helical bundle patterns are dynamic, but are reported as being present at all stages of the cell cycle.[16] This agrees with the fact that we see these types of distributions in our data, which includes data from all stages of the cell cycle. In addition, similar helical nucleoid structures have been observed in both *B. subtillis* and *C. crescentus* suggesting universality of this type of DNA structure in bacteria.[17,18]

Transcription may cause peripheral distributions

It is possible that the tested loci, which comprise a very small fraction of all the DNA loci, were coincidentally located away from the center (with the exception of *ter*) due to their proximity to a highly transcribed gene. When genes for membrane proteins are transcribed, they migrate towards the outer edge of the nucleoid and drag a length of DNA with them.[19] This was observed in a study by Libby *et a*l., in which the gene encoding for the membrane protein lactose permease (LacY) migrated outward when induced, compared to its normal position.[19] They found that this outward movement affected DNA > 90 kb away, but not ~170 kb away. There are ~1,000 genes that are predicted to encode for membrane proteins on the chromosome. If a large number of them are expressed it will likely play a large role in shaping the overall structure of the nucleoid, and may explain our observations of a partially hollow nucleoid. It would be interesting to determine the proximity of our studied loci to genes for membrane proteins. We could then see how this affects the $P(y')$ distributions of the loci in different growth conditions.

Libby *et a*l. saw that the extent of locus repositioning increases with the expression level of the protein.[19] If this is true of all highly transcribed genes, not just those encoding for

membrane proteins, then this would affect an even larger portion of the chromosome. For example, the *rrn* operons *rrnC* and *rrnA* are both located within 125 kb of *oriC*. Since *rrn* operons are transcribed heavily, in rich growth conditions, *oriC* may be pulled outwards. Our lab has shown that slowly moving RNAP molecules and RNAP foci (which likely coincide with *rrn* operons) tend to be located slightly out towards the periphery in cells grown in EZRDM (unpublished results). Berger *et al.* observed that *oriC* is in fact located in close physical proximity to RNAP foci, but *ter* is not.[20] In addition, when the transcription regulator *hup*A/B is mutated the proximity of *oriC* and RNAP foci is lost.[20] This suggests that *oriC* is pulled close to the highly transcribed *rrn* operons while they undergo transcription. Berger *et al.* also define a chromosomal domain, the "*rrn* macrodomain" which they estimate extends from *oriC* through the non-structured regions on either side of the chromosome. If all the regions in this macrodomain are affected by high levels of transcription by being pulled outwards, then that would explain the $P(y')$ distributions observed here for all but Right-2 and Left-1. Perhaps the domain extends slightly further to include these locations, leaving only the terminal macrodomain unaffected. Or, it is possible that there are other highly transcribed regions or codes for membrane proteins near these loci which are outside of the *rrn* macrodomain, causing their peripheral locations.

The question remains as to whether the studied genes are always located at the periphery or only during times of high transcription. One hint may be that the loci are located less peripherally when cells are grown in MBM than in EZRDM. In EZRDM there is likely more transcription of *rrn* operons occurring, due to the faster growth, causing the operons and the loci near them to be distributed peripherally. However, the degree to which the loci are outwards is

harder to resolve in MBM due to the smaller cell radius (315 ± 26 nm compared to 445 ± 25 nm in EZRDM). In order to test the dependence of focus' *y'* position on transcription one could halt transcription with the antibiotic rifampicin, but this is known to cause drastic changes in the overall nucleoid structure and would likely not produce interpretable results.

Conclusions

It has been shown here that GFP-ParB labeled DNA loci are specifically organized not only in the long axis of the cell, but also the short axis. Specific loci have preferential locations which are dependent on the growth conditions of the cells. Tested loci were generally more peripherally located in richer growth conditions with the exception of *ter*, which is found more often near the centerline. These results suggest that on average the *E coli.* nucleoid exhibits some degree of hollowness. It is possible that loci are excluded from the bulk of the nucleoid due to the GFP-ParB/*parS* labeling system. This work should be verified using a different labeling scheme such as a fluorescent repressor operator system (FROS), which was described in Chapter 3. Additional studies would also be necessary to understand the biological significance of the observed organization.

Future studies

Repeat the P(y') studies using FROS

The *P*(*y'*) distributions should be verified using an alternative, less bulky, labeling system such as FROS (as described in Chapter 3). This would determine if the peripheral distributions are due to the GFP-ParB/*parS* labeling system and to what degree.

Does the organization correspond to cell cycle?

We have not observed a specific pattern in the DNA loci distributions that corresponds to the loci's locations on the chromosome or order of replication. In order to determine if the stage of the cell cycle determines the shape of the distributions, one could potentially use the cell length, focus' *x'* position, or number of foci in the cell as a proxy for cell cycle. The *P*(*y*') data could be sorted by these criteria in order to see if there is any dependence of the focus' *y'* position on cell cycle.

Slower growth conditions

The interpretation of these *P*(*y*') distributions is difficult considering that there are likely multiple copies of the chromosome in the cell: as many as six in the case of EZRDM. These measurements could be repeated in very poor medium such as AB medium in order to ensure that there is only a single copy of the DNA in newly born cells. This would simplify the interpretation of the *P*(*y'*) data and possibly allow clear trends to emerge.

Figures

Figure 1. Location of labeled loci on the chromosome map. Figure adapted from Valens *et al*., 2004.[21]

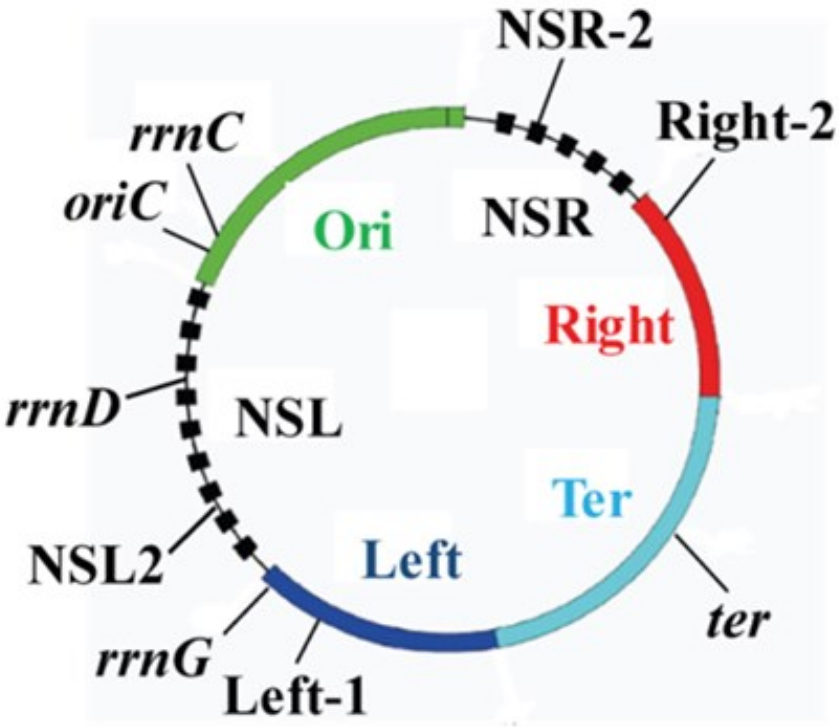

Figure 2. Example fluorescent and phase contrast image of *oriC* and *ter* foci in cells grown in MBM and EZRDM. Scale bars are 2 μm. Since *oriC* is replicated first and *ter* last, these images show the maximum and minimum number of foci per cell in each growth condition.

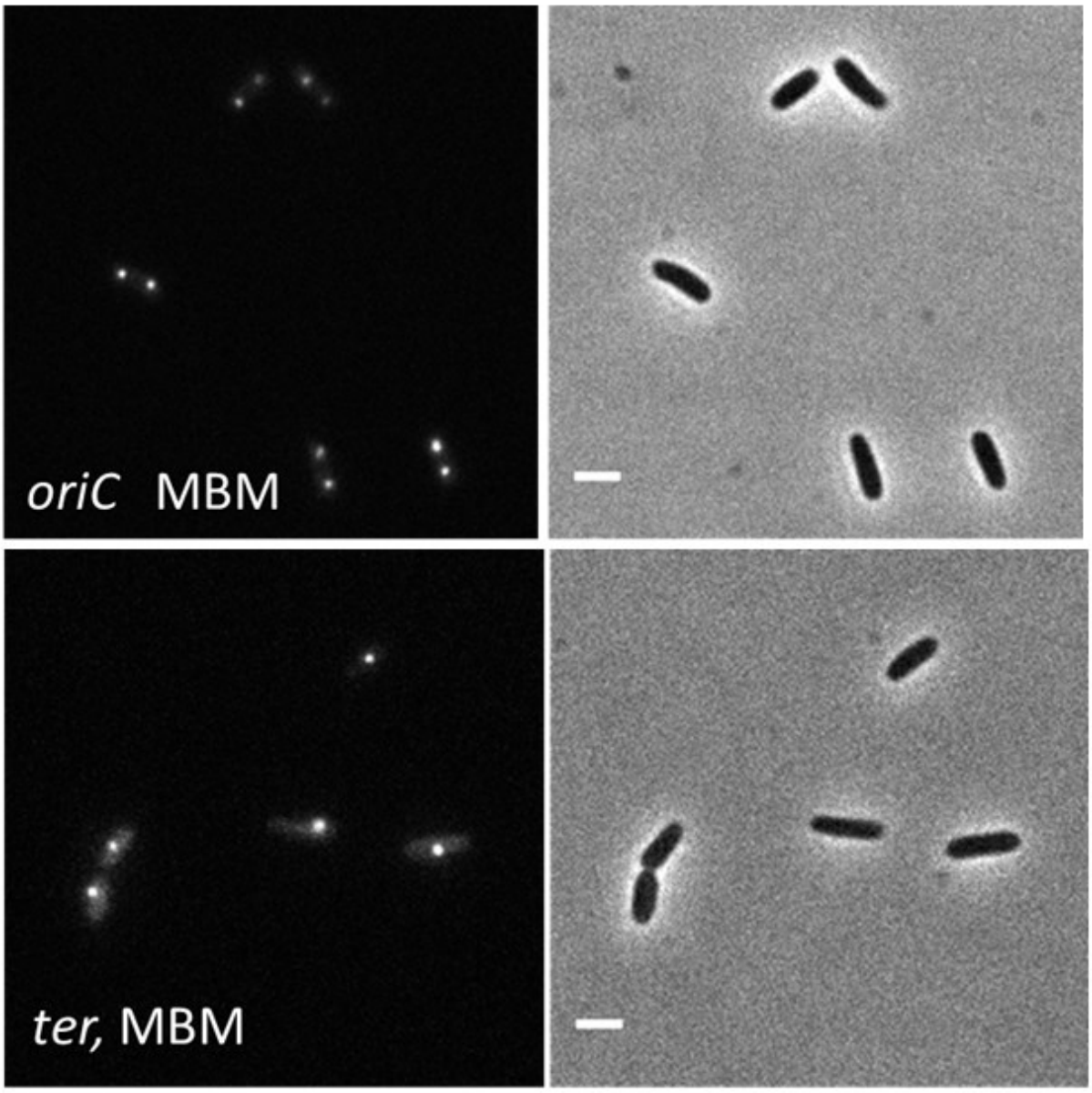

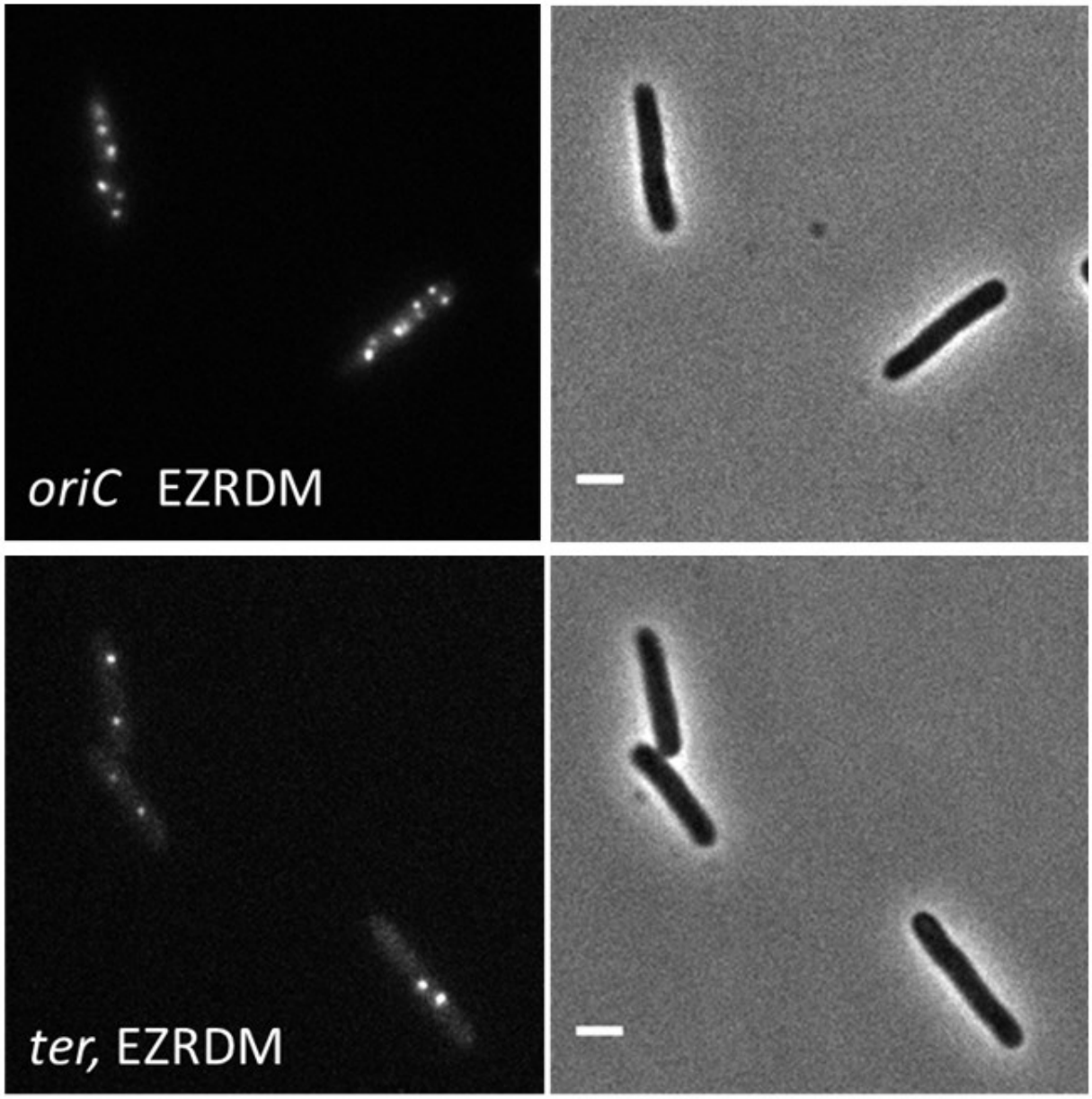
oriC EZRDM
ter, EZRDM

Figure 3. Cell-based coordinate system where *x'* is the distance along the center spine and *y'* is the perpendicular distance from the center spine. Figure reproduced and modified from Sliusarenko *et al*..[10]

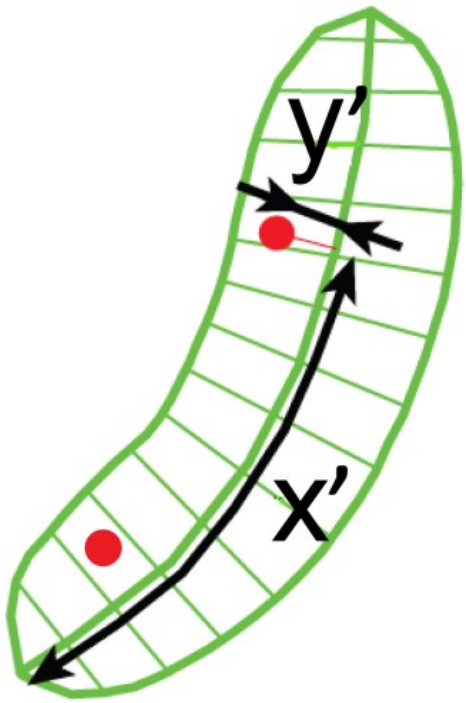

Figure 4. Specific foci have different distributions in *y'*. *y'* histograms for various positions around the chromosome for cells with a VH1000 background grown in moderately rich (EZRDM) and poor (MBM) medium.

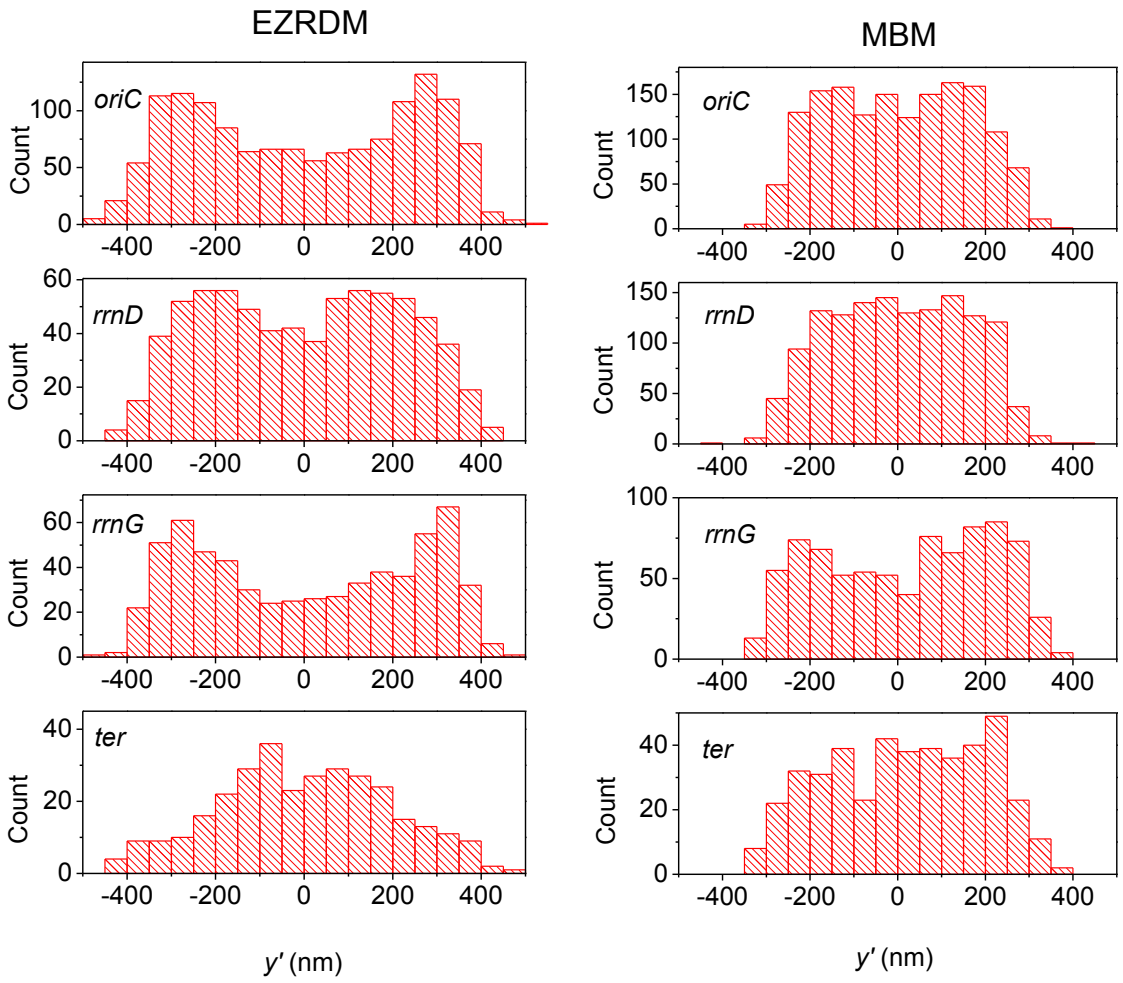

Figure 5. *y'* histograms for cells with an MG1655 background grown in EZRDM.

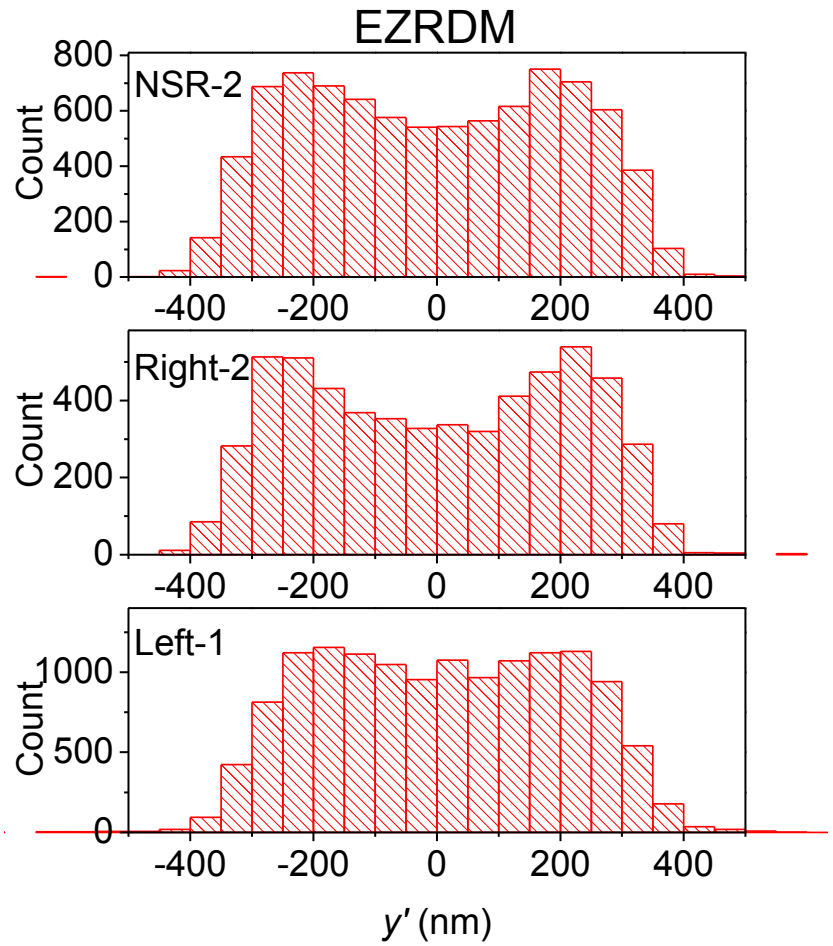

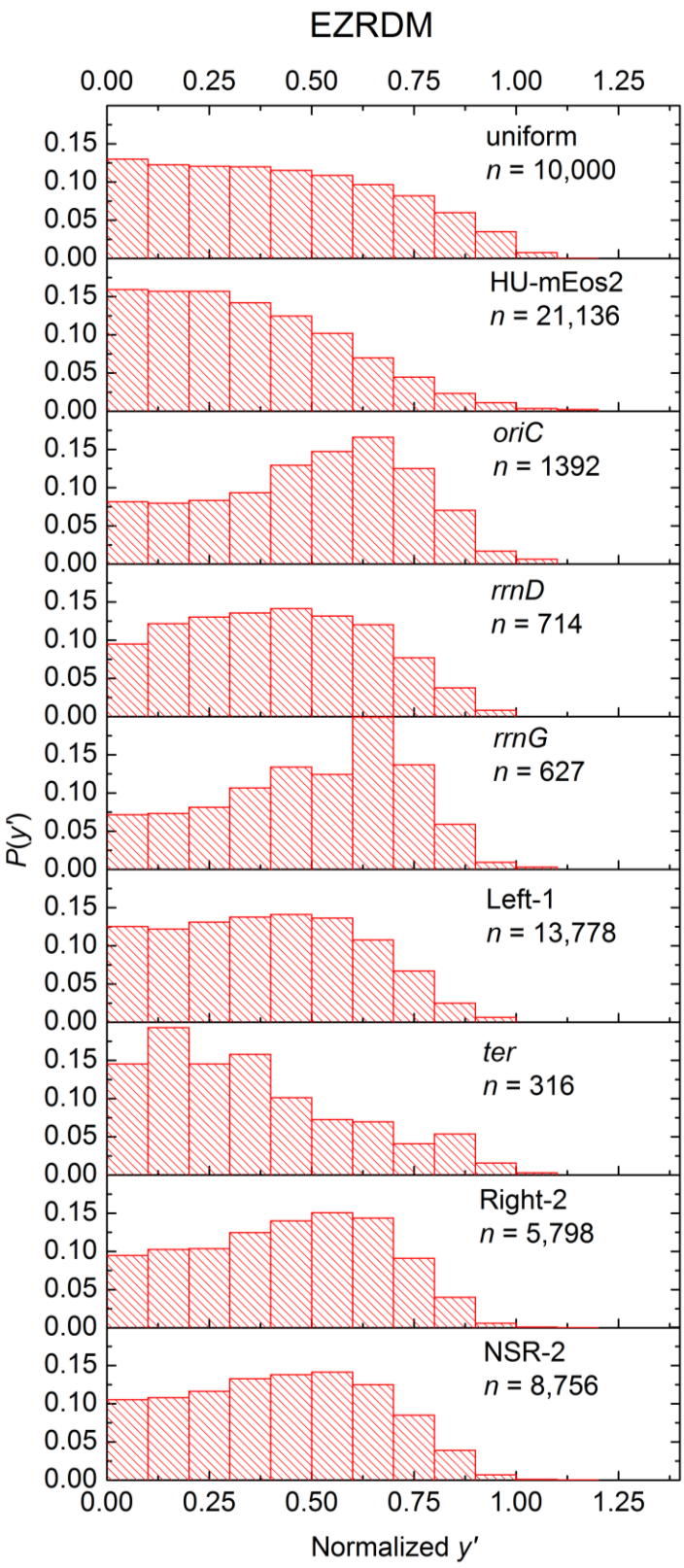

Figure 6. Specific foci have different distributions in y'. $P(y')$ histograms for all loci positions measured in cells grown in EZRDM irrespective of cell background. Data is normalized by cell radius (445 ± 25 nm for VH1000, 424 ± 20 nm for MG1655) with 0 at the cell center and 1 at the far edge. The distribution of positions in a uniformly filled cylinder with r = 445 ± 25 nm (calculated from y-intercepts of the MSD curves in Chapter 3 as intercept = $4\sigma^2$) is also included for comparison, as is the distribution of HU-mEos2. Chromosome map provided again for reference.

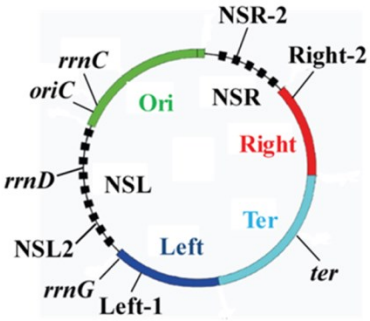

Figure 7. Comparison of $P(y')$ for loci in cells grown in EZRDM and MBM. Data is normalized by cell radius (445 ± 25 nm for EZRDM, 315 ± 26 nm for MBM) with 0 at the cell center and 1 at the far edge. The distribution of positions in a uniformly filled cylinder with r equal to the average cell radius and σ = 25 nm for the EZRDM data and σ = 16 nm for the MBM data (calculated from y-intercepts of the MSD curves in Chapter 3 as intercept = $4\sigma^2$) is also included for comparison.

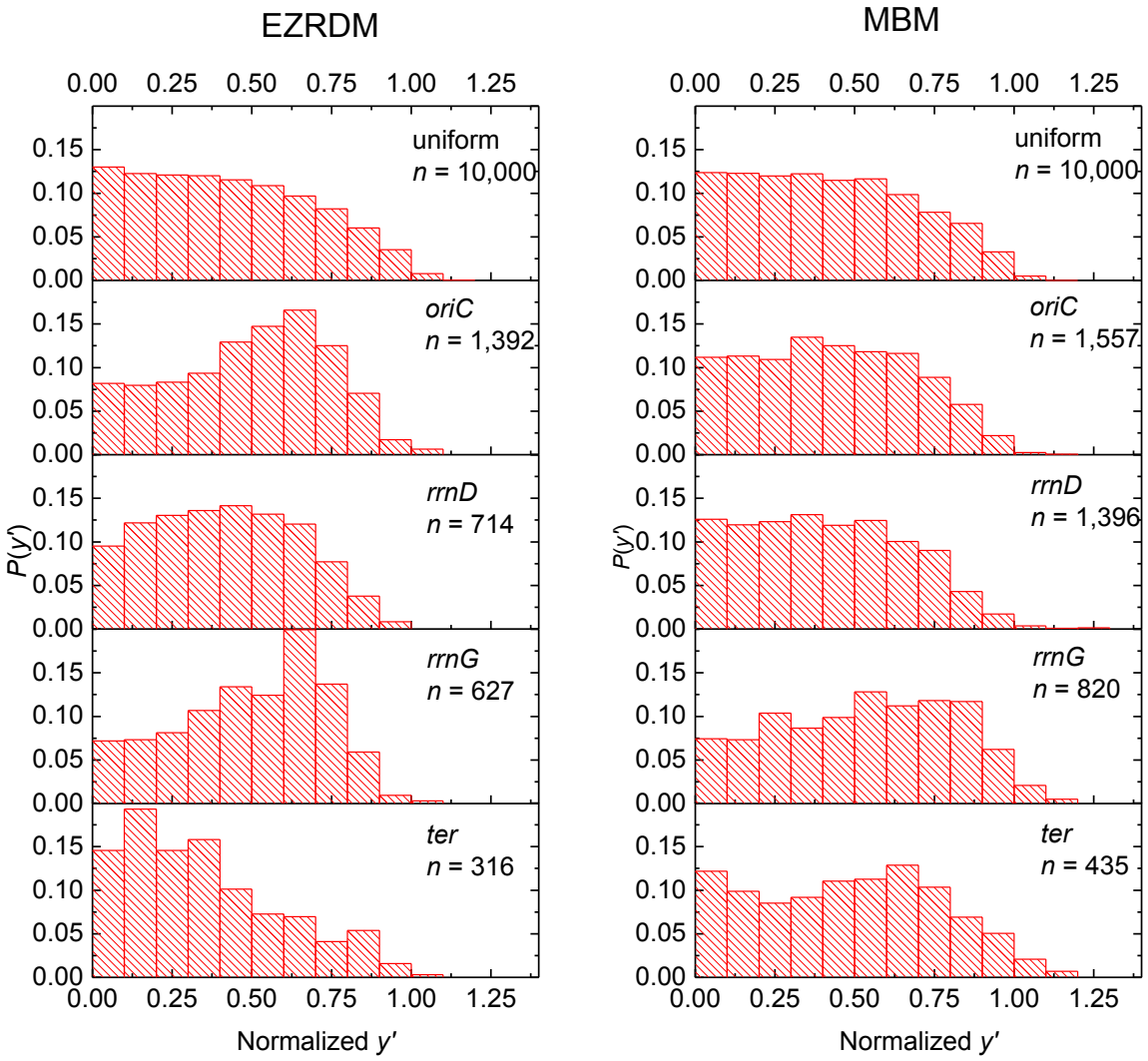

Figure 8. Comparison of $P(y')$ for HU with a model distribution for a uniformly filled cylinder of radius 445 nm. The cylinder model includes localization error of $\sigma = 25$ nm. The HU distribution is narrower than the cytoplasm as expected based on previous observations of RNAP distributions.[14] HU-mEos2 data collected by Somenath Bakshi and Wenting Li.

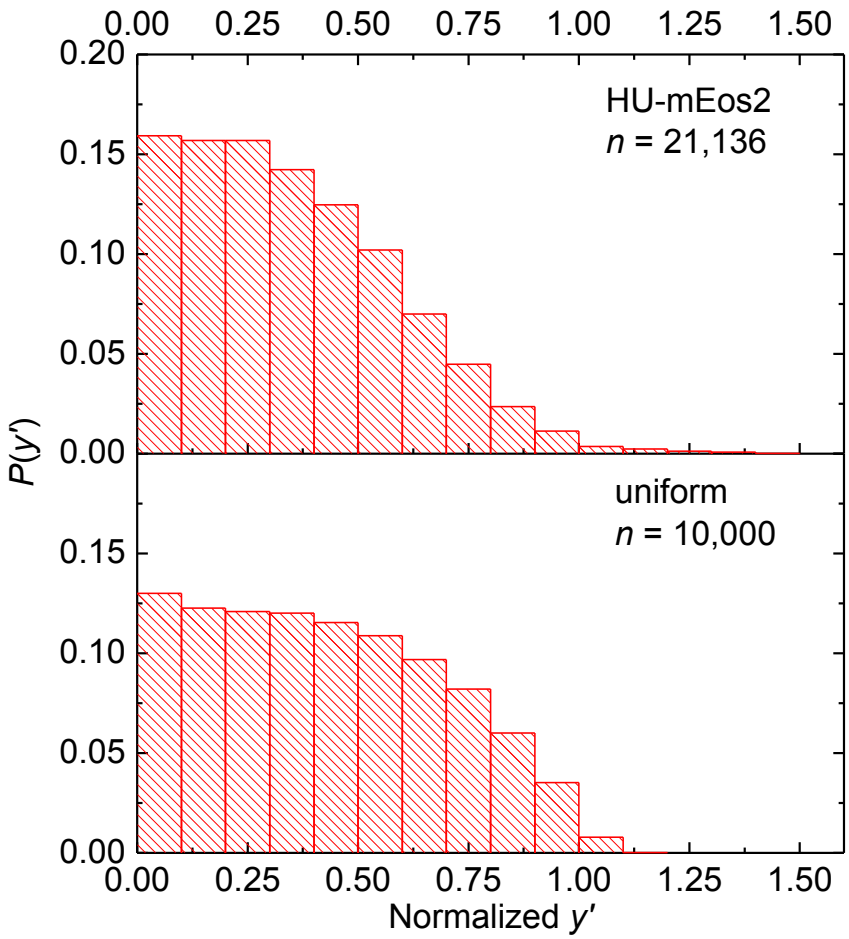

Figure 9. Plots comparing the *P*(*y'*) distributions for foci of varying intensity groups.

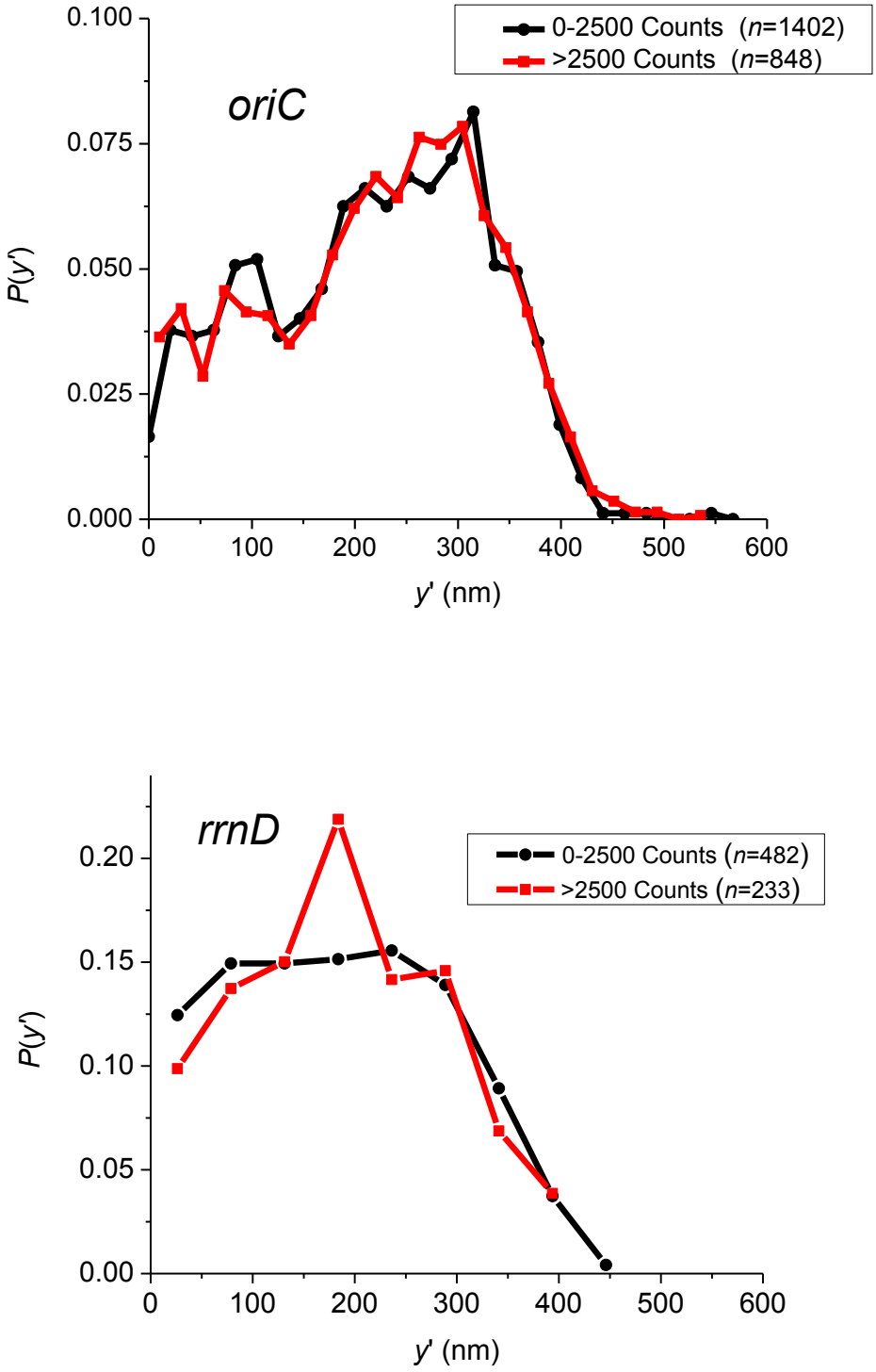

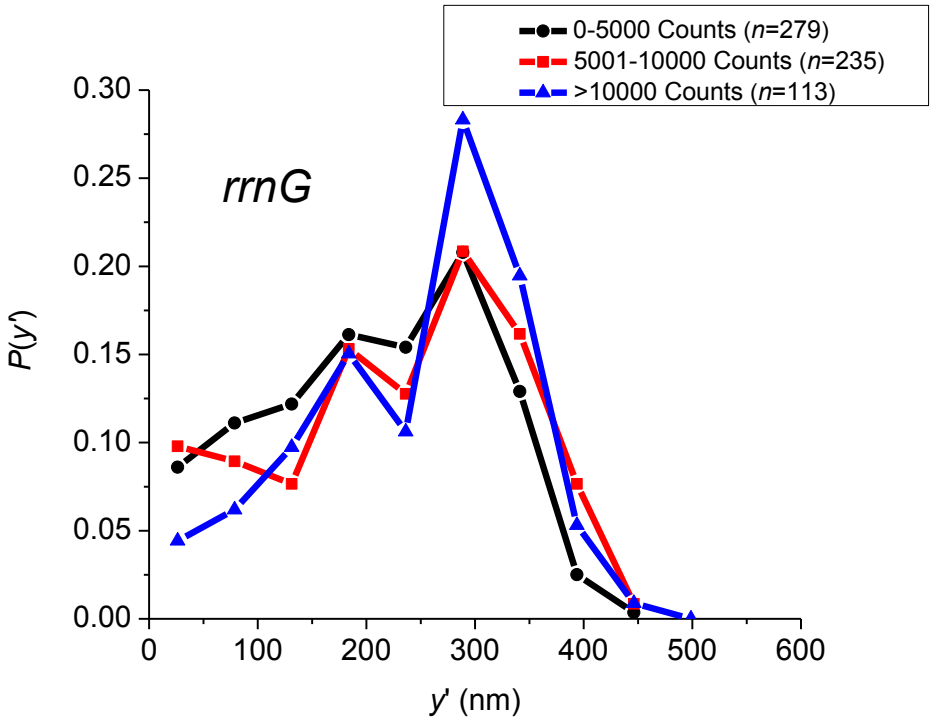
0-5000 Counts (n=279)
5001-10000 Counts (n=235)
>10000 Counts (n=113)
rrnG
P(y')
y' (nm)
0.00
0.05
0.10
0.15
0.20
0.25
0.30
0
100
200
300
400
500
600

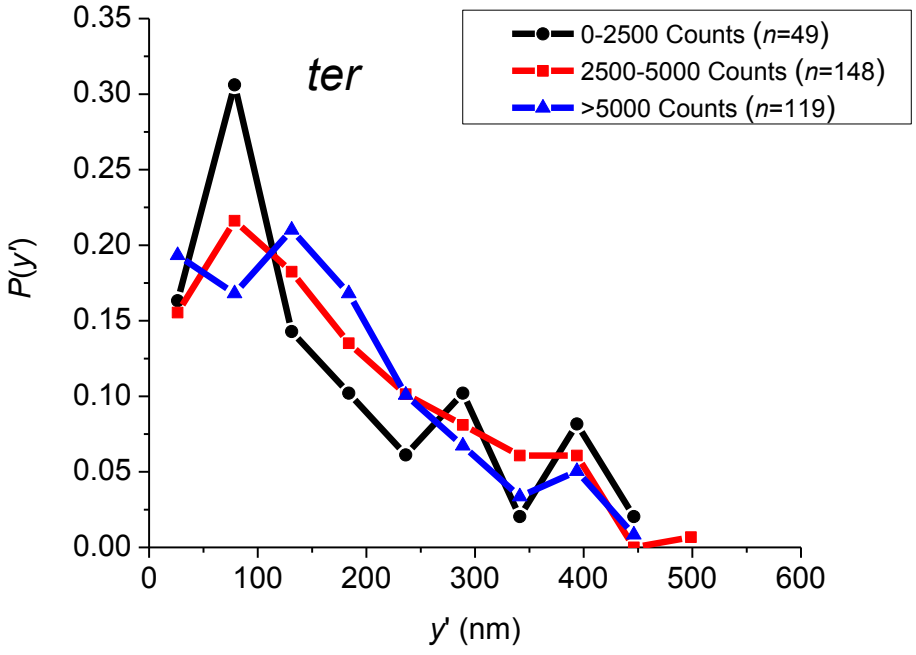
0-2500 Counts (n=49)
2500-5000 Counts (n=148)
>5000 Counts (n=119)
ter
P(y')
y' (nm)
0.00
0.05
0.10
0.15
0.20
0.25
0.30
0.35
0
100
200
300
400
500
600

References

1 Wiggins, P. A., Cheveralls, K. C., Martin, J. S., Lintner, R. & Kondev, J. Strong intranucleoid interactions organize the Escherichia coli chromosome into a nucleoid filament. *PNAS* **107**, 4991–4995 (2010).

2 Niki, H., Yamaichi, Y. & Hiraga, S. Dynamic organization of chromosomal DNA in Escherichia coli. *Genes & Development* **14**, 212-223, doi:10.1101/gad.14.2.212 (2000).

3 Roos, M. *et al.* Cellular localization of oriC during the cell cycle of Escherichia coli as analyzed by fluorescent in situ hybridization. *Biochimie* **81**, 797-802, doi:http://dx.doi.org/10.1016/S0300-9084(99)00218-7 (1999).

4 Bates, D. & Kleckner, N. Chromosome and Replisome Dynamics in E. coli: Loss of Sister Cohesion Triggers Global Chromosome Movement and Mediates Chromosome Segregation. *Cell* **121**, 899-911, doi:http://dx.doi.org/10.1016/j.cell.2005.04.013 (2005).

5 Wang, X., Possoz, C. & Sherratt, D. J. Dancing around the divisome: asymmetric chromosome segregation in Escherichia coli. *Genes & Development* **19**, 2367-2377, doi:10.1101/gad.345305 (2005).

6 Wang, X., Liu, X., Possoz, C. & Sherratt, D. J. The two Escherichia coli chromosome arms locate to separate cell halves. *Genes & Development* **20**, 1727-1731, doi:10.1101/gad.388406 (2006).

7 Nielsen, H. J., Li, Y., Youngren, B., Hansen, F. G. & Austin, S. Progressive segregation of the Escherichia coli chromosome. *Molecular Microbiology* **61**, 383-393, doi:10.1111/j.1365-2958.2006.05245.x (2006).

8 Nielsen, H. J., Ottesen, J. R., Youngren, B., Austin, S. J. & Hansen, F. G. The Escherichia coli chromosome is organized with the left and right chromosome arms in separate cell halves. *Molecular Microbiology* **62**, 331-338, doi:10.1111/j.1365-2958.2006.05346.x (2006).

9 Bakshi, S., Dalrymple, R. M., Li, W., Choi, H. & Weisshaar, J. C. *Partitioning of RNA Polymerase Activity in Live E. coli from Analysis of Single-molecule Diffusive Trajectories* (2013).

10 Sliusarenko, O., Heinritz, J., Emonet, T. & Jacobs-Wagner, C. High-throughput, subpixel precision analysis of bacterial morphogenesis and intracellular spatio-temporal dynamics. *Molecular Microbiology* **80**, 612-627, doi:10.1111/j.1365-2958.2011.07579.x (2011).

11 Bakshi, S., Bratton, Benjamin P. & Weisshaar, J. C. Subdiffraction-Limit Study of Kaede Diffusion and Spatial Distribution in Live Escherichia coli. *Biophysical journal* **101**, 2535-2544 (2011).

12 Meile, J.-C. *et al.* The terminal region of the E. coli chromosome localises at the periphery of the nucleoid. *BMC Microbiology* **11**, 28 (2011).

13 Mondal, J., Bratton, B. P., Li, Y., Yethiraj, A. & Weisshaar, James C. Entropy-Based Mechanism of Ribosome-Nucleoid Segregation in E. coli Cells. *Biophysical journal* **100**, 2605-2613, doi:http://dx.doi.org/10.1016/j.bpj.2011.04.030 (2011).

14 Bakshi, S., Siryaporn, A., Goulian, M. & Weisshaar, J. C. Superresolution imaging of ribosomes and RNA polymerase in live Escherichia coli cells. *Molecular Microbiology* **85**, 21-38, doi:10.1111/j.1365-2958.2012.08081.x (2012).

15 Hadizadeh Yazdi, N., Guet, C. C., Johnson, R. C. & Marko, J. F. Variation of the folding and dynamics of the Escherichia coli chromosome with growth conditions. *Molecular Microbiology* **86**, 1318-1333, doi:10.1111/mmi.12071 (2012).

16 Fisher, J. K. *et al.* Four-Dimensional Imaging of E. coli Nucleoid Organization and Dynamics in Living Cells. *Cell* **153**, 882-895 (2013).

17 Berlatzky, I. A., Rouvinski, A. & Ben-Yehuda, S. Spatial organization of a replicating bacterial chromosome. *Proceedings of the National Academy of Sciences* **105**, 14136-14140, doi:10.1073/pnas.0804982105 (2008).

18 Umbarger, Mark A. *et al.* The Three-Dimensional Architecture of a Bacterial Genome and Its Alteration by Genetic Perturbation. *Molecular cell* **44**, 252-264 (2011).

19 Libby, E. A., Roggiani, M. & Goulian, M. Membrane protein expression triggers chromosomal locus repositioning in bacteria. *Proceedings of the National Academy of Sciences*, doi:10.1073/pnas.1109479109 (2012).

20 Berger, M. *et al.* Coordination of genomic structure and transcription by the main bacterial nucleoid-associated protein HU. *EMBO Rep* **11**, 59–64 (2010).

21 Valens, M., Penaud, S., Rossignol, M., Cornet, F. & Boccard, F. Macrodomain organization of the Escherichia coli chromosome. *EMBO J.* **23**, 4330-4341 (2004).